Stony Brook University

Defect characterization and stress analysis by white beam synchrotron X-ray topography in single crystal semiconducting materials

A Dissertation Presented

by

Vishwanath Sarkar

to

The Graduate School

in Partial Fulfillment of the

Requirements

for the Degree of

Doctor of Philosophy

in

Materials Science and Engineering

Stony Brook University

December 2011

Stony Brook University

The Graduate School

Vishwanath Sarkar

We, the dissertation committee for the above candidate for the

Doctor of Philosophy degree, hereby recommend

acceptance of this dissertation.

Michael Dudley – Dissertation Advisor
Professor, Department of Materials Science and Engineering

Dilip Gersappe- Chairperson of Defense
Professor, Department of Materials Science and Engineering

Balaji Raghothamachar
Research Professor, Department of Materials Science and Engineering

Vladimir Noveski
PhD, Senior Engineer
Intel Incorporated

This dissertation is accepted by the Graduate School

Lawrence Martin
Dean of the Graduate School

Defect characterization and stress analysis by white beam synchrotron X-ray topography in single crystal semiconducting materials

by

Vishwanath Sarkar

Doctor of Philosophy

in

Materials Science and Engineering

Stony Brook University

2011

Semiconductor devices are becoming increasingly more complex as the number of transistors increases in the same Integrated Circuit (IC) area. Due to the complexity in design; processing and packaging of the device plays a crucial role in the IC fabrication. Package induced residual stress are not only detrimental to device performance but can also lead to device failure. We propose a non-destructive method to determine the complete stress state at each point on a packaged Silicon device. Surface and edge defect created as a result of various manufacturing steps were characterized using different techniques, primarily X-ray diffraction topography, optical microscopy, SEM and TEM.

Residual stress plays an important role in the performance and lifetime of single crystal device material. Here we present a novel technique using white beam synchrotron X-ray diffraction reticulography, Stress Mapping and Analysis via Ray Tracing (SMART) in order to determine residual stress level at an array of points over the entire crystal area. This method has a unique advantage compared with other stress measurement technique in that it can evaluate all six components of the stress tensor. The underlying experimental technique is based on white beam synchrotron X-ray diffraction topography and ray tracing. An array of X-ray micro-beam is illuminated on the single crystal sample and multiple reflections (reticulographs) are recorded simultaneously on a photographic film. Crystallographic plane normal vector at the location of

each micro-beam in the crystal is calculated. The variation of the plane normal vector direction is due to residual strain (both sheer and dilatational) present in the crystal. By considering three different diffracting planes and corresponding reticulograph a complete state of stress is calculated. Principle, applications and limitations are discussed.

White beam synchrotron reticulography is used in reflection geometry to evaluate complete residual stress tensor as a function of depth in a single crystal material. This novel technique, an extension of SMART technique is developed to determine stress tensor components at various depths within the crystal. In reflection geometry penetration depth is controlled by manipulating the geometrical parameters such as incident angle. Data is obtained from various penetration depth, which represents exponentially decaying weighted average of actual stress value or in other words this stress profile is Laplace transform of real stress profile. Mathematical procedure is described to determine real stress profile from Laplace profile. To demonstrate this method, a packaged semiconducting Silicon die is used and its complete stress tensor profile is generated. This method has demonstrated the capability of determining all six components of stress as a function of depth in the crystal. Experimental procedure, theoretical basis and mathematical methods along with its application, capability and limitations are discussed.

Wafer dicing process results in edge and surface damage. Various characterization tools were used to detect these defects. Surface reflection topographs were taken to probe surface and subsurface defects, primarily scratches and micro cracks. Optical microscopy and SEM were used as a complementary tool for surface characterization. TEM is used for detecting sub-surface nano-cracks and dislocations. X-ray transmission topography is used to detect half loop dislocations resulting from dicing process. In order to study dynamic behavior of defects (dislocations) during thermal processing and operation an environmental chamber (furnace) is designed and built to record in-situ X-ray diffraction topographs during thermal cycling and at high temperature.

Table of Contents

List of Figures

List of Tables

List of Abbreviations

SWBXT: Synchrotron white beam X-ray topography

SWBXR: Synchrotron white beam X-ray reticulography

SEM: Scanning electron microscope

TEM: Transmission electron microscope

IC: Integrated circuit

FWHM: Full width at half maxima

SMART: Stress mapping and analysis via Ray Tracing

CTE: Coefficient of thermal expansion

Acknowledgements

First I would like to give my deep and sincere gratitude to Professor Michael Dudley, my Ph.D. advisor, for providing me this great opportunity to study in the field of semiconductor characterization and stress analysis. His wide knowledge and helpful guidance have been of great value for me. No doubt his understanding, encouragement and personal guidance have always been providing an excellent basis for my Ph.D. research.

I would like to thank Dr. Balaji Raghothamachar, valuable suggestion and discussion during the entire research project.

I would like to thank Dr. Vladimir Noveski from Intel Corporation and Professor Dilip Gersappe for being in my defense committee member and their invaluable help and suggestion during my research project.

I would also like to thank my colleagues: Dr. Hui Chen, Dr. Yi Chen, Dr. Yu Zhang, Mr. Fangzhen Wu, Ms. Huanhuan Wang, Ms. Mengjia Gaowei, Mr. Shayan Byrappa, Ms. Gloria Choi and Ms. Shun Sun for their help and during my research.

I would also like to thank Mr. Lester Orlick and Mr. Frank Burger for help with machining and assembling the furnace.

I would also like to acknowledge continuous help and support of graduate program coordinator Ms. Deborah Michienzi, Ms. Lynn Allopenna and Ms. Chandrani Roy.

Finally, I would like to thank my parents Mr. Dilip Sarkar and Mrs. Kajal Sarkar, my daughter Kritika Sarkar and my wife, Dr. Paramita Sarkar, for her great assistance during my Ph.D. study. Without her, I would not have been able to spend so much time on my research and attain so many results.

This work was supported by Intel Corporation. I would like to thank Dr. Ravi Mahajan and Dr. Deepak Goyal for their generous help, discussion and suggestion. X-ray reticulography experiments were carried out at the Stony Brook Synchrotron Topography Facility (Beamline X-19C) at the NSLS, Brookhaven National Laboratory, which is supported by the U.S. Department of Energy, under Contract No. DE-AC02-98CH10886.

Fields of Study

This section summarizes my major research accomplishments. Residual stress and defect structure developed inside a Silicon IC during processing and packaging is studied in detail using X-ray diffraction topography. Defects developed during processing and operations are studied by in-situ topography. A new technique to determine residual stress is developed, which can have huge potential and application in semiconductor and crystal growth industry.

A. A new method (SMART), based on white beam synchrotron diffraction topography technique is developed to determine residual stress in single crystal material. All six components of stress can be determined by this method. A good spatial resolution is achieved by this technique. Transmission X-ray technique is used, which provided average through thickness stress value, which provides reasonable results if the stress variation along the thickness is not large.

B. SMART technique is extended in reflection X-ray geometry to determine depth resolved stress tensor components. For demonstration of capability of this technique strain and stress maps were generated at a specific depth below the crystal.

C. Semiconductor processing involves various mechanical, thermal and chemical operation subjected to Silicon crystal. Defects generated due to wafer cutting and various other processes are studied in detail. Techniques such as optical microscopy, SEM, TEM and X-ray diffraction topography are used for characterizing defects. In order to understand real time defect movements during processing and operation of IC, an environmental chamber for in-situ topography is designed and built and in-situ experiments were carried out.

Chapter 1 Introduction

1.1 Residual stress in integrated circuit

Packaged Silicon integrated circuit (IC) is a complex composite structure, primarily composed of Silicon, solder material, Copper, interconnects, plastic backing and other materials. Each of these material have different coefficient of thermal expansion (CTE) and different elastic properties. These materials are processed at different temperature and leads to residual stress within the structure. Stresses are developed not only during processing of the IC but also during the operation due to thermal cycling [1]. Thermo-mechanical stresses build up in the package during manufacture and operation of the device. The residual stress in an electronic component not only leads to device failure but also can affect the intended electrical performance of the device [2]. Residual stresses can cause failure at the junction of two dissimilar materials by producing crack and hence reliving the stress [3]. It is also a well known fact that the transistor characteristic of a semiconducting chip is affected by surface residual stress.

Integrated circuits (ICs) for microelectronics are becoming more and more complex as technological developments demand higher performance and improved functionality from electronic circuits. They are used in ever more severe environmental conditions for application in military, automotive or space needs. An electronic package serves as mechanical support and protection from external environment such as high humidity level, light radiations, etc. It also allows power and signal transmission to and from the chip using interconnections from the chip surface to leads extend outside the package.

These types of stresses are one of the most serious concerns for the semiconductor device manufacturer. Problem arises due to residual stress are critical in Silicon technology. A substantial number of defective Silicon IC can be attributed to stresses developed during processing. These problems become more complex as the circuit design involves complicated geometry and more different kind of materials are involved. It is not only important to understand the nature and origin of these stresses but also quantitatively characterize and evaluate the residual stress by experimentation and modeling.

The origin of residual stresses can be broadly classified into following categories [1]:

1. Stress due to thermal gradient: Results from non-uniform temperature distribution in a silicon wafer.
2. Film stresses: Stress resulting from films such as silicon dioxide, silicon nitride which are overlaid on silicon substrate.
3. Stress arising from embedded structural elements: Embedded elements such as metal lines on amorphous on silicon dioxide, recessed oxide isolation and trench isolation on silicon substrate
4. Stress in planer and non-planer thermal oxide: Local oxidation such as converting silicon to SiO_2 results in volume expansion. This process must be accommodated by either viscoelastic flow of SiO_2 or the plastic deformation of Silicon resulting in dislocations.
5. Strain and misfit dislocations in doped lattices and hetroepitaxy: This strain is due to lattice mismatch between epitaxial layer and the substrate.
6. IC packaging: Residual stress resulting from encapsulation of IC in the final package.

Quantitative understanding of residual stress is critical in optimization of manufacturing process, materials selection, and device structural geometries.

1.2 Research objective

The primary objective of this research is to study residual stress and damage incurred during packaging process of Silicon dies. Two problems are studied and investigated in detailed here: (A) thermo-mechanical stresses generated in the packaged Silicon die. (B) edge/surface damage and defects incurred during the saw and laser cutting of the individual Silicon dies from the wafer. The residual stresses and the edge defect structures are studied and measured non-destructively and non-invasively as a function of lateral position and depth in the device using the technique of Synchrotron White Beam X-ray Topography (SWBXRT) and Synchrotron White Beam X-ray Reticulography (SWBXR). Stress mapping and measurement is carried out using SMART (Stress Measurement and Analysis via Ray Tracing) technique developed in our lab. Stress and strain maps are generated across the crystal area and at various depths. Both the problems were studied and addressed separately through various sets of experiment.

The overall goal of the residual stress measurement analysis is to systematically characterize the effect of each packaging process step for different packaging type (flip chip or

wire bond etc.) on the generation of stresses in the package. From this information, it would be possible to identify the manufacturing processes and materials responsible for high stress generation. This information can be used to develop optimized packaging process and/or material.

The broader goal of studying edge damage induced defects and propagation of these defects during subsequent processes is to help the development of cutting and edge-preparation procedure to minimize the deleterious effect of this damage and also to develop a complete set of characterization tool for qualitative and quantitative assessment of these defects.

Excessive level of stress may degrade performance and eventually lead to failure of the device. It is therefore, important to be able to understand and evaluate the levels of thermo-mechanical stress in the IC in order to gain insight of failure mechanism and improve package reliability. This information on the level and distribution of stresses within packaged Silicon substrate will also provide an understanding on how stresses are generated during packaging processes and aid the development of optimized packages and packaging processes which minimize stress generation for microelectronics.

The generation and propagation of defects from die edges, caused by damage from cutting and processing strongly influence the reliability and performance of devices. For example, a dislocation which propagated into the device, acts as an electronic short and can destroy the device. Understanding of the type and density of edge defects and how they propagate under thermo-mechanical stress and/or during temperature cycling can facilitate the development of optimized cutting processes thereby minimizing the generation of edge defects.

Various destructive and non destructive techniques are available in order to evaluate the residual stress [4]. Destructive method of residual stress determination generally involves two steps: (A) Stress relaxation by removal of material and then (B) measuring the state of strain or displacement due to relaxation. Some of the commonly used destructive methods for residual stress determination are: Hole drilling, Ring core, Bending deflection and Sectioning method. Macroscopic strain is measured by either strain gauge or optical technique such as moiré interferometry, holography, electronic shearohraphy and laser speckle interferometry. Residual stress can then be determined by using elasticity theory. Most common techniques using non-

destructive methods are: X-ray and neutron diffraction [5], Raman spectroscopy [6], piezoresistive stress sensing method[7], Moire interferometry [8], photoelastic technique [9], scanning acoustic microscopy[10] and finite element modeling [11]. There are various methods described in literature to determine residual stress using X-rays [12-17]. All these techniques have their own advantages and disadvantages such as number of stress components determined, spatial resolution, precision or stress resolution, speed and ease of measurement.

Silicon wafers for IC production are currently being manufactured dislocation free up to 300mm in diameter. Excessive stress during wafer dicing process can cause defects such as microcracks and dislocations to originate at the surface or the edge. Microcracks in combination with stress can catastrophically break the crystal while dislocations can reduce the yield of electronic devices. Many manufacturing steps in the production of Silicon integrated circuit create stress in the Silicon substrate. In case when this stress level exceeds a certain level, the crystal will yield by generating dislocation. Various sources of stress generation during IC fabrication and stress-induced dislocation is Silicon IC is studied by Fahey et al. [18]. Recently, in-situ study of dislocation dynamics and slip band formation in Silicon single crystal by X-ray diffraction topography is carried out by Danilewsky et al. [19]. Apart from X-ray topography various other characterization tools such as TEM, SEM, and optical microscopy are used for studying edge damage.

1.3 Various X-ray techniques for residual stress determination

Many techniques for measurement of residual strain using X-ray are described in the literature. Different techniques have its advantages and disadvantages. A literature review of residual stress measurement in single crystal material, using X-ray diffraction is given in this section.

The measurement of strain field by utilizing topographic equi-inclination contour mapping is studied by Stock et al. [16]. Characteristic X-rays from lab source or monochromatic radiation from synchrotron can be used to generate equi-inclination contour maps. Strain is calculated by analyzing a number of equi-inclination contour topograph generated by rotating crystal through steps of small angle.

Due of its technological importance, a considerable amount of work is been done in evaluating residual stress in integrated circuits. Recently stress measurement on flip chip assembly was measured by Chen et al. [12] using micron size white beam synchrotron X-ray. Laue pattern were recorded by scanning the crystal across horizontal and vertical lines. Using the deviation in the Laue pattern, curvature of the crystal was measured and then stress was calculated.

Photographic technique to determine residual stress in mounted Silicon chip is reported by Kozaki et al. [13], [20]. Residual stress at various locations on the chip is determined by using characteristic X-rays of very small size (60μm diameter). Back reflection diffraction pattern is recorded for both the sample and the stress free Silicon sample. Strain and thereby stress is calculated by comparing stresses sample with stress free sample. In this method plane stress condition is assumed and measurements were recorded from about 15μm depth below the crystal surface.

Strain field developed during packaging process of an IC is studied by Kanatharana et al. [21], [15], [22], [23] using synchrotron radiation. Strain developed during the reflow process for Lead-Tin solder bumps in a ball grid array package is studied. Lattice strain is calculated by determining magnitude of orientation contrast shift.

A stress measurement technique is proposed by Suzuki et al. [17], [24] which did not rely on the measurement of stress free lattice parameter or stress free crystal. They also assumed the plane stress condition in the crystal and calculated three stress components. This method evaluates the plane stress state with any combination of diffraction planes. They demonstrated their technique by evaluating stress field in single crystal Silicon and Iron. This method calculates stress using multiple regression analysis using angle of at least four different diffraction planes. This method is capable of measuring three components of stress by assuming a plane stress condition.

A quite interesting study is carried out by Ando et al. [25] where they intentionally applied compressive stress at diametrically opposite sides of a circular single crystal Silicon plate. Topographs were taken using different characteristic radiation and strain field were qualitatively compared with the theory.

Measurement of minute local strain in semiconductor using highly parallel microbeam (angular divergence < 2arcsecond) is studied by Matsui et al.[26]. This technique is reported to have capability of measuring strain of the order of 10^{-5} to 10^{-6}. This technique essentially measures rocking curve and calculate the peak shift. This technique only evaluates only one component of normal strain.

A comprehensive study on strain in semiconductor crystal, especially Silicon, was done by Matsui [27] and by Bonse et al. [28]. Monochromatic synchrotron radiation is used for determining strain using topography. Various sources of strain such as growth striation, strain due to minute defects were identified and studied.

Lattice plane tilt and the relative lattice parameter $\Delta d / d$ (dilatational strain) is been calculated and mapped over the entire wafer area by Kikuta et al.[14] and later by Barnett et al. [29]. This method utilized double crystal topography using synchrotron source. It is shown that lattice plane tilt and the dilatational strain component can be calculated using the formula:

$$\phi(r) = \frac{\alpha_2(r) - \alpha_1(r)}{2} \quad \text{Equation 1-1}$$

$$\frac{\Delta d(r)}{d(r_o)} = -\frac{\left(\alpha_2(r) + \alpha_1(r)\right)}{2\tan(\theta_0)} \quad \text{Equation 1-2}$$

where r is a general position on the crystal.

$\alpha_1(r)$ is the angle through which crystal has to be rotated for diffracting condition from position r_0 to r. $\alpha_2(r)$ angle determined at same location by rotating the crystal 180^0 about diffraction vector **g**.

r_0 is an arbitrary chosen reference point for the entire experiment. A complete map of lattice tilt and lattice strain is plotted over the entire wafer area. The accuracy of this method depends on the chosen Braggs reflection and is increased by using high order Bragg's reflection which will give large Bragg's angle and a narrow rocking curve width.

A compilation of above techniques is provided in tabular format below:

Table 1-1: Residual stress measurement by X-ray techniques reported by different authors.

Author	**Reference**	**Comments**
Stock, Chen	[16]	Equi-inclination contour map
Chen	[12]	Curvature is measured by evaluating deviation from Laue pattern
Kozaki	[13, 20]	Photographic technique 15μm depth below the crystal
Kanatharana	[15, 21-23]	Strain is determined by magnitude of orientation contrast shift
Suzuki	[17, 24]	Three stress components were evaluated and plane stress condition is assumed.
Ando	[25]	Strain field were qualitatively compared with the theory by applying predefined stress
Matsui	[26]	Local minute strain is evaluated by determination of peak shift in rocking curve.
Matsui	[27]	Monochromatic synchrotron radiation, equi-lattice-parameter mapping
Bonse	[28]	Rocking curve technique to determining minute lattice strain in Silicon
Kikuta	[14]	Lattice plane variation and tilt is mapped in single crystal Silicon using Lab source.
Barnett	[29]	Lattice plane tilt and strain in GaAs wafer is measured and mapped using synchrotron radiation.

In any stress measurement method, stress is never measured directly, strain is first calculated by measuring some physical quantity and then stress is calculated. For example, in case of measuring applied stress, strain gauge is used which measures electrical resistance before and after applied stress and in case of $\sin^2\psi$ method lattice parameter is measured at different azimuthal angle, radius of curvature on sample surface is measured in case of curvature method. In the method presented here, the physical quantity we are measuring is the lattice plane normal direction on three crystallographic planes, at a location in the crystal simultaneously using white beam X-rays.

Synchrotron x-ray topography is a well established X-ray imaging technique used to detect defects in highly perfect single crystal. A topograph is a two dimensional image formed on a detector (usually photographic film) placed in the path of area-filling diffracted beam from single crystal exposed to an incident area-filling X-ray beam. Synchrotron X-ray topography technique is highly sensitive to lattice strain present within the crystal. It is used to detect dislocations, small angle grain boundary, lattice strain variation and other defects related to crystal growth. In this work we have devised a technique to determine strain (and hence stress) in

the crystal using the fundamental concept of X-ray topography and ray tracing. Spatially resolves as well as depth resolved stress values were determined in this new technique.

1.4 Fundamentals of X-ray diffraction

X-ray diffraction technique has been extensively used by chemists, metallurgists and material scientists to determine structure of materials. Diffraction is a phenomenon when a wave (X-ray) interacts with a crystalline material to form a constructive interference i.e. scattered waves mutually reinforce each other. X-rays when interact with crystalline material, diffract according to Braggs law.

$$\lambda = 2d\,Sin(\theta) \qquad \text{Equation 1-3}$$

where λ is the wavelength of the X-rays, d is interplaner spacing and θ is the angle incident ray makes with the crystallographic plane.

In order to understand and explain the X-ray diffraction phenomena in crystalline materials, kinematical and dynamical theory of X-ray diffraction are employed. Laue's kinematical theory [30] provides good approximation when X-rays interact with relatively small imperfect crystal, whereas dynamical theory proposed by Ewald and Darwin is useful for large and highly perfect crystal. Nonetheless kinematical theory plays an important role in interpreting topographic contrasts and is discussed latter in this chapter. In the kinematical theory, X-rays are assumed to be scattered by atom only once, and re-scattering is negligible. Dynamical theory considers re-scattering of X-rays in the lattice.

Dynamical theory of X-ray diffraction was developed to address discrepancies from kinematical theory. Kinematical theory is employed satisfactorily in case of small highly deformed crystal. However large single crystals which are highly perfect, significant discrepancies exist between measured intensity and intensity predicted by kinematical theory. Diffracted intensity is predicted to increase continuously with increasing size of crystal in kinematical theory which clearly contradicts conservation of energy. In a large single crystal the breakdown of kinematical theory is clearly demonstrated by the phenomena of primary extinction. The dynamical theory of X-ray diffraction takes into account the overall wavefield inside a crystal while diffraction takes place as a single entity. Dynamical theory primarily solves Maxwell's equations in a periodic lattice (crystal). In a large perfect single crystal, X-rays are

diffracted dynamically where multiple scattering occurs. Bloch waves are created inside the crystal as the X-ray wavefield interacts with the periodic crystal laccice.

Assuming parallelepiped shaped crystal with N_i unit cells along a_i axis, where i is 1, 2 or 3. Diffraction intensity is given by:

$$I\left(\bar{b}\right) = \left|F\left(\bar{b}\right)\right|^2 G\left(\bar{b}\right) \qquad \text{Equation 1-4}$$

where $F\left(\bar{b}\right)$ = Structure factor $= \sum f_\alpha e^{-2\pi i b r_\alpha}$ Equation 1-5

and $G\left(\bar{b}\right)$ is Laue function, $G\left(\bar{b}\right) = \dfrac{\sin^2\left(\pi h N_1\right)}{\sin^2\left(\pi h\right)} \dfrac{\sin^2\left(\pi k N_2\right)}{\sin^2\left(\pi k\right)} \dfrac{\sin^2\left(\pi l N_3\right)}{\sin^2\left(\pi l\right)}$ Equation 1-6

$f_\alpha\left(\bar{b}\right)$ = atomic scattering factor of α^{th} atom located at $\bar{r}_\alpha = x_\alpha \bar{a}_1 + y_\alpha \bar{a}_2 + z_\alpha \bar{a}_3$ and $\bar{b}$ is the scattering vector given as $\bar{b} = h\bar{a}_1^* + k\bar{a}_2^* + l\bar{a}_3^*$ where $\bar{a}_1^*, \bar{a}_2^* \text{ and } \bar{a}_3^*$ are reciprocal vector and h, k and l are integers. x_α, y_α and z_α are the coordinates of the α^{th} atom within the unit cell and $\bar{a}_1, \bar{a}_2$ and $\bar{a}_3$ are unit cell vectors.

$$I = {F_{hkl}}^2 \frac{\sin^2\left(\pi h N_1\right)}{\sin^2\left(\pi h\right)} \frac{\sin^2\left(\pi k N_2\right)}{\sin^2\left(\pi k\right)} \frac{\sin^2\left(\pi l N_3\right)}{\sin^2\left(\pi l\right)} \qquad \text{Equation 1-7}$$

This equation is based on kinematical theory, and work well for small crystals but breaks down for larger crystals. When N_1, N_2, N_3 goes to infinity Laue function G(b) goes to infinity i.e. diffracted intensity is infinity which is physically impossible and contradicts conservation of energy. This equation is holds very well for small crystals but fails for large/thick crystals. Therefore dynamical theory of X-ray diffraction has to be applied in case of nearly perfect large size crystal.

Structure of Silicon is Diamond cubic which is closely related to FCC crystal structure, two interpenetrating FCC lattices. It belongs to space group F d -3 m (space group number 227). Lattice parameters at room temperature are:

$a = b = c = 5.4309\text{Å}$ and $\alpha = \beta = \gamma = 90^0$

Coordinate points of Silicon atoms within the unit cell are:

(0, 0, 0), (0, 1/2, 1/2), (1/2, 0, 1/2), (1/2, 1/2, 0)

(1/4, 1/4, 1/4), (1/4, 3/4, 3/4), (3/4, 1/4, 3/4), (3/4, 3/4, 1/4)

Therefore the structure factor can be written as:

$$F_{hkl} = f_{Si}\left[e^{2\pi i(0)} + e^{2\pi i\left(\frac{j}{2}+\frac{k}{2}\right)} + e^{2\pi i\left(\frac{i}{2}+\frac{k}{2}\right)} + e^{2\pi i\left(\frac{i}{2}+\frac{j}{2}\right)} + e^{2\pi i\left(\frac{i}{4}+\frac{j}{4}+\frac{k}{4}\right)} + e^{2\pi i\left(\frac{i}{4}+\frac{3j}{4}+\frac{3k}{4}\right)} + e^{2\pi i\left(\frac{3i}{4}+\frac{j}{4}+\frac{3k}{4}\right)} + e^{2\pi i\left(\frac{3i}{4}+\frac{3j}{4}+\frac{k}{4}\right)}\right]$$

Equation 1-8

After some mathematical calculation, the diffraction criteria can be shown as:

$F_{hkl}F_{hkl}^{*} = 0$ when h, k, l are mixed

$F_{hkl}F_{hkl}^{*} = 32f^{2}$ when h,k,l are odd

$F_{hkl}F_{hkl}^{*} = 64f^{2}$ when h,k,l are even and h+k+l=4n

$F_{hkl}F_{hkl}^{*} = 0$ when h,k,l are even and h+k+l≠4n

1.5 Introduction to X-ray diffraction topography

X-ray diffraction topography is a diffraction imaging technique used for detecting defects in large (>1mm) nearly perfect single crystalline material[31], [32], [33]. An X-ray topograph is a two-dimensional image obtained by projecting the distribution of diffracted intensity in an area-filling diffracted beam, produced by a low-divergence area-filling X-ray beam incident on a single crystal set at the Bragg angle, onto a two dimensional detector (usually high-resolution X-ray film, CCD detector or a nuclear plate). Contrasts in an X-ray topograph arises from different diffracting power between the region near the defect and the more perfect region. Local X-ray diffraction intensity variation, within the crystal, generates the contrast in the topograph.

The foundation of X-ray diffraction topography was mainly developed by classical laboratory X-ray work [34-39] between 1930 and 1960. Most of these works rely on characteristic X-rays from laboratory source. The development of synchrotron source has further advanced this technique by enabling white beam topography and enhancing monochromatic X-ray technique.

X-ray topography technique is primarily utilized for detecting and characterizing extended defects in single crystal. Most common defects observed in X-ray topographs are dislocations, stacking fault, small angle grain boundary, inclusions and surface damage. Point

defects cannot be determined by topography technique. A relatively short and concise overview of structural defect detection using X-ray topography is written by Klapper [40].
Even though nuclear plate and photographic film provides better resolution, digital CCD detectors are used for rapid production of topographic image [41]. X-ray topograph is recorded by illuminating a single crystal sample by an X-ray beam and recording the image of the diffracted beam. Contrast in the image is due to imperfection in the crystal which causes deviation, u(r) from perfect long range atomic order.
Variation in the topographic techniques are available, some commonly used techniques are listed below:

A. Lang topography
B. Berg-Barrett method
C. White beam topography
D. Plane wave topography
E. Section topography
F. Total external reflection topography

We have used white beam topography for recording most of our topographs.
Three main types of geometries are used for recording topographs in our research: (A) Transmission, (B) Back reflection, and (C) Reflection geometry. Schematic of these geometries are shown in Figure 1-1.

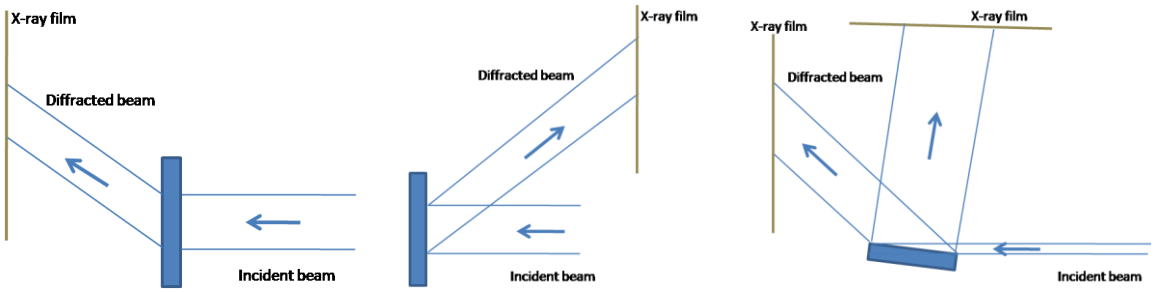

(A) (B) (C)

Figure 1-1: Schematic of most commonly used geometries in topography experiments.

In order to quantitatively analyze the defect, a complete understanding of contrast formation mechanism in different diffracting condition is required. For example, certain contrasts may disappear under certain diffraction condition.

The development of synchrotron radiation source has enabled a new era of topography, synchrotron topography. Synchrotron radiation has various advantages over conventional radiation such as high intensity, natural collimation and tunability. High intensity drastically reduces the exposure time to few seconds compared to hours or even days in conventional technique. Two most important synchrotron topography are white beam topography [42, 43] and monochromatic topography. The development of synchrotron source has enhanced the field of white beam topography to a different level [44]. A full description of X-ray topography requires dynamical theory of X-ray diffraction [45-47].

A freely available, robust and extremely useful, Windows based software program LauePt developed by Huang [48] is used extensively throughout this work. It is mainly used for indexing the Laue pattern, determination of wavelength and crystal orientation.

1.6 Resolution in X-ray diffraction topography

Individual defects can only be distinguishable if there is enough spatial resolution. Since there is no magnification in X-ray diffraction topography, the resolution can only be controlled by geometrical factors. Even though compared to electron microscopy, X-ray diffraction topography has much lower spatial resolution but it is more than sufficient for high quality crystals which are currently grown. In order to understand the resolution of X-ray diffraction topography, consider diffraction due to the Bragg's law $\lambda = 2d\sin(\theta)$. Consider a cone with semi-apex angle $(90^0 - \theta)$ and the axis of which is diffracting planes normal vector or the reciprocal lattice vector $(\bar{g})$ as shown in Figure 1-2.

Since X-ray source has a finite size, which indicates X-rays received at a point in crystal may have originated at two distinct points in the source. Therefore point P in the crystal will receive X-rays with correct Bragg's angle from locus of points in the source defined by the intersection of cone and the X-ray source surface. Consider three such points a, b and c on the surface of the source. X-rays emanating from points a, b and c after diffraction from point P will form an arc onto the detector A, B and C. This arc is generated by the locus of points defined by intersection of detector surface and the Bragg's cone. It can be seen that "image" of point P is spread over the arc A-B-C which gives rise to blurring effect in the image of that point. The plane where incident and diffraction beam vector lies, is defined as the plane of incidence (for

example plane bPb'). The source dimension perpendicular to the plane of incidence should be minimized in order to reduce the blurring effect or the effective resolution. The blurring is proportional to specimen to film distance, source size perpendicular in the direction of plane of incidence and inversely proportional to source to specimen distance.

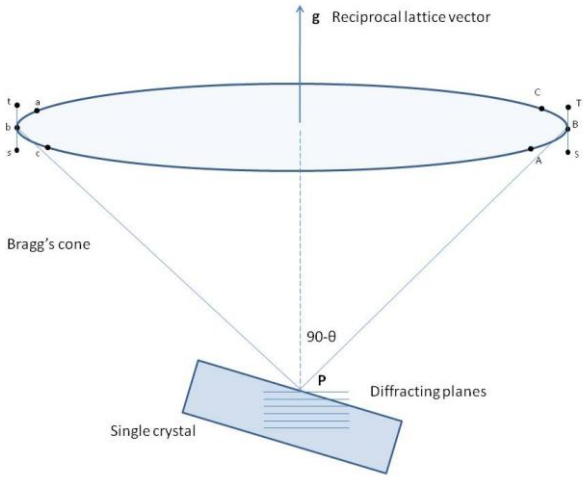

Figure 1-2: Schematic of diffraction geometry and Bragg's cone showing the effect of source dimension on resolution of topographic image. **g** is the active reciprocal lattice vector, 90-θ is the semi-apex angle of Bragg's cone.

This relationship can be mathematically written as:

$$R = \frac{S\,D}{C} \qquad \text{Equation 1-9}$$

where S is the maximum source dimension perpendicular to the plane of incidence, D is specimen film distance and C is source specimen distance.

Now let us consider the effect of source size in the direction parallel to the plane of incidence. Referring to Figure 1-2, the point P will accept X-rays (for diffraction) emanating from range of points on the source in the direction parallel to the plane of incidence (t-b-s) determined by the rocking curve width. Higher rocking curve width would mean wider acceptance angle (t-P-s) in the plane of incidence.

It can be shown by simple calculations that source dimension perpendicular to the plane of incidence is the limiting factor in determining spatial resolution rather than source dimension parallel to the plane of incidence.

We have noted before that spatial resolution depends on specimen to film distance and should be minimized; however there is limitation on resolution of photographic detectors used in topography therefore there is no added benefit in reducing specimen to film distance beyond the resolution of detector determined by grain size in the emulsion which is around 1μm. In practice specimen to film distance is set such that calculated resolution (Equation 1-10) matches with detector resolution.

1.7 Penetration depth

The penetration depth is an important concept and plays a vital role in interpreting X-ray diffraction topograph. It provides the information of the volume from which the image is generated. Penetration depth, defined for a reflection is the depth (t) at which intensity drops to 1/e. Figure 1-3 shows a reflection with a penetration depth of t.

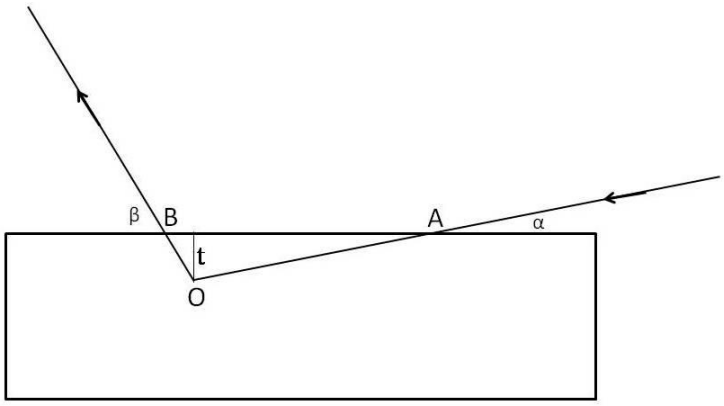

Figure 1-3: Schematic ray diagram for calculation of penetration depth.

$$OA = \frac{t}{\mathrm{cosec}(\alpha)} \qquad \text{Equation 1-10}$$

$$OB = \frac{t}{\mathrm{cosec}(\beta)} \qquad \text{Equation 1-11}$$

Therefore: $OA + OB = t\left(\frac{\mathbf{1}}{sin(\alpha)} + \frac{\mathbf{1}}{sin(\beta)}\right) = \tau$ Equation 1-12

By definition of mass absorption coefficient: $\frac{I}{I_0} = e^{-\mu\tau}$

Also by the definition of penetration depth $e^{-\mu\tau} = \frac{\mathbf{1}}{e}$

or, $\mu\tau = \mathbf{1}$

or, $\mu t\left(\frac{\mathbf{1}}{sin(\alpha)} + \frac{\mathbf{1}}{sin(\beta)}\right) = \mathbf{1}$

or, Penetration depth = $t = \frac{\mathbf{1}}{\mu\left(\frac{\mathbf{1}}{sin(\alpha)} + \frac{\mathbf{1}}{sin(\beta)}\right)}$ Equation 1-13

We have used the equation 1-14 in determining penetration depth.

Penetration depth determination and surface study of Silicon wafer using white beam synchrotron radiation topography in grazing Bragg-Laue geometry is carried out by Dudley et al. [49].

Here we have defined and determined penetration depth based on intensity dropping to 1/e. Many authors have sometimes defined penetration depth (t_{10}) when intensity drops to 1/10. In this case:

$\frac{I}{I_0} = e^{-\mu\tau} = \frac{\mathbf{1}}{\mathbf{10}}$

or, $\mu\tau = ln(\mathbf{10})$

or, $\tau = \frac{ln(\mathbf{10})}{\mu}$

or, $t_{10}\left(\frac{\mathbf{1}}{sin(\alpha)} + \frac{\mathbf{1}}{sin(\beta)}\right) = \frac{ln(\mathbf{10})}{\mu}$

or, $t_{10} = \frac{\ln(10)}{\mu\left(\frac{1}{\sin(\alpha)} + \frac{1}{\sin(\beta)}\right)} = t\ln(10)$ Equation 1-14

1.8 Contrast formation mechanism in X-ray diffraction topograph

Defects can be imaged using X-ray diffraction topography where there is measurable difference in diffracted intensity. These defects include those giving rise to localized strain field such as dislocations, subgrain boundary, grain boundary and growth sector boundaries. Contrast in an X-ray diffraction topograph is generally described by two mechanisms: orientation contrast and extinction contrast.

Orientation contrast in a X-ray diffraction topograph is the non-uniform distribution of intensity, purely arising from convergence (overlap) or divergence (separation) of diffracted rays. This contrast is seen in crystal containing small angle grain boundary, twin and grain boundary. Misorientation in lattice plane caused by residual stress can also be observed as orientation contrast. Observation of orientation contrast is the result of both the nature of X-ray and the nature of misorientation. If either the beam divergence or the wavelength bandwidth available in the incident X-ray is smaller than the misorientation between two regions, then only one region in the crystal can diffract at a time. Therefore orientation contrast is presence or absence of diffracted intensity in one of the region.

Extinction contrast is due to the difference in scattering power around the defect from rest of the crystal. Extinction contrast is mostly used for understanding and explaining images of dislocation in topographs. Image of a dislocation in a topograph consists of three different types of images: direct, dynamic and intermediary image due to three types of extinction contrast. In transmission geometry, absorption condition (μt) determines the type of image that can be observed. Where μ is the mass absorption coefficient and t is the thickness of the crystal. Near the dislocation core where the lattice is heavily distorted compared to the rest of the crystal, dynamical diffraction breaks down and the core region diffracts kinematically. The reason for rescattering being negligible is because the core region falls outside the full width at half maxima of rocking curve. This is similar to small size crystal diffraction which diffracts kinematically.

Direct dislocation image: This type of image is observed when topograph is recorded under low absorption condition $\mu t<1$. In this case diffracted intensity from dislocation core region is higher than the surrounding matrix resulting in dark dislocation line.

Dynamical dislocation image: This type of image if observed when topograph is recorded under high absorption condition $\mu t>6$. In this case dislocation line will appear as white line due to anomalous absorption also called Borrmann effect.

Intermediary dislocation image: This type of image if observed when topograph is recorded under absorption condition 6> μt>1. In intermediary absorption condition all three components can contribute. Usually these images appear as bead-line contrast along direct image.

1.9 Application of X-ray diffraction topography

Determination of dislocation line direction:

Dislocations are generally created either during growth of the crystal, post growth deformation or during processing such as slicing and dicing. Understanding of dislocation line direction is quite important in order to fully characterize the given dislocation which in turn can be used to understand its origin and prevent its occurrence. The line direction of a dislocation can be determined by analyzing by its projected image on two or more topographs with different reciprocal lattice vector [50, 51].

Determination of Burgers vector in a dislocation:

A localized strain field is associated with a dislocation. The displacements of lattice points are parallel to Burgers vector $\bar{\mathbf{b}}$. Therefore lattice planes perpendicular to $\bar{\mathbf{b}}$ are distorted whereas lattice planes parallel to $\bar{\mathbf{b}}$ are not distorted. As a result, topograph recorded from diffracting planes perpendicular to $\bar{\mathbf{b}}$ $\left(\bar{\mathbf{g}} \parallel \bar{\mathbf{b}}\right)$ will have strong contrast due to dislocation. When the topograph is recorded from diffracting planes parallel to $\bar{\mathbf{b}}$ $\left(\bar{\mathbf{g}} \perp \bar{\mathbf{b}}\right)$, the contrast due to dislocation will not be present.

This result can be used in determining Burgers vector by analyzing the contrast due to dislocation in several different topographs taken with different diffraction vector $(\bar{\mathbf{g}})$. If two reflections are found where contrast due to a dislocation is "extinct" $\left(\bar{\mathbf{g}}.\bar{\mathbf{b}} = 0\right)$ then the Burgers vector must lie along the intersection of those two planes.

A generalized criteria dislocation contrast to disappear is given by:

$\bar{\mathbf{g}} \cdot \bar{\mathbf{b}} = 0$ for screw dislocation Equation 1-15

$\bar{\mathbf{g}} \cdot \bar{\mathbf{b}} = 0$ *and* $\bar{\mathbf{g}} \cdot \bar{\mathbf{b}} \times \bar{\mathbf{l}} = 0$ for edge and mixed dislocation Equation 1-16

where $\bar{\mathbf{l}}$ is line direction of dislocation.

Determination of Burgers vector sense and magnitude:

Once the direction of the Burgers vector is determined using $(\bar{\mathbf{g}} \cdot \bar{\mathbf{b}})$ analysis, further detailed analysis is required in order to determine the Burgers vector sense and magnitude. Divergent beam technique using conventional radiation is developed by Chikawa [52] for determining sense in both screw and edge dislocation and can be further compared with theoretical calculation in order to determine magnitude of Burgers vector.

1.10 Comparison between TEM and X-ray diffraction topography

Fundamentally both the technique of TEM and X-ray diffraction topography are similar. In case of TEM, diffracted electron beam from a thin sample is imaged, whereas in case of X-ray diffraction topography, image of a diffracted X-ray beam is recorded. Both the techniques use diffraction phenomena of electron and X-rays respectively.

Dislocations can be imaged using both the techniques. TEM is used for imaging dislocations where dislocation density is high (because of high magnification) whereas X-ray topography is used for large single crystal material with very low dislocation density.

For comparison dislocation images recorded from Silicon crystal using TEM and X-ray topography is shown in Figure 1-4 below.

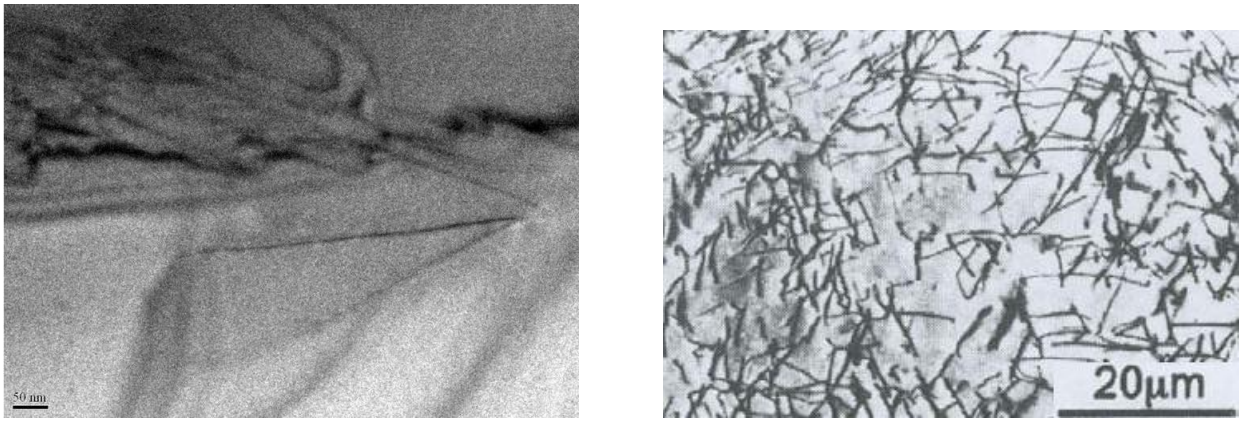

(A) (B)

Figure 1-4: Comparison of images of a dislocation in Silicon crystal recorded using A. TEM and B. X-ray topography.

X-ray topography does not provide any magnification in the imaging process whereas TEM technique provides a large magnification.

It can be seen from Figure 1-4 that the width of a dislocation image in X-ray topograph is about 3 orders of magnitude greater than width of dislocation line in TEM micrograph. The larger width of a dislocation line in X-ray topography compared to TEM is direct consequence of high strain sensitivity of X-ray topography. This can be explained from the difference in angular width of diffracting range around its plane normal. In case of X-rays Full Width at Half Maxima (FWHM) of a rocking curve is around 10^{-5} radians whereas for electron diffraction it is about 10^{-2} radians for 100 keV electrons.

Now we can qualitatively explain the wider image of dislocation in X-ray topograph and narrower electron micrograph. Image of a dislocation line is formed due to lattice plane misorientation and perfect crystal diffraction cannot take place. We know that a lattice plane misorientation around a dislocation line is inversely proportional to distance (r) away from dislocation core.

The narrower the rocking curve width (diffracting range) the further from the dislocation core the crystal will appear "misoriented".

Therefore in X-ray topography with narrower diffracting range results in a wider dislocation image and in electron micrograph with wider diffracting range results in narrower dislocation image.

Here we also note that in X-ray topography, higher order and weak reflection have narrow rocking curve width and therefore will give wider dislocation image.

1.11 Brief review of fundamental concepts in Solid Mechanics

Stress is defined at a infinitesimally small volume inside a solid material. Consider a solid object as shown in Figure 1-4. Various external forces act on the material, such that the material is in equilibrium. Consider a very small volume at an arbitrary location within the material. This volume element is defined by three sets of planes perpendicular to axis x_1, x_2 and x_3. If we consider components of force acting on these planes and divide it by the area will result in components of stress. For example: when the plane is perpendicular to axis x_2 and force component along x_3 the stress component will be σ_{23}. In general, stress tensor has nine components σ_{ij} where i and j can have value 1, 2 or 3. It can be shown that $\sigma_{ij} = \sigma_{ji}$, therefore total number of independent stress components reduces to six.

$$\sigma_{ij} = \begin{bmatrix} \sigma_{11} & \sigma_{12} & \sigma_{13} \\ \sigma_{21} & \sigma_{22} & \sigma_{23} \\ \sigma_{31} & \sigma_{32} & \sigma_{33} \end{bmatrix} \qquad \text{Equation 1-17}$$

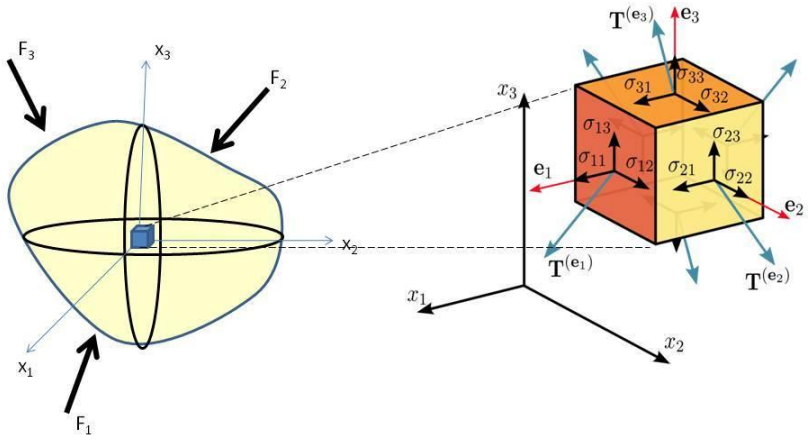

Figure 1-5: Schematic of a solid object under applied stress

Strain is a tensor defined at a location (infinitesimal small volume) in solid material as

$$\varepsilon_{ij} = \frac{1}{2}\left(\frac{\partial u_i}{\partial j} + \frac{\partial u_j}{\partial i}\right) = \begin{bmatrix} \varepsilon_{xx} & \varepsilon_{xy} & \varepsilon_{xz} \\ \varepsilon_{yx} & \varepsilon_{yy} & \varepsilon_{yz} \\ \varepsilon_{xz} & \varepsilon_{yz} & \varepsilon_{zz} \end{bmatrix} = \begin{bmatrix} \frac{\partial u_x}{\partial x} & \frac{1}{2}\left(\frac{\partial u_y}{\partial x} + \frac{\partial u_x}{\partial y}\right) & \frac{1}{2}\left(\frac{\partial u_z}{\partial x} + \frac{\partial u_x}{\partial z}\right) \\ \frac{1}{2}\left(\frac{\partial u_x}{\partial y} + \frac{\partial u_y}{\partial x}\right) & \frac{\partial u_y}{\partial y} & \frac{1}{2}\left(\frac{\partial u_z}{\partial y} + \frac{\partial u_y}{\partial z}\right) \\ \frac{1}{2}\left(\frac{\partial u_x}{\partial z} + \frac{\partial u_z}{\partial x}\right) & \frac{1}{2}\left(\frac{\partial u_y}{\partial z} + \frac{\partial u_z}{\partial y}\right) & \frac{\partial u_z}{\partial z} \end{bmatrix} \qquad \text{Equation 1-18}$$

where i, j is x, y or z and u is the displacement.

Small strain (elastic strain) is proportional to applied stress in the material. Both stress and strain can be treated as a symmetric second rank tensor. There linear dependency can be written in the concise form as:

$$\sigma_{ij} = C_{ijkl}\varepsilon_{kl} \qquad \text{Equation 1-19}$$

where C_{ijkl} is called the stiffness matrix. The above equation is the concise form known as Einstein's notation, also note that summation over k and l is implied. It is a set of nine equations

for each of the component of stress tensor. As an example, one of the stress component σ_{11} is written as:

$$\sigma_{11} = C_{1111}\varepsilon_{11} + C_{1112}\varepsilon_{12} + C_{1113}\varepsilon_{13} + C_{1121}\varepsilon_{21} + C_{1122}\varepsilon_{22} + C_{1123}\varepsilon_{23} + C_{1131}\varepsilon_{31} + C_{1132}\varepsilon_{32} + C_{1133}\varepsilon_{33}$$

Equation 1-20

The above equation is interesting and surprising. Consider an example in which C_{1113} has a non zero value. A tensile stress in the direction **1** will cause shear strain ε_{13}. Even though it is not intuitive, it is possible in single crystal with fewer symmetry elements. It can be shown by symmetry arguments that C_{1113} is zero in case of isotropic material.

The inverse of Equation 1-20 can be written as:

$$\varepsilon_{ij} = S_{ijkl}\sigma_{kl} \qquad \text{Equation 1-21}$$

where S_{ijkl} is compliance matrix.

In general there are a total of 81 constants in either compliance or stiffness matrix but there is relation between the components which leads to fewer numbers of elastic constants. Since $\varepsilon_{kl} = \varepsilon_{lk}$ and therefore the terms C_{ijkl} and C_{ijlk} will occur together in the Equation 1-20 and it is permissible to say:

$$C_{ijkl} = C_{jikl} \quad \text{Equation 1-22}$$

Next let us assume only one strain component ε_{11}, then we have

$\sigma_{12} = C_{1211}\varepsilon_{11}$ and $\sigma_{21} = C_{2111}\varepsilon_{11}$ since $\sigma_{12} = \sigma_{21}$ we have $C_{1211} = C_{2111}$.

Or in general $C_{ijkl} = C_{jikl}$ Equation 1-23

Similar arguments will lead to the relation

$$S_{ijkl} = S_{jikl} \quad \text{Equation 1-24}$$

$$S_{ijkl} = S_{jikl} \quad \text{Equation 1-25}$$

These relations reduced the total number of independent constants to 36. At this point it is convenient to use two prefix for compliance and stiffness matrix and one prefix for strain and stress as given below:

$$\begin{bmatrix} \sigma_{11} & \sigma_{12} & \sigma_{13} \\ \sigma_{21} & \sigma_{22} & \sigma_{23} \\ \sigma_{31} & \sigma_{32} & \sigma_{33} \end{bmatrix} \rightarrow \begin{bmatrix} \sigma_{1} & \sigma_{6} & \sigma_{5} \\ \sigma_{6} & \sigma_{2} & \sigma_{4} \\ \sigma_{5} & \sigma_{4} & \sigma_{3} \end{bmatrix} \quad \text{Equation 1-26}$$

Similar contraction apply for C_{ijkl} that is $C_{1123} \rightarrow C_{14}, C_{1212} \rightarrow C_{66}, C_{2213} \rightarrow C_{25}$ etc. and

$$\begin{bmatrix} \varepsilon_{11} & \varepsilon_{12} & \varepsilon_{13} \\ \varepsilon_{21} & \varepsilon_{22} & \varepsilon_{23} \\ \varepsilon_{31} & \varepsilon_{32} & \varepsilon_{33} \end{bmatrix} \rightarrow \begin{bmatrix} \varepsilon_{1} & \frac{1}{2}\varepsilon_{6} & \frac{1}{2}\varepsilon_{5} \\ \frac{1}{2}\varepsilon_{6} & \varepsilon_{2} & \frac{1}{2}\varepsilon_{4} \\ \frac{1}{2}\varepsilon_{5} & \frac{1}{2}\varepsilon_{4} & \varepsilon_{3} \end{bmatrix} \quad \text{Equation 1-27}$$

Therefore Equation 1-20 can be rewritten in the compact notation as:

$$\sigma_i = C_{ij}\varepsilon_j \text{ and } \varepsilon_i = S_{ij}\sigma_j \quad \text{Equation 1-28}$$

$$\text{or, } \begin{bmatrix} \sigma_1 \\ \sigma_2 \\ \sigma_3 \\ \sigma_4 = \sigma_{23} \\ \sigma_5 = \sigma_{31} \\ \sigma_6 = \sigma_{12} \end{bmatrix} = \begin{bmatrix} C_{11} & C_{12} & C_{13} & C_{14} & C_{15} & C_{16} \\ C_{21} & C_{22} & C_{23} & C_{24} & C_{25} & C_{26} \\ C_{31} & C_{32} & C_{33} & C_{34} & C_{35} & C_{36} \\ C_{41} & C_{42} & C_{43} & C_{44} & C_{45} & C_{46} \\ C_{51} & C_{52} & C_{53} & C_{54} & C_{55} & C_{56} \\ C_{61} & C_{62} & C_{63} & C_{64} & C_{65} & C_{66} \end{bmatrix} \begin{bmatrix} \varepsilon_1 \\ \varepsilon_2 \\ \varepsilon_3 \\ \gamma_{23} = 2\varepsilon_{23} \\ \gamma_{31} = 2\varepsilon_{31} \\ \gamma_{12} = 2\varepsilon_{12} \end{bmatrix} \quad \text{Equation 1-29}$$

Further it can also be proved that $C_{ij} = C_{ji}$ and $S_{ij} = S_{ji}$, thereby reducing the total number of independent elastic constant to 21 from 36.

Rewriting Equation 1-25 in the compact notation yields six equations for each component of stress:

$$\begin{aligned}
\sigma_{11} &= C_{11}\varepsilon_1 + C_{12}\varepsilon_2 + C_{13}\varepsilon_3 + 2C_{14}\varepsilon_{23} + 2C_{15}\varepsilon_{31} + 2C_{16}\varepsilon_{12} \\
\sigma_{22} &= C_{21}\varepsilon_1 + C_{22}\varepsilon_2 + C_{23}\varepsilon_3 + 2C_{24}\varepsilon_{23} + 2C_{25}\varepsilon_{31} + 2C_{26}\varepsilon_{12} \\
\sigma_{33} &= C_{31}\varepsilon_1 + C_{32}\varepsilon_2 + C_{33}\varepsilon_3 + 2C_{34}\varepsilon_{23} + 2C_{35}\varepsilon_{31} + 2C_{36}\varepsilon_{12} \\
\sigma_{23} &= C_{41}\varepsilon_1 + C_{42}\varepsilon_2 + C_{43}\varepsilon_3 + 2C_{44}\varepsilon_{23} + 2C_{45}\varepsilon_{31} + 2C_{46}\varepsilon_{12} \\
\sigma_{31} &= C_{51}\varepsilon_1 + C_{52}\varepsilon_2 + C_{53}\varepsilon_3 + 2C_{54}\varepsilon_{23} + 2C_{55}\varepsilon_{31} + 2C_{56}\varepsilon_{12} \\
\sigma_{12} &= C_{61}\varepsilon_1 + C_{62}\varepsilon_2 + C_{63}\varepsilon_3 + 2C_{64}\varepsilon_{23} + 2C_{65}\varepsilon_{31} + 2C_{66}\varepsilon_{12}
\end{aligned} \quad \text{Equation 1-30}$$

Total number of independent elastic constant in a material is 21. Therefore in a general crystal, having least crystallographic symmetry elements with arbitrary orientation, total number of independent elastic constant is 21. As the symmetry elements in the crystal increases, the total number of independent elastic constants decreases. As an example, if a cubic crystal oriented such that the crystal axis ([1 0 0], [0 1 0] , [0 0 1]) are parallel to the reference axis (x,y,z) respectively, the total number of independent elastic constants are 3 $\left(C_{11}=C_{22}=C_{33},\ C_{12}=C_{23}=C_{31} and\ C_{44}=C_{55}=C_{66}\right)$ and rest of the terms are zero. Another special case example would be isotropic material (e.g. non-textured, randomly oriented grains in polycrystalline material) in which total number of independent elastic constants are 2 (two).

Tensor transformation: Values of tensor components are different for different coordinate system. Elastic constants, say stiffness matrix, can be transformed to a new axes by applying standard tensor transformation equation:

$$C'_{ijkl}=a_{im}a_{jn}a_{ko}a_{lp}C_{mnop} \qquad \text{Equation 1-31}$$

where a_{ij} is the cosine of the angle between the new axis x'_i and the old axis x_j. In the above equation summation in m, n, o and p is implied i.e. after expanding the right side of the Equation 1-27, it consists of 81 terms.

At this point it is important to note that the strain/compliance/stiffness matrix in the compact notation are not a true tensor and standard tensor operation cannot be applied them (such as transformation) but stress in compact notation is a true tensor. A comprehensive table is compiled by Hearmon [53] for transformation of stiffness C_{ij} and compliance S_{ij} in contracted notation.

Elastic constants of Si crystals are [54]:

$$\mathrm{C_{11}}=\mathbf{165.7},\mathrm{C_{12}}=\mathbf{63.9}\,\mathrm{and}\,\mathrm{C_{44}}=\mathbf{79.6}\,\mathrm{GPa} \qquad \text{Equation 1-32}$$

These constants represent when the crystal is oriented such that crystallographic direction [100], [010] and [001] coincides with x, y and z axis as shown in Figure 1-6 (A).

Let us consider an example in which we calculate stiffness constant in another coordinate system. This result will be used in the next chapter for stress calculations. Here we find the components of stiffness constant when the crystal is rotated 45^0 degrees about z axis, tensor transformation is done from old axis (x,y,z) to new axis (x',y',z')

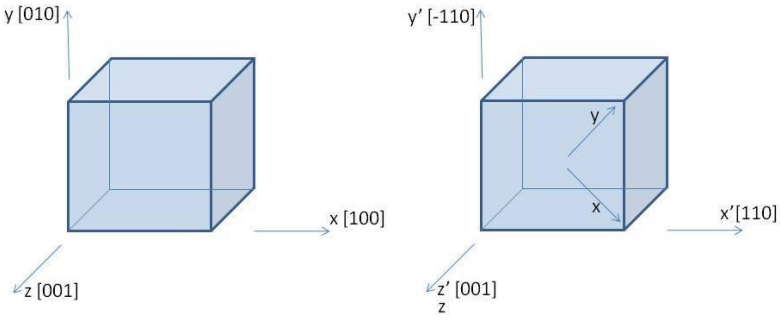

(A) (B)

Figure 1-6: Transformation of elastic constants. Stiffness matrix is known for orientation (A), for orientation (B) stiffness matrix is being determined by using tensor transformation.

We use Equation 1-29 in order to determine components of stiffness tensor. But, before we apply equation 1-29 which uses expanded notation of C_{ijkl} we need to convert the values of C_{ij} from compact notation to expanded notation.

$$\left.\begin{aligned} C_{11} &= C_{1111} \\ C_{22} &= C_{2222} \\ C_{33} &= C_{3333} \end{aligned}\right\} = \boldsymbol{165.7}$$

$$\left.\begin{aligned} C_{44} &= C_{2323} = C_{2332} = C_{3223} = C_{3232} \\ C_{55} &= C_{1313} = C_{1331} = C_{3113} = C_{3131} \\ C_{66} &= C_{2121} = C_{2112} = C_{1221} = C_{1212} \end{aligned}\right\} = \boldsymbol{79.6} \qquad \text{Equation 1-33}$$

$$\left.\begin{aligned} C_{12} &= C_{1122} = C_{2211} \\ C_{23} &= C_{2233} = C_{3322} \\ C_{31} &= C_{3311} = C_{1133} \end{aligned}\right\} = \boldsymbol{63.9}$$

Next step is to calculate the a_{ij} matrix. The relation between old coordinate system (x y z) and new coordinate system is defined using a matrix.

$$\begin{bmatrix} x' \\ y' \\ z' \end{bmatrix} = \begin{bmatrix} \cos\theta_{x'x} & \cos\theta_{x'y} & \cos\theta_{x'z} \\ \cos\theta_{y'x} & \cos\theta_{y'y} & \cos\theta_{y'z} \\ \cos\theta_{z'x} & \cos\theta_{z'y} & \cos\theta_{z'z} \end{bmatrix} \begin{bmatrix} x \\ y \\ z \end{bmatrix} \qquad \text{Equation 1-34}$$

where $\theta_{x'x}$ is the angle between x and x' etc. Therefore in our case

$$a_{ij} = \begin{bmatrix} \cos\theta_{x'x} & \cos\theta_{x'y} & \cos\theta_{x'z} \\ \cos\theta_{y'x} & \cos\theta_{y'y} & \cos\theta_{y'z} \\ \cos\theta_{z'x} & \cos\theta_{z'y} & \cos\theta_{z'z} \end{bmatrix} = \begin{bmatrix} \frac{1}{\sqrt{2}} & \frac{1}{\sqrt{2}} & \mathbf{0} \\ \frac{1}{\sqrt{2}} & \frac{1}{\sqrt{2}} & \mathbf{0} \\ \mathbf{0} & \mathbf{0} & \mathbf{1} \end{bmatrix} \qquad \text{Equation 1-35}$$

A concise Mathematica code is written to calculate the summation in equation 1-29 and to evaluate the transformed matrix. The code is given in Appendix E and the results, components of stiffness matrix after transformation are given below:

$$\begin{bmatrix} \begin{pmatrix} C_{1111} & C_{1112} & C_{1113} \\ C_{1121} & C_{1122} & C_{1123} \\ C_{1131} & C_{1132} & C_{1133} \end{pmatrix} & \begin{pmatrix} C_{1211} & C_{1212} & C_{1213} \\ C_{1221} & C_{1222} & C_{1223} \\ C_{1231} & C_{1232} & C_{1233} \end{pmatrix} & \begin{pmatrix} C_{1311} & C_{1312} & C_{1313} \\ C_{1321} & C_{1322} & C_{1323} \\ C_{1331} & C_{1332} & C_{1333} \end{pmatrix} \\ \begin{pmatrix} C_{2111} & C_{2112} & C_{2113} \\ C_{2121} & C_{2122} & C_{2123} \\ C_{2131} & C_{2132} & C_{2133} \end{pmatrix} & \begin{pmatrix} C_{2211} & C_{2212} & C_{2213} \\ C_{2221} & C_{2222} & C_{2223} \\ C_{2231} & C_{2232} & C_{2233} \end{pmatrix} & \begin{pmatrix} C_{2311} & C_{2312} & C_{2313} \\ C_{2321} & C_{2322} & C_{2323} \\ C_{2331} & C_{2332} & C_{2333} \end{pmatrix} \\ \begin{pmatrix} C_{3111} & C_{3112} & C_{3113} \\ C_{3121} & C_{3122} & C_{3123} \\ C_{3131} & C_{3132} & C_{3133} \end{pmatrix} & \begin{pmatrix} C_{3211} & C_{3212} & C_{3213} \\ C_{3221} & C_{3222} & C_{3223} \\ C_{3231} & C_{3232} & C_{3233} \end{pmatrix} & \begin{pmatrix} C_{3311} & C_{3312} & C_{3313} \\ C_{3321} & C_{3322} & C_{3323} \\ C_{3331} & C_{3332} & C_{3333} \end{pmatrix} \end{bmatrix} = \begin{bmatrix} \begin{pmatrix} 194.4 & 0 & 0 \\ 0 & 35.2 & 0 \\ 0 & 0 & 63.9 \end{pmatrix} & \begin{pmatrix} 0 & 50.9 & 0 \\ 50.9 & 0 & 0 \\ 0 & 0 & 0 \end{pmatrix} & \begin{pmatrix} 0 & 0 & 79.6 \\ 0 & 0 & 0 \\ 79.6 & 0 & 0 \end{pmatrix} \\ \begin{pmatrix} 0 & 59.9 & 0 \\ 59.9 & 0 & 0 \\ 0 & 0 & 0 \end{pmatrix} & \begin{pmatrix} 35.2 & 0 & 0 \\ 0 & 194.4 & 0 \\ 0 & 0 & 63.9 \end{pmatrix} & \begin{pmatrix} 0 & 0 & 0 \\ 0 & 0 & 79.6 \\ 0 & 79.6 & 0 \end{pmatrix} \\ \begin{pmatrix} 0 & 0 & 79.6 \\ 0 & 0 & 0 \\ 79.6 & 0 & 0 \end{pmatrix} & \begin{pmatrix} 0 & 0 & 0 \\ 0 & 0 & 79.6 \\ 0 & 79.6 & 0 \end{pmatrix} & \begin{pmatrix} 63.9 & 0 & 0 \\ 0 & 63.9 & 0 \\ 0 & 0 & 165.7 \end{pmatrix} \end{bmatrix}$$

Equation 1-36

Chapter 2 Residual stress determination in transmission geometry

2.1 Introduction

Silicon is the most widely used semiconducting material for the manufacturing of integrated circuits. Demand for higher performance has led to higher circuit density and compact design resulting in more complex manufacturing process. As a result residual stresses are unintentionally introduced in the crystal during various steps in manufacturing process and final packaging. Residual stresses are known to cause instability in electrical performance [55] and eventually kill the device if the material yields to produce dislocation. Various techniques have been used to determine residual stress in the crystal [4]. We have used the technique of white beam synchrotron X-ray diffraction topography to determine stress tensor at each point and mapped it over the entire surface [56].

We devised a novel technique to determine all the components of stress tensor in single crystal bulk material. This technique, also known as **SMART** (**S**tress **M**apping **A**nalysis via **R**ay **T**racing), is a non-destructive, non-invasive method based on the principle of X-ray diffraction imaging. This method uses the technique of **S**ynchrotron **W**hite **B**eam **X**-ray **T**opography (**SWBXT**) in combination with a fine grid made out of X-ray absorbing material and therefore, it can also be referred to as **S**ynchrotron **W**hite **B**eam **X**-ray **R**eticulography (**SWBXR**). The grid essentially breaks the area-filling X-ray beam into an array of micro-beams, each micro-beam is then traced separately. This novel technique utilizes the method of SWBXR to determine stress level at an array of points over the entire crystal area. The experiments were carried out in transmission geometry; the results are the average of the through thickness of the crystal. In the next chapter, we discuss the depth profiling in which experiments were carried out in the reflection geometry, providing stress tensor component as a function of depth. This method has a unique advantage compared with other stress measurement technique in that it can evaluate all six components of the complete stress tensor in a nondestructive way.

The hypothesis in our technique is that there exists a relationship between the state of strain in a crystal and the local plane orientation. This relationship can be exploited to determine full strain tensor as a function of position within the crystal. From the known components of strain tensor, components of stress tensor can be calculated by using the crystal's elastic

constants. Local lattice plane orientation can be measured and mapped accurately using the nondestructive technique of SWBXR. The measurement (lattice plane orientation) of three independent reflections (from three crystallographic planes) is input into the mathematical relationship between the strain tensor and the local lattice plane orientation. It allows computation of complete strain and hence stress tensor as a function of lateral position of the crystal.

X-ray reticulography is an applied technique based on the technique of X-ray diffraction topography [57-60]. Synchrotron X-ray diffraction reticulography has capability to measure angular lattice plane mis-orientation between point-to-point on a crystal with a sub-arc second angular resolution capability [57]. This technique involves placing a fine scale reticule (sometimes may be referred as grid or mesh in various literatures) in the path of incident or diffracted beam very close to the crystal. Inverse image of the grid or the "shadow" from the grid is formed due to diffraction from the crystal and is recorded on a photographic film, known as a reticulograph. A schematic of experimental setup for reticulography in a back reflection Bragg's geometry is shown in Figure 2-1. In this example, the grid partially absorbs the diffracted area-filling X-ray beam and the image is recorded in the detector. Also note that, in this example, only one reticulograph is recorded.

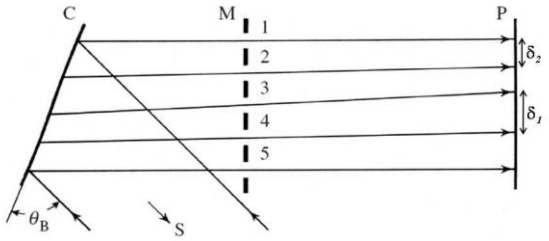

Figure 2-1: Schematic of X-ray diffraction reticulography in the back-reflection geometry. C, M, and P indicate crystal, mesh and photographic X-ray film respectively.

The grid essentially splits the area filling X-ray beam into an array of individual micro-beam. The relative divergence and convergence of individual micro-beam is determined by the relative displacement among the individual cells in the reticulograph. Figure 2-1 shows basic elements involved in an X-ray reticulographic experiment. In the figure, M represents the square mesh, C is the specimen, S is synchrotron source, and P is photographic X-ray film. Uneven

spacing ($\delta_1 > \delta_2$) between the array points in the recorded image indicates the convergence or divergence in the diffracted beam, which arises due to lattice plane misorientation.

Shape (distortion) of reticulograph under known applied stress:

In our technique, essentially we are determining residual stress from the data of recorded reticulograph. In this section we will analyze the shape of reticulograph resulting from the known stress components. Here we consider separately different stress components and the resulting distortion in the reticulograph.

Assuming that only one component of stress exists in a small volume element V within the sample and rest of the crystal is stress free. This is only a hypothetical example and such a state of stress may not be realistic. As a result of this stress, distortion in the reticulograph is shown in Figure 2-2. We have considered three different stress component, σ_{xx}, σ_{yy} and σ_{zz} individually and distortion due to them is shown in schematic of reticulograph.

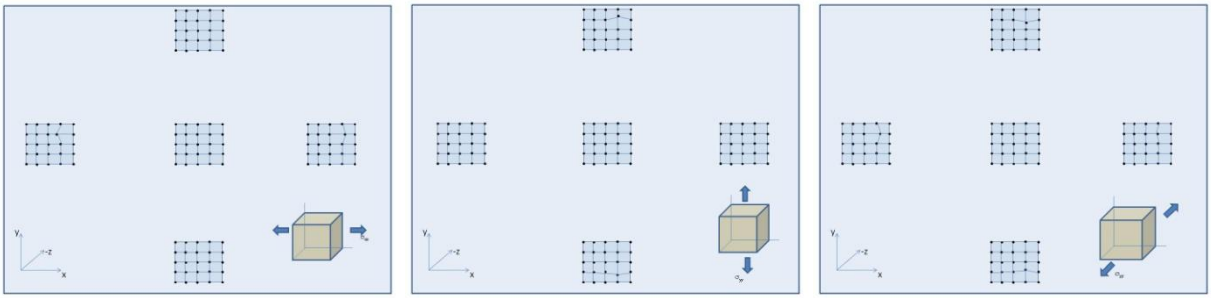

(A) (B) (C)

Figure 2-2: Schematic of distortion in a reticulograph due to various stress components. A B and C represents stress component along x, y and z direction.

2.2 Theory and mathematical principle

The underlying principle in this technique is that there is a relationship between any plane (crystallographic plane) normal and state of stress at a given location within crystal. In other words, if a stress is applied to a single crystal, not only is there a change in its lattice parameter but there is also a change in orientation in various crystallographic planes. A schematic of change in crystallographic plane orientation due to applied stress is illustrated in Figure 2-3. When normal stress σ_{yy} is applied to a single crystal, plane normal direction $\bar{n}_0$ changes to $\bar{n}$. This

is because interplaner spacing of planes perpendicular to y-axis increases and interplaner spacing of the planes perpendicular to x-axis decreases. The relationship between local state of stress or strain and local plane orientation is exploited in order to fully characterize strain or stress tensor at any general location within the crystal. Even though we are not directly measuring normal strain in y direction, we are able to detect tilt of another crystallographic plane by calculating strain in the y direction. On the reticulographic image of plane perpendicular to y-axis, there will be no significant detectable change; but on the image of plane which is perpendicular to $\bar{n}$, the shift is detectable and measurable.

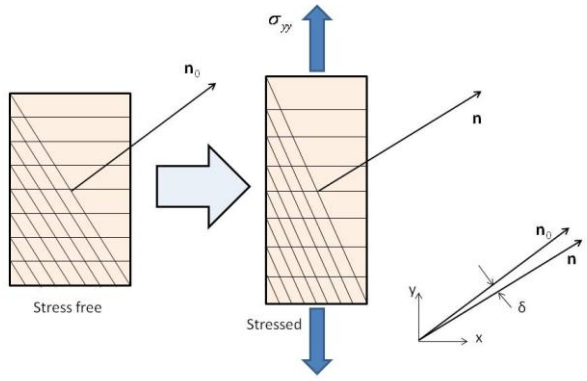

Figure 2-3: Schematic illustration of change in lattice plane orientation due to application of stress. A stress is applied to a stress free crystal (on left) and the changes in various lattice planes are shown (on right)

Traditionally lattice strain is measured by the detecting the peak shift in the intensity (I) versus Bragg's angle (2θ) diagram. A change in peak position is due to a change in lattice parameter. Since wavelength (λ) is known and constant in these measurements, strain can be calculated simply as $\frac{\Delta d}{d} = -\Delta\theta \cos\theta$. This technique only allows the measurement of the normal or the dilatational strain. In contrast to other techniques, here we are measuring lattice plane orientation at array of points in the crystal.

In our technique we have used area-filling white beam synchrotron radiation in transmission geometry in which the entire crystal is imaged. Unlike monochromatic beam, diffraction occurs from every location in the crystal, even if the crystal is highly strained locally.

Strained location is going to choose a slightly different wavelength in order to satisfy diffraction criteria. A schematic of the experimental setup is shown in Figure 2-4. Figure 2-5 illustrates the schematic of difference in reticulographs obtained from a stress free and stressed sample.

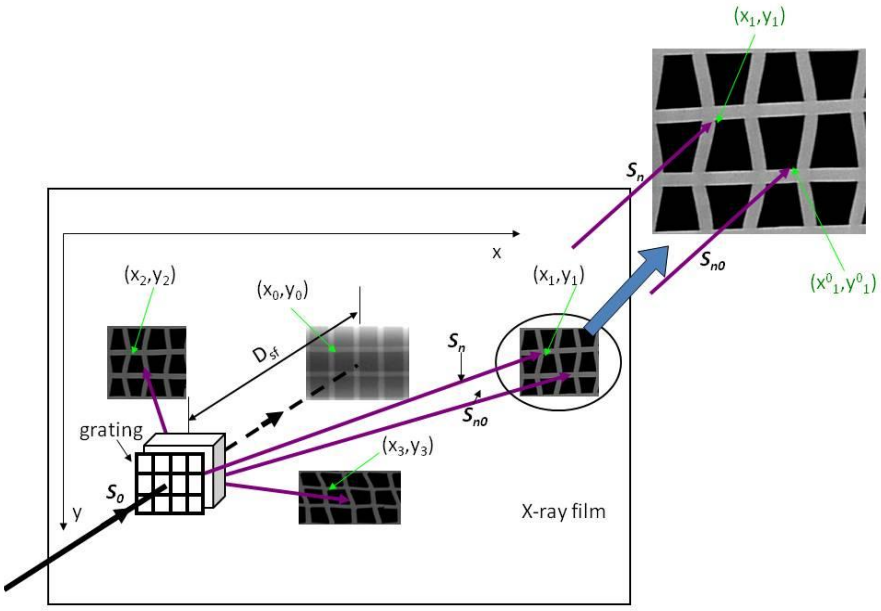

Figure 2-4: Schematic of diffraction from a strained crystal. Unlike monochromatic beam, using white beam has the advantage that the diffraction data is obtained from the entire crystal simultaneously.

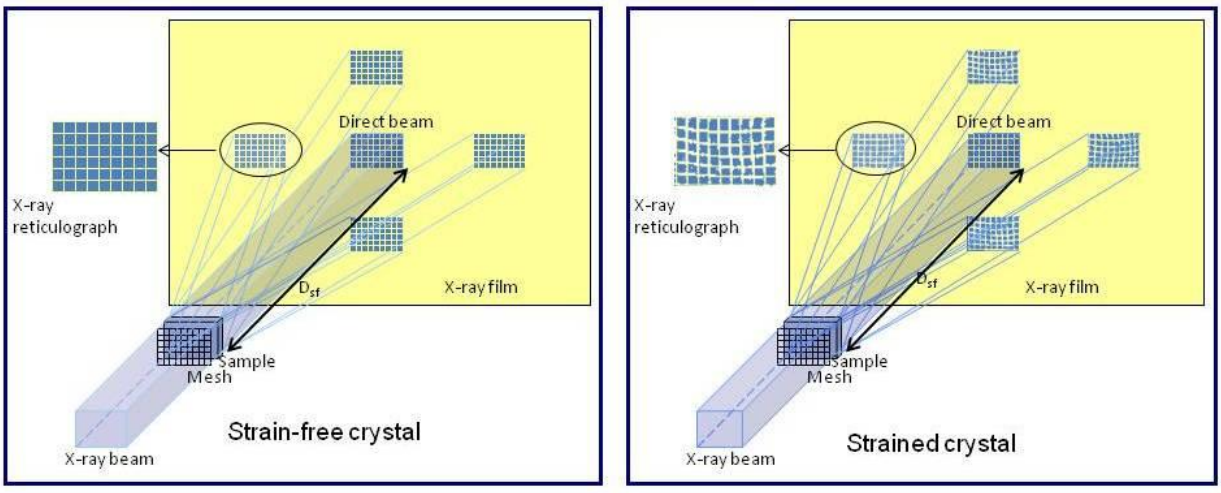

Figure 2-5: Schematic comparison of reticulographs. Left side is perfect crystal - horizontal and vertical lines are perfectly parallel and perpendicular to each other. Right side is strained crystal- distortion in the reticulographs is shown.

One of the advantages of using the white beam, as discussed earlier, is that the diffraction condition can be met at each location in the crystal. Another advantage of the white beam which really makes this technique possible is that multiple diffraction spots can be recorded simultaneously. Since the diffraction data is recorded from every location in the crystal, which essentially means residual stress can be calculated at each point in the crystal. But this is limited by the grid spacing: the finer the grid, the better spatial resolution can be achieved. In other words, stress is calculated at two distinct points defined by the grid, but the stress values/distribution between those two points is not known. In some cases where features in the device are much bigger than the grid spacing, it may be safe to assume linear stress distribution between those two stress points. The cases where feature size is comparable or smaller than the grid spacing, there may be non-linear distribution of stress between the two points. The spatial resolution of this technique is limited by the grid spacing.

Plane normal vector $\bar{n}(x, y, z)$ for any particular set of (h,k,l) plane varies continuously within the single crystal. Constant plane normal vector $\bar{n}(x, y, z)$ either implies zero stress or uniform stress. The fact that there exists a relationship between state of stress at a point within the crystal and the local lattice plane orientation has been exploited. State of stress at an arbitrary location within the crystal is a function of change in plane normal direction with respect to the stress-free location of any three general planes. In general form this relationship can be written as:

$$\sigma_{ij}(x,y,z) = f\left(\bar{n}_1(x,y,z), \bar{n}_2(x,y,z), \bar{n}_3(x,y,z), \bar{n}_0(x_0, y_0, z_0)\right) \qquad \text{Equation 2-1}$$

where $\bar{n}_1(x,y,z)$, $\bar{n}_2(x,y,z)$ and $\bar{n}_3(x,y,z)$ are plane normal vector at a location (x,y,z) of the crystallographic plane 1, 2 and 3 respectively and $\bar{n}_0(x_0,y_0,z_0)$ is the plane normal vector at a

stress free location (x_0, y_0, z_0). Plane normal vector at a point in the crystal can be detected and measured by using X-ray microbeam incident on a crystal and recording a Laue pattern.

Consider a plane "A" which is distorted due to stress, as shown in Figure 2-6. When there is no strain, assume that the perfect plane is perpendicular to the z-axis. When the plane is distorted, the plane normal vector also changes direction. Plane normal vector $\bar{n}$ continuously changes direction from one point to another. Discontinuity in plane normal implies a grain boundary.

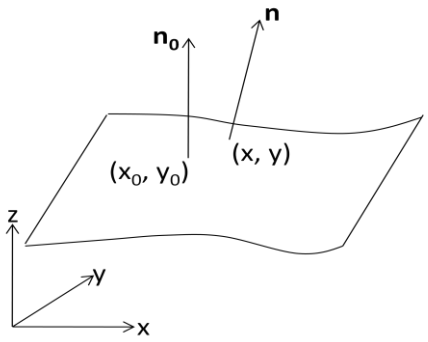

Figure 2-6: A schematic representation of a distorted crystallographic plane. Plane is perpendicular to z axis in undistorted condition, after distortion this plane is warped and the plane normal vector is different at different location on the surface. $\bar{n}_0$ is the plane normal vector at a strain free location and $\bar{n}(x, y, z)$ is the plane normal vector at any general (strained) location (x, y, z)

Plane normal vector at any general (strained) location $\bar{n}(x, y, z)$ is related to plane normal at strain free location $(\bar{n}_0)$ by the equation:

$$\bar{n}(x, y, z) = \bar{n}_0 - \nabla\left[\bar{n}_0 . \bar{u}(x, y, z)\right] \qquad \text{Equation 2-2}$$

where $\bar{u}(x, y, z)$ is the displacement vector at a location (x, y, z)

Equation 2-2 is the central equation in our analysis and stress determination. The theory and the proof of SMART technique is based on the Equation 2-2. This equation is the direct

result of Taylor expansion, the proof of this equation is given in Appendix A. A schematic representation of Equation 2-2 is given in Figure 2-7. In this particular example, the top half of the crystal has undergone distortion (strain) which is shown by the tilt in the lattice plane. The displacement vector is along x-axis, which increases linearly as y increases.

$$\bar{u} = k\left(y - y_0\right)\hat{i}$$

where k and y_0 are constants.

Also note that the plane normal vector $\bar{n}_0$ is along x direction i.e. $\bar{n}_0 = \hat{i}$, and therefore $\bar{n}_0 \cdot \bar{u} = k\left(y - y_0\right)$. The gradient of $\bar{n}_0 \cdot \bar{u}$ is along y axis as shown in Figure 2-7 or,

$$\bar{\nabla}\left(\bar{n}_0 \cdot \bar{u}\right) = k\,\hat{j}$$

It should be noted here that Equation 2-2 is a vector equation and can be split into three scalar component equations.

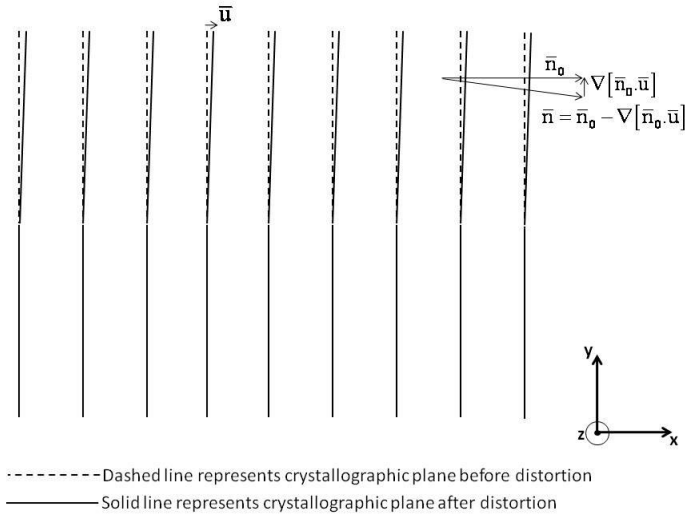

Figure 2-7: 2-D schematic of plane normal variation and its relationship to the divergence of displacement component.

Writing $\bar{n}_0$ and $\bar{u}$ in terms of its scalar components:

$$\bar{n}_0 = n_{0x}\hat{i} + n_{0y}\hat{j} + n_{0z}\hat{k}$$ Equation 2-3

$$\bar{u} = u_x\hat{i} + u_y\hat{j} + u_z\hat{k}$$ Equation 2-4

Since $\bar{n}_0$ is constant and can be taken out of derivative term, Equation 2-2 can be expanded to its x, y and z components:

$$n_x\hat{i} + n_y\hat{j} + n_z\hat{k} = n_{0x}\hat{i} + n_{0y}\hat{j} + n_{0z}\hat{k} - n_{0x}\left(\frac{\partial u_x}{\partial x}\hat{i} + \frac{\partial u_x}{\partial y}\hat{j} + \frac{\partial u_x}{\partial z}\hat{k}\right) - n_{0y}\left(\frac{\partial u_y}{\partial x}\hat{i} + \frac{\partial u_y}{\partial y}\hat{j} + \frac{\partial u_y}{\partial z}\hat{k}\right) - n_{0z}\left(\frac{\partial u_z}{\partial x}\hat{i} + \frac{\partial u_z}{\partial y}\hat{j} + \frac{\partial u_z}{\partial z}\hat{k}\right)$$

Equation 2-5

Equating i, j and k components:

$$n_x = n_{0x} - n_{0x}\frac{\partial u_x}{\partial x} - n_{0y}\frac{\partial u_y}{\partial x} - n_{0z}\frac{\partial u_z}{\partial x}$$ Equation 2-6

$$n_y = n_{0y} - n_{0x}\frac{\partial u_x}{\partial y} - n_{0y}\frac{\partial u_y}{\partial y} - n_{0z}\frac{\partial u_z}{\partial y}$$ Equation 2-7

$$n_z = n_{0z} - n_{0x}\frac{\partial u_x}{\partial z} - n_{0y}\frac{\partial u_y}{\partial z} - n_{0z}\frac{\partial u_z}{\partial z}$$ Equation 2-8

These set of three equations can be written in the form of a matrix equation using the dot product:

$$\begin{bmatrix} n_x \\ n_y \\ n_z \end{bmatrix} = \begin{bmatrix} n_{0x} \\ n_{0y} \\ n_{0z} \end{bmatrix} - \begin{bmatrix} \frac{\partial u_x}{\partial x} & \frac{\partial u_y}{\partial x} & \frac{\partial u_z}{\partial x} \\ \frac{\partial u_x}{\partial y} & \frac{\partial u_y}{\partial y} & \frac{\partial u_z}{\partial y} \\ \frac{\partial u_x}{\partial z} & \frac{\partial u_y}{\partial z} & \frac{\partial u_z}{\partial z} \end{bmatrix} \bullet \begin{bmatrix} n_{0x} \\ n_{0y} \\ n_{0z} \end{bmatrix}$$ Equation 2-9

The aforementioned equations 2-6, 2-7, 2-8 are the underlying equation in our technique. These three equations contain nine (9) derivative terms:

$\frac{\partial u_x}{\partial x}, \frac{\partial u_y}{\partial x}, \frac{\partial u_z}{\partial x}, \frac{\partial u_x}{\partial y}, \frac{\partial u_y}{\partial y}, \frac{\partial u_z}{\partial y}, \frac{\partial u_x}{\partial z}, \frac{\partial u_y}{\partial z}, \frac{\partial u_z}{\partial z}$. Once these nine terms are calculated, strain can easily be determined using equation 2-12.

For convenience we define the all the nine derivative terms in form of matrix:

$$u_{ij} = \frac{\partial u_i}{\partial j} = \begin{bmatrix} \frac{\partial u_x}{\partial x} & \frac{\partial u_y}{\partial x} & \frac{\partial u_z}{\partial x} \\ \frac{\partial u_x}{\partial y} & \frac{\partial u_y}{\partial y} & \frac{\partial u_z}{\partial y} \\ \frac{\partial u_x}{\partial z} & \frac{\partial u_y}{\partial z} & \frac{\partial u_z}{\partial z} \end{bmatrix} \quad \text{where } i, j \in x, y \text{ or } z \qquad \text{Equation 2-10}$$

Therefore the most important part of our problem is to calculate the nine (9) displacement-derivative terms. These terms are invariant, meaning they are independent of the crystallographic planes used for measurement. But these values depend on the choice of coordinate system and can be determined for different coordinate system by using tensor transformation.

In our experimental technique, multiple diffraction spots (reticulographs) are recorded simultaneously. Each diffraction spot represents reflection from an independent crystallographic plane. In the three equations stated above (2-6, 2-7, 2-8), plane normal vector components $\left(n_x, n_y, n_z\right)$ are calculated experimentally by location of diffraction spot on the topograph. If we choose three independent reticulographs, we can generate nine independent linear equations which can be solved simultaneously to determine all nine (9) displacement-derivative terms.

Given below is a set of nine (9) equations (equations 2-11 a to i) generated by using three reticulographs. Three set of equations are generated from each reticulographic image.

Stress free location is estimated by inspecting the reticulographs, where the grid intersecting lines are not distorted with respect to the rest of the crystal. Given the geometry of the experimental setup (specimen to film distance), plane normal vector can be determined. A detailed description of the procedure is given in the experimental method section of this chapter.

By determining the local plane normal vectors $\left(\bar{n}_1, \bar{n}_2 \text{ and } \bar{n}_3\right)$ at a particular location in the crystal, one can determine all the components of matrix $\frac{\partial u_i}{\partial j}$ (where i,j belongs to x,y or z) by solving equations 2-11 a to i and hence determine strain and stress tensor at that location.

$$n_{1x} = n^{0}_{1x} - \left(n^{0}_{1x} \frac{\partial u_x}{\partial x} + n^{0}_{1y} \frac{\partial u_y}{\partial x} + n^{0}_{1z} \frac{\partial u_z}{\partial x} \right) \quad \text{Equation 2.11a}$$

$$n_{1y} = n^{0}_{1y} - \left(n^{0}_{1x} \frac{\partial u_x}{\partial y} + n^{0}_{1y} \frac{\partial u_y}{\partial y} + n^{0}_{1z} \frac{\partial u_z}{\partial y} \right) \quad \text{Equation 2.11b}$$

$$n_{1z} = n^{0}_{1z} - \left(n^{0}_{1x} \frac{\partial u_x}{\partial z} + n^{0}_{1y} \frac{\partial u_y}{\partial z} + n^{0}_{1z} \frac{\partial u_z}{\partial z} \right) \quad \text{Equation 2.11c}$$

$$n_{2x} = n^{0}_{2x} - \left(n^{0}_{2x} \frac{\partial u_x}{\partial x} + n^{0}_{2y} \frac{\partial u_y}{\partial x} + n^{0}_{2z} \frac{\partial u_z}{\partial x} \right) \quad \text{Equation 2.11d}$$

$$n_{2y} = n^{0}_{2y} - \left(n^{0}_{2x} \frac{\partial u_x}{\partial y} + n^{0}_{2y} \frac{\partial u_y}{\partial y} + n^{0}_{2z} \frac{\partial u_z}{\partial y} \right) \quad \text{Equation 2.11e}$$

$$n_{2z} = n^{0}_{2z} - \left(n^{0}_{2x} \frac{\partial u_x}{\partial z} + n^{0}_{2y} \frac{\partial u_y}{\partial z} + n^{0}_{2z} \frac{\partial u_z}{\partial z} \right) \quad \text{Equation 2.11f}$$

$$n_{3x} = n^{0}_{3x} - \left(n^{0}_{3x} \frac{\partial u_x}{\partial x} + n^{0}_{3y} \frac{\partial u_y}{\partial x} + n^{0}_{3z} \frac{\partial u_z}{\partial x} \right) \quad \text{Equation 2.11g}$$

$$n_{3y} = n^{0}_{3y} - \left(n^{0}_{3x} \frac{\partial u_x}{\partial y} + n^{0}_{3y} \frac{\partial u_y}{\partial y} + n^{0}_{3z} \frac{\partial u_z}{\partial y} \right) \quad \text{Equation 2.11h}$$

$$n_{3z} = n^{0}_{3z} - \left(n^{0}_{3x} \frac{\partial u_x}{\partial z} + n^{0}_{3y} \frac{\partial u_y}{\partial z} + n^{0}_{3z} \frac{\partial u_z}{\partial z} \right) \quad \text{Equation 2.11i}$$

Solving equations 2-11a, 2-11d and 2-11g simultaneously, (i component) we get

$$\frac{\partial u_x}{\partial x}, \frac{\partial u_y}{\partial x} \& \frac{\partial u_z}{\partial x}$$

Solving equations 2-11b, 2-11e and 2-11h simultaneously, (j component) we get

$$\frac{\partial u_x}{\partial y}, \frac{\partial u_y}{\partial y} \& \frac{\partial u_z}{\partial y}$$

Solving equations 2-11c, 2-11f and 2-11i simultaneously, (k component) we get

$$\frac{\partial u_x}{\partial z}, \frac{\partial u_y}{\partial z} \& \frac{\partial u_z}{\partial z}$$

Once the matrix u_{ij} is fully determined, strain tensor can be calculated using this matrix.

Strain tensor ε_{ij} is calculated according to the Equation 1-19.

From the values of strain components, all the values of stress components can be calculated using Equation 1-20. In order to demonstrate our technique we have used a Silicon die (packaged IC) as a test sample to calculate residual stress. Details of the experimental techniques and results are discussed in the next section.

2.3 Experimental method

In this section, experimental steps used for determining residual stress in transmission X-ray diffraction mode are described. The test specimen used is a packaged IC Silicon die. An area filling synchrotron white beam is used for recording reticulographs in the experiments. Synchrotron experiments were carried out at NSLS beamline X-19C located at Brookhaven National Laboratory (BNL). As the name implies, in transmission mode, X-ray interacts with the entire crystal volume by passing through the thickness of the material. Data obtained by transmission method represents the average value over the entire sample depth represented by the Equation 2-12.

$$\left\langle \sigma_{ij} \right\rangle = \int_{0}^{t} \sigma_{ij}(z)\,dz \qquad \text{Equation 2-12}$$

A schematic of experimental setup is shown in Figure 2-4 and 2-5, topographs are recorded in the transmission geometry. A grid is placed on the incoming side of the synchrotron beam. The grid effectively splits the area filling beam into an array of square shaped micro-beams. The purpose of the grid is to locate points on the crystal to the corresponding points in reticulographs. Corner points of all the micro-beam represent a set of points forming an array. Figure 2-8 shows the schematic of splitting of X-ray by the grid. Grid is made out of X-ray absorbing material tungsten. A complete design and description of the grid used for the experiment is given in the Appendix [B].

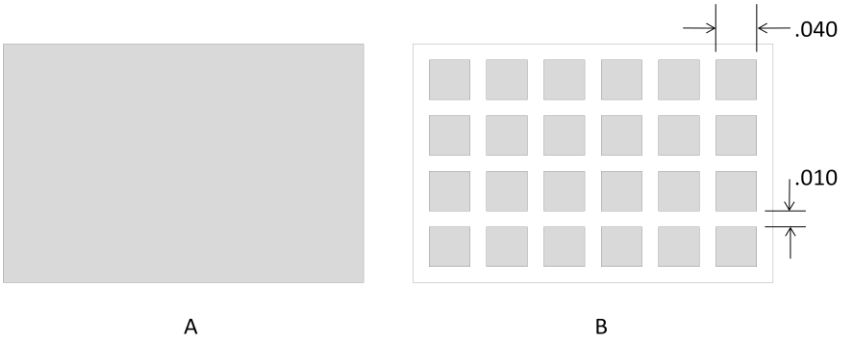

Figure 2-8: Schematic of an area filling x-ray beam (A) is split into an array microbeams (B) by placing a grid in the path of incident beam. Filled area with grey color represents x-ray and the white region is where the X-rays are absorbed by the grid. The corner points of small square is located in the reticulographic image from which diffracted beam direction is determined.

X-ray reticulographs are recorded at a particular specimen to film distance. In our experiments we have used specimen to film distance of 8cm. Multiple diffracted spots (reticulographs) are recorded simultaneously on photographic film Agfa Structurix D3-SC. Following the exposure to X-ray, the film is developed, fixed, washed and dried. Finally the film is scanned at a high resolution in an electronic Tagged Image File Format (.TIFF file). Films were scanned at a resolution of 2400 dpi (dots per inch). A typical image of the film is given in Figure 2-11. Figure 2-13 shows magnified view of the reticulographs and the radiograph used for calculations.

Care has to be taken while choosing the reticulographs, the images must be clear enough to distinguish the pattern features produced by the grid. Three reticulographs were chosen such that they do not belong to the same zone. In this particular example, three reticulographs chosen are: -2 4 2, 2 4 2, 4 2 2 as indicated in the Figure 2-13.

Unit plane normal vector of these three planes are:

$$\bar{n}_1 = \frac{1}{\sqrt{24}}\left(-2\mathrm{i} + 4\mathrm{j} + 2\mathrm{k}\right)$$
$$\bar{n}_2 = \frac{1}{\sqrt{24}}\left(2\mathrm{i} + 4\mathrm{j} + 2\mathrm{k}\right)$$
$$\bar{n}_3 = \frac{1}{\sqrt{36}}\left(4\mathrm{i} + 2\mathrm{j} + 4\mathrm{k}\right)$$

$$V = \left|\bar{n}_1 \times \bar{n}_2 \cdot \bar{n}_3\right| = \left| \frac{1}{\sqrt{24}\sqrt{24}\sqrt{36}} \begin{vmatrix} -2 & 4 & 2 \\ 2 & 4 & 2 \\ 4 & 2 & 4 \end{vmatrix} \right| = \frac{1}{6} \neq 0$$

Since the above determinant is not zero, these three planes do not belong to the same zone and hence can be used for calculations.

Specimen to film distance (sfd) should be optimized during the experiment. Too small sfd may lead to overlapping of reticulographs and too large sfd can cause diffracted spots to go outside of film area.

Exposure time should also be chosen properly, over-exposure to X-rays can cause darkening of the film due to noise and will reduce the contrast and the image quality. Underexposure can lead to poor contrast and the features may not be distinguishable.

Lead thickness used for blocking the direct beam is important in experiment. Thin Lead piece attached to the X-ray film acts as a partial beam stop. Thin piece of Lead is used because the image of the radiograph is also used in calculation of diffraction vector. Without the Lead piece the image will be too dark at the center where the direct beam after passing through Silicon sample hits the film. Similarly with the use of too thick Lead piece the image of the radiograph cannot be seen.

In case where sample size is larger than the area of the X-ray beam, scanning method is to be used. In the scanning method, sample, grid and the film are connected together such that they move together and the sample stage is scanned across the X-ray beam as shown in Figure 2-9. The exposure time in this geometry is determined by the scanning velocity (v) and the height of incident beam height (h).

$$\text{Exposure time} = t = \frac{h}{v} \qquad \text{Equation 2-13}$$

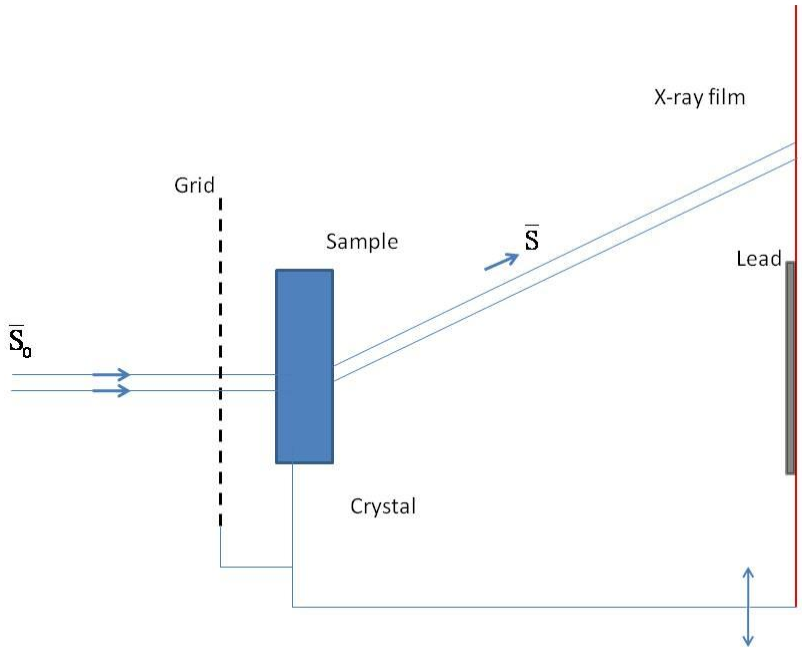

Figure 2-9: Schematic of scanning geometry. It is used when the beam size is unable to fully cover the sample. In this geometry the sample, grid and the film are attached rigidly that is there is no relative movement among them as the assembly moves from top to bottom. This can be achieved by mounting sample, grid and the film on the same stage.

Next step in the calculation is to evaluate plane normal vector at each array point defined by the grid. This can be calculated simply by subtracting incident beam unit vector $\bar{S}_0$ from diffraction unit vector $\bar{S}$ and as shown in Figure 2-10.

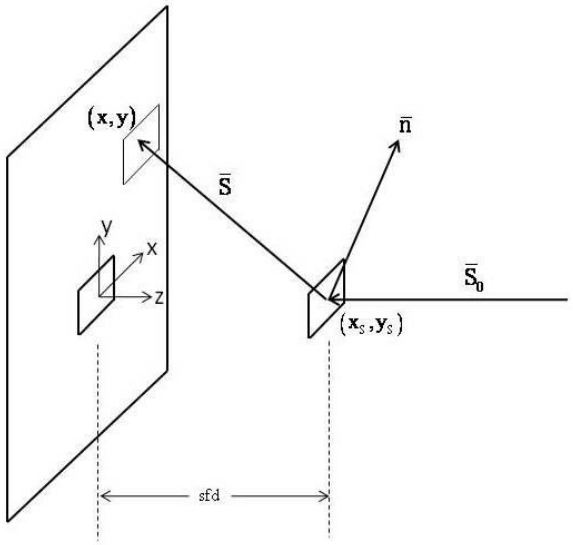

Figure 2-10: Schematic of diffraction in transmission geometry, incident beam vector $\bar{S}_0$, diffracted beam vector $\bar{S}$ and plane normal vector $\bar{n}$ are shown. Axis of reference is chosen such that the origin is defined somewhere arbitrarily on the sample and z axis is perpendicular to the plane of the film. Therefore the z coordinate of any point in the film is -(sfd)

Assuming (x, y) is a grid-corner array point on a reticulograph and (x_S, y_S) is the corresponding point on the sample surface.

$$\bar{S} = \frac{(x - x_S)\hat{i} + (y - y_S)\hat{j} - (sfd)\hat{k}}{\sqrt{(x - x_S)^2 + (y - y_S)^2 + sfd^2}} \qquad \text{Equation 2.14}$$

$$\bar{S}_0 = -\hat{k} \qquad \text{Equation 2-15}$$

$$\bar{n} = \frac{\bar{S} - \bar{S}_0}{\left|\bar{S} - \bar{S}_0\right|} \qquad \text{Equation 2-16}$$

Where $\bar{S}_0$ = Unit incident beam vector $= -\hat{k}$

$\bar{S}$ = Unit diffraction beam vector

$\bar{n}$ = Plane unit normal vector

(x, y) = Coordinates of point on the film where diffracted beam intersects the film

(x_S, y_S) = Corresponding points of (x, y) on the sample surface.

sfd = Specimen to film distance

(x, y, z) → Coordinate system defined such that origin is on the film surface and z axis is perpendicular to film.

From the recorded reticulographs, diffraction vector and the plane normal vector is calculated at each array points on the crystal. This calculation is done for three different reticulographic images.

Plane normal vectors $(\bar{n}_1, \bar{n}_2, \bar{n}_3)$ of three independent crystallographic planes $(\mathbf{1}, \mathbf{2}, \mathbf{3})$ are determined at each array point on the crystal. By inspecting the reticulographs, a stress free (or relatively low stress) location is determined. Assume stress free location on the crystal is $(x_0, y_0, -sfd)$. Using equation 2-11 a to i, the complete nine components of $\frac{du_i}{dj} = [u_{ij}]$ (where i, j are x, y or z) tensor is determined at each array point in the crystal. From $\frac{du_i}{dj}$ tensor, strain ans stress tensors are calculated using Equation 1-17 and Equation 1-18 respectively.

From the strain tensor, stress can be calculated using the elastic constants of silicon. In case of Si stiffness matrix is C_{11}=165.7GPa, C_{44}=79.6GPa and C_{12}=63.9 GPa [54]. Stress tensor is determined at each array point. Note that these components are valid when the reference axis (x,y,z) is parallel to the crystallographic axis [100], [010] and [001] respectively. We have to transform the stiffness matrix components for the new set of axis where $x' \rightarrow [110]$, $y' \rightarrow [\bar{1}10]$ and $z' \rightarrow [001]$. Referring to Section 1-12 and Appendix E, a procedure for transformation of axis and calculations are given. We have C_{ij} matrix (which is not a true tensor) for the new set of axis $[x', y', z']$ given by:

$$\begin{bmatrix} 194.4 & 35.2 & 194.4 & 0 & 0 & 0 \\ 35.2 & 194.4 & 63.9 & 0 & 0 & 0 \\ 194.4 & 63.9 & 165.7 & 0 & 0 & 0 \\ 0 & 0 & 0 & 50.9 & 0 & 0 \\ 0 & 0 & 0 & 0 & 79.6 & 0 \\ 0 & 0 & 0 & 0 & 0 & 79.6 \end{bmatrix} GPa$$

Therefore the six set of equation xyz, is written as:

$$\sigma_{11} = 194.4\varepsilon_1 + 35.2\varepsilon_2 + 194.4\varepsilon_3 \qquad \text{Equation } 2-17a$$
$$\sigma_{22} = 35.2\varepsilon_1 + 194.4\varepsilon_2 + 63.9\varepsilon_3 \qquad \text{Equation } 2-17b$$
$$\sigma_{33} = 194.4\varepsilon_1 + 63.9\varepsilon_2 + 165.7\varepsilon_3 \qquad \text{Equation } 2-17c$$
$$\sigma_{23} = 2*50.9\varepsilon_{23} \qquad \text{Equation } 2-17d$$
$$\sigma_{31} = 2*79.6\varepsilon_{31} \qquad \text{Equation } 2-17e$$
$$\sigma_{12} = 2*79.6\varepsilon_{12} \qquad \text{Equation } 2-17f$$

Even though the calculations are relatively straightforward as it involves solving simple linear equations, but the large amount of data requires us to use a computer program. A computer code is written in Mathematica for strain and stress computation. Initially the code calculates the plane normal vector at each array points for three different crystallographic planes. Coordinate points of three reticulographs and a radiograph are input to the program in the form of text files. Once the plane normal vectors are calculated and the stress free region is identified, nine linear equations can be readily solved for nine unknown terms. Finally strain and stress components are readily calculated using equations 1-19 and 2-17. The Mathematica code is also extended to calculate principal stresses and rotational components. A copy of the code is given in Appendix G.

2.4 Results and discussion

A typical X-ray film recorded from packaged silicon die is shown in Figure 2-11 and the corresponding simulated Laue pattern generated using software LauePt [48]. A magnified image of three reticulographs used for the calculations and the radiograph are shown in the Figure 2-13. Since white beam is used, multiple reticulographs are recorded in single exposure. It can be seen in the Figure 2-13 that the reticulographs are highly distorted compared to the sample dimension.

Heavy distortion of the grid lines in the reticulographs implies high distortion in crystallographic plane or high residual strain. This uneven distortion in the reticulograph indicates non-homogeneous distribution of strain. In the ideal case when there is no lattice distortion the reticulographs will have almost same shape and size as radiograph.

To determine plane normal before distortion, a minimum stress point is selected that exhibited the least distortion or no distortion in all the reticulographs. As described previously the coordinate points of grid intersection corner is calculated in three reticulographs and the radiograph. These coordinate data are which is saved as text file, is input to the Mathematica program. Strain and stress values are calculated at an array of points on the crystal. Strain and stress maps are generated from these values are shown in Figure 2-14 and 1-15 respectively.

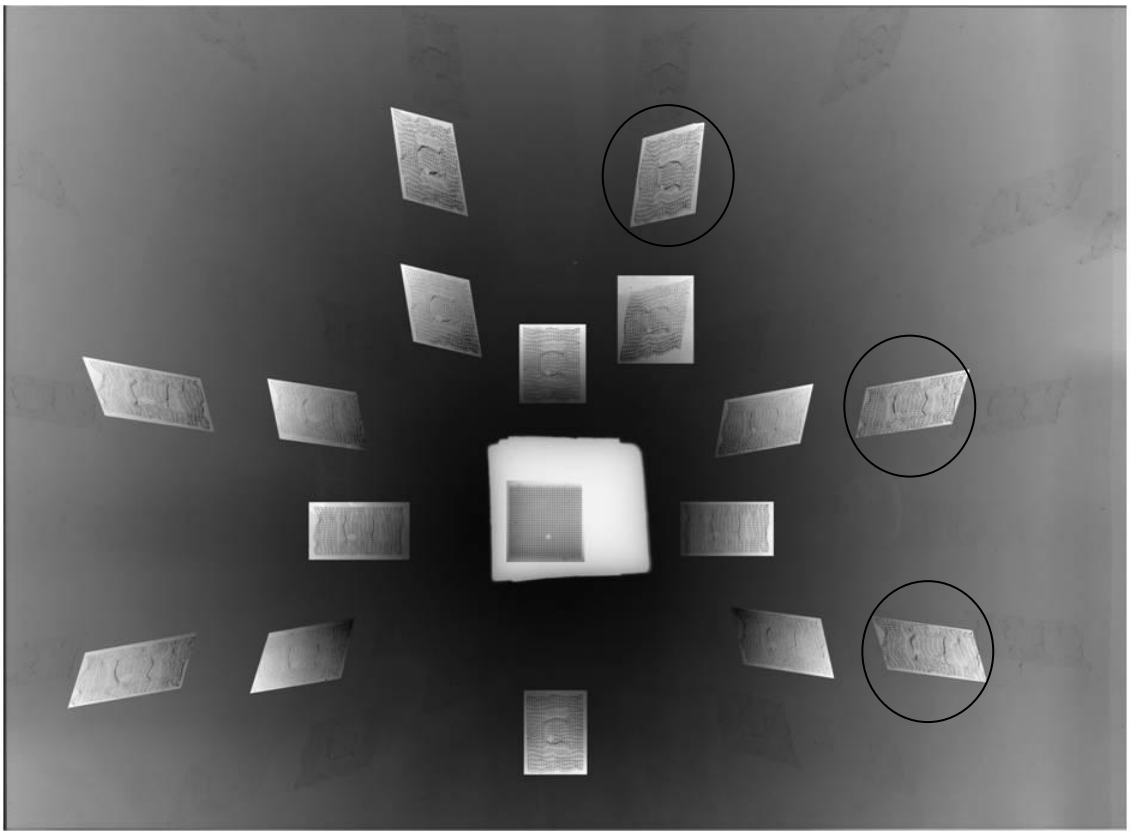

Figure 2-11: A scan of the X-ray film with recorded Laue pattern in transmission mode. Three chosen reticulogtaphs are indicated.

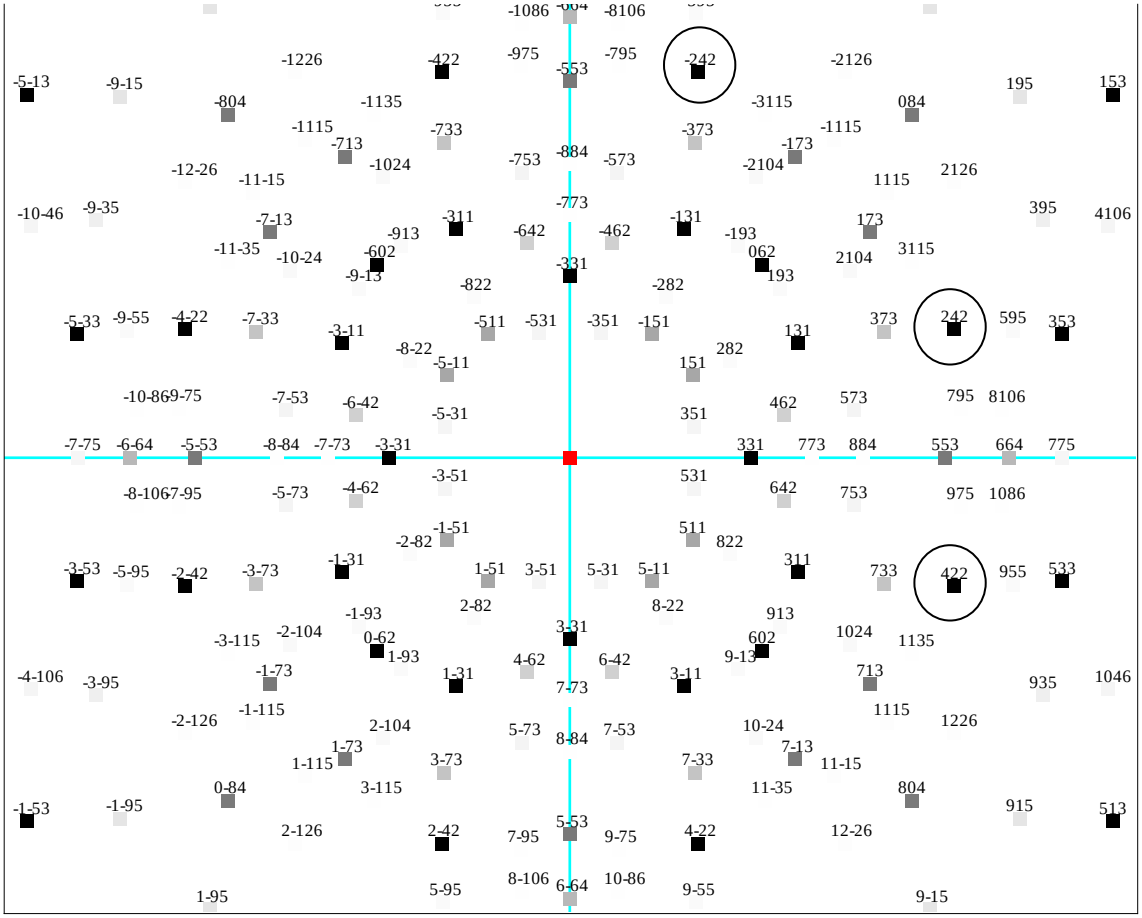

Figure 2-12: Simulated Laue pattern using program LauePt . Front surface plane facing the beam is (0 0 1) and the right side plane is (1 1 0). This simulated pattern is used as comparision with the recorded topograph and also for indexing the pattern.

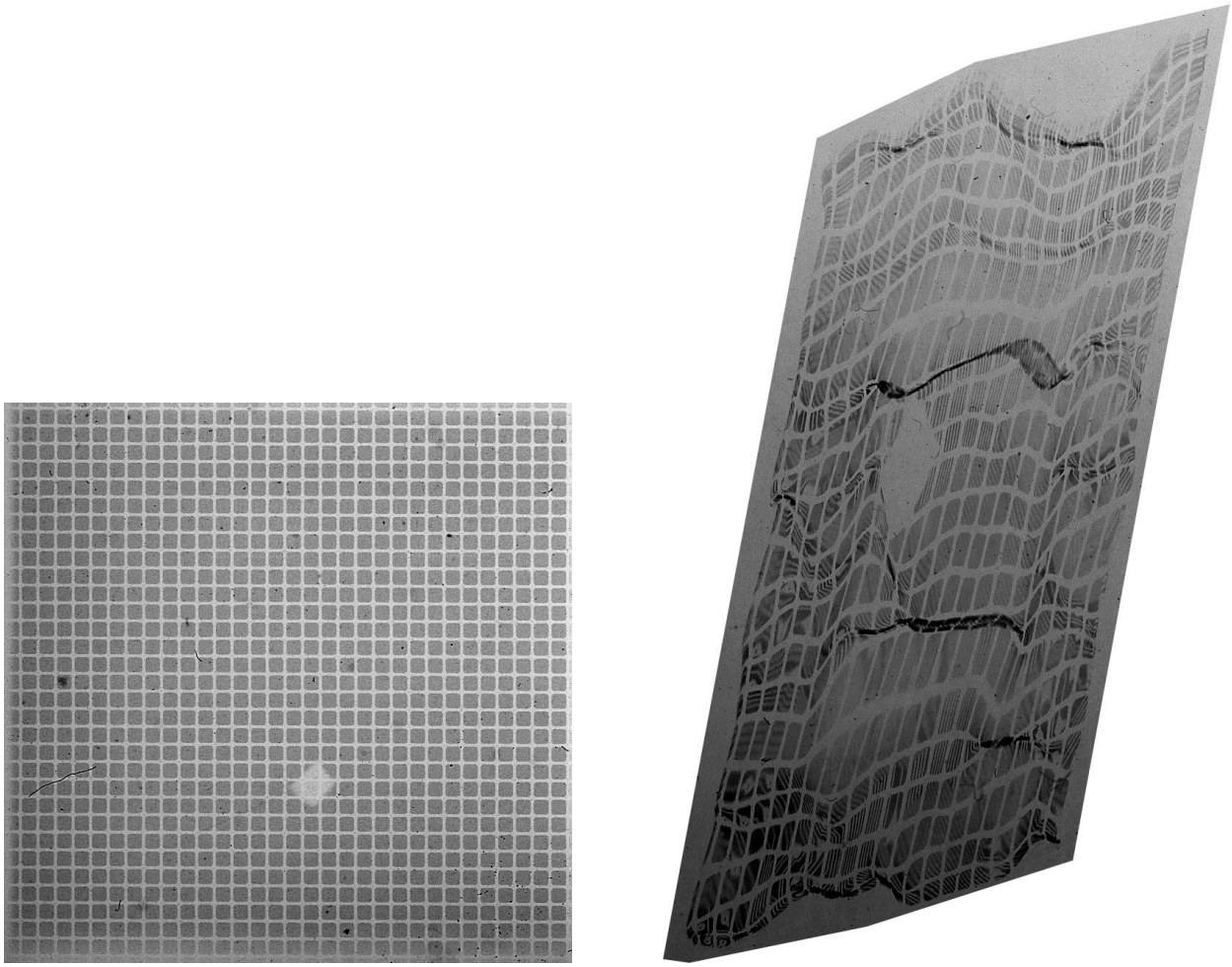

(A) (B)

(C) (D)

Figure 2-13: Magnified image of reticulographs and radiographs used for calculation. (A) Radiograph, (B) g= -2 4 2, λ=.91 (C) g= 2 4 2, λ=.91 (D) g= 4 2 2, λ=.91

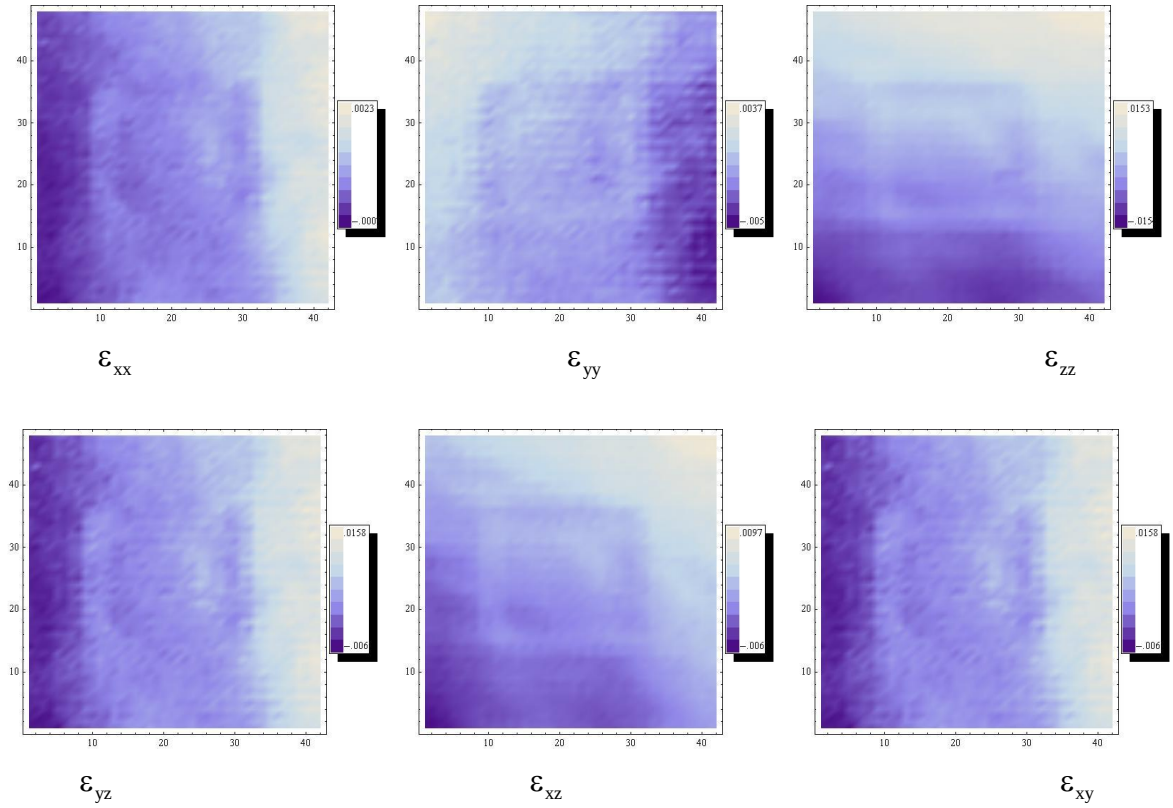

Figure 2-14: Strain maps generated using data in transmission geometry

All the six components of residual strain are mapped over the crystal area. This strain value represents the average strain value over the thickness of the crystal (Equation 2-12) or in other words strain variation along the thickness of crystal is ignored. A more detailed depth profiling method strain variation as a function of depth is considered in next chapter.

Maximum and minimum value (variation) of strain is given in Table 2-1 below.

Table 2-1: Maximum and minimum value (variation) of strain

	ε_{xx}	ε_{yy}	ε_{zz}	ε_{yz}	ε_{xz}	ε_{xy}
Minimum	-.0007	-.0052	-.0145	-.0063	-.0065	-.0093
Maximum	.0023	.0037	.0153	.0158	.0097	.0139

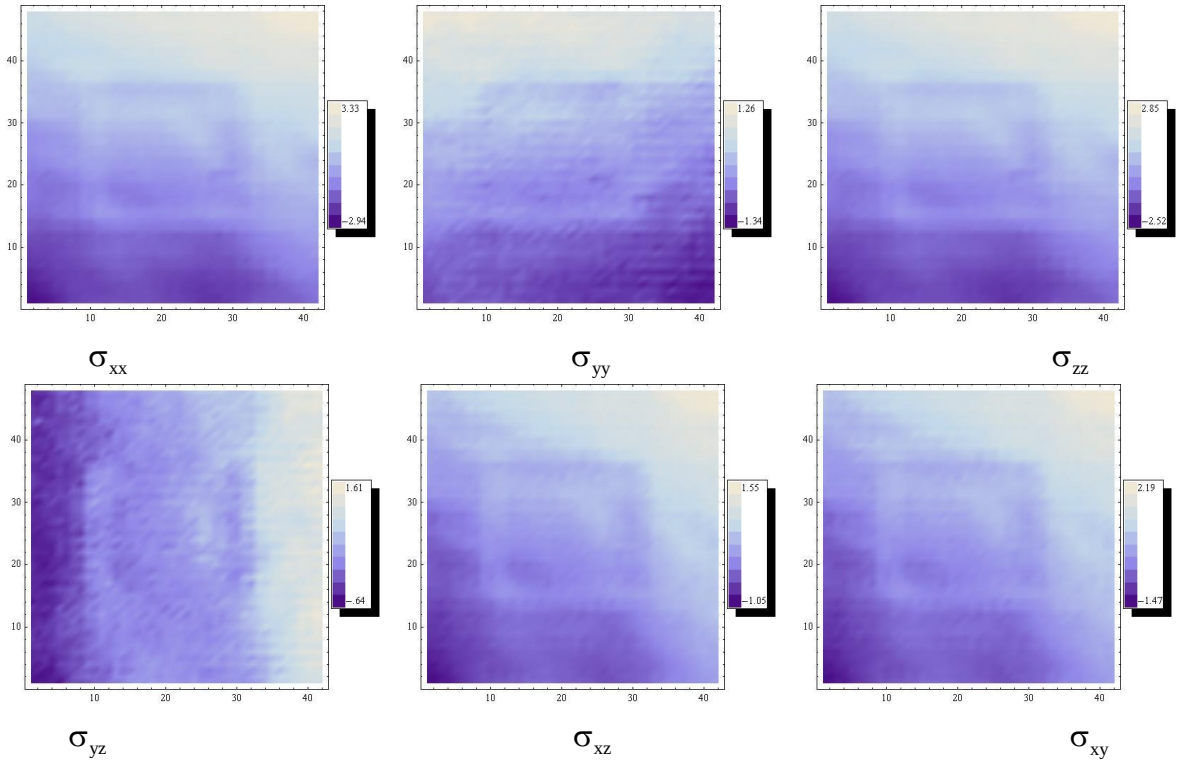

Figure 2-15: Stress maps generated from strain data in transmission geometry

In Figure 2-10 all the six components of residual stress are mapped over the crystal area. Maximum and minimum value (variation) of stress is given in Table 2-2 below.

Table 2-2: Maximum and minimum value (variation) of stress (in GPa)

	σ_{xx}	σ_{yy}	σ_{zz}	σ_{yz}	σ_{xz}	σ_{xy}
Minimum	-2.94	-1.34	-2.52	-.64	-1.05	-1.47
Maximum	3.33	1.26	2.85	1.61	1.55	2.19

A 3-D maps of strain and stress components are also plotted is given in Figure 2-16 and Figure 2-17 respectively. These types of maps are helpful in quickly spotting the high stress region in the crystal and its magnitude.

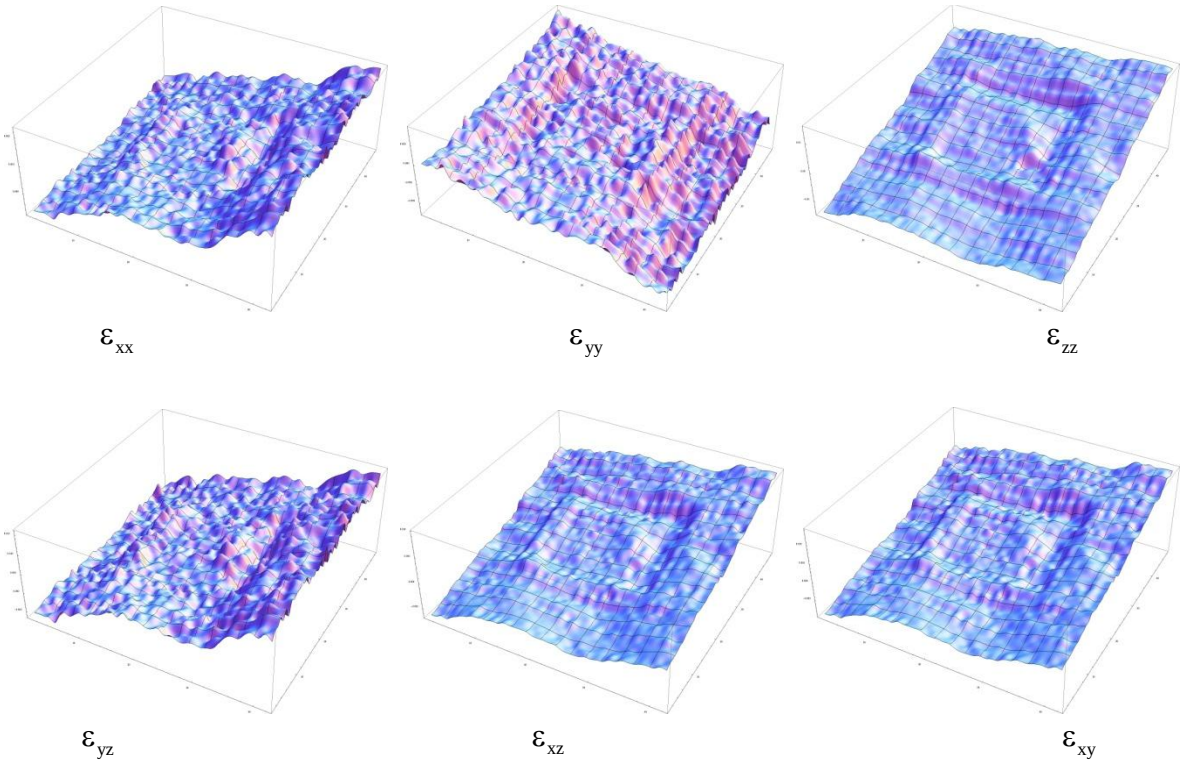

Figure 2.16: 3D Strain map

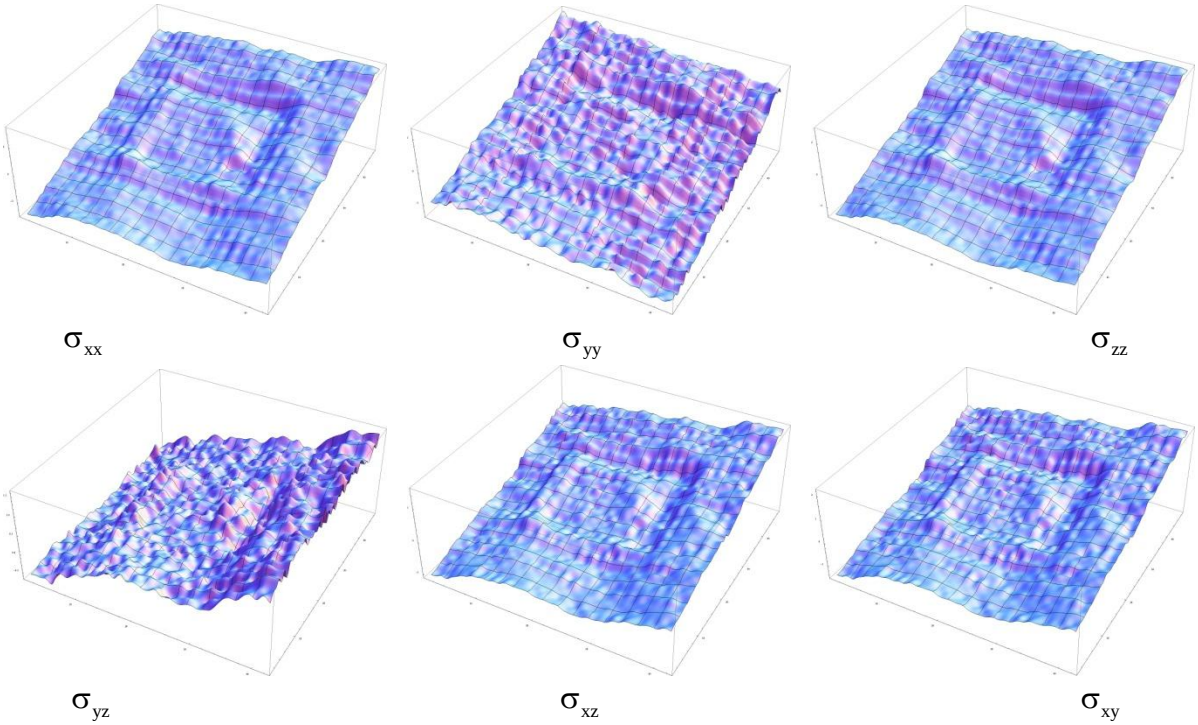

Figure 2-16: 3D Stress plot

Strain and stress variation across any length of crystal can also be easily plotted from the data generated. As an example 2-D graphs given in Figure 2-17 and 2-18 are plotted in order to show stress and strain components variation across x-axis of the crystal at constant y (=20). The Mathematica command used for plotting these 2D and 3D plots are listed in Appendix F.

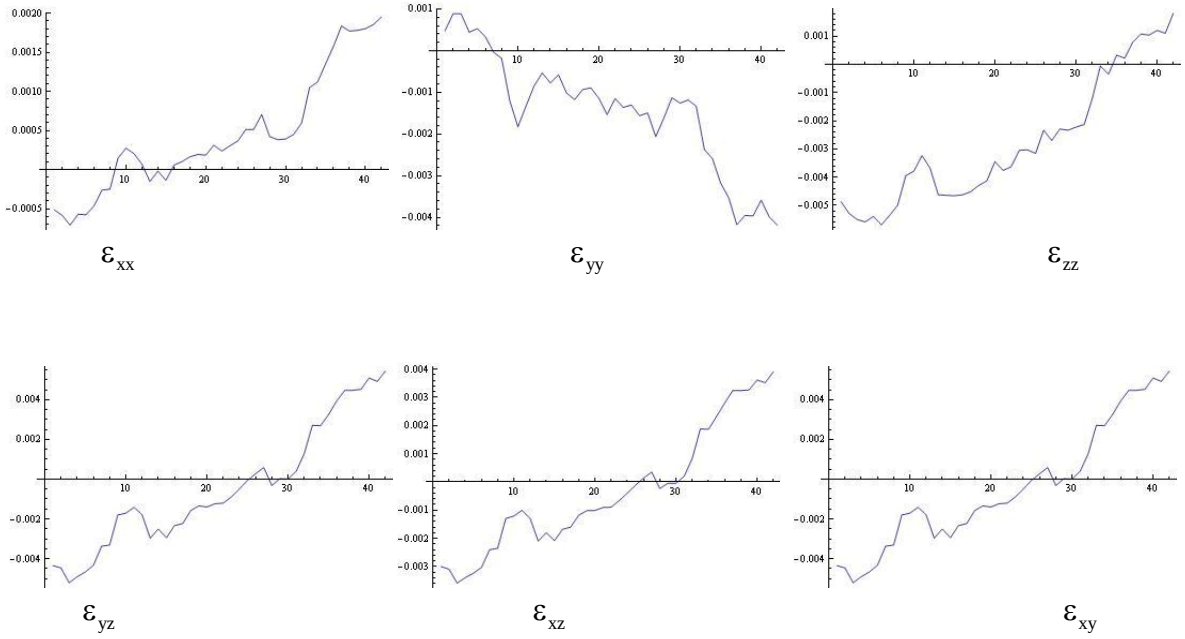

Figure 2-17: Variation of strain as a function of x at constant y (=20).

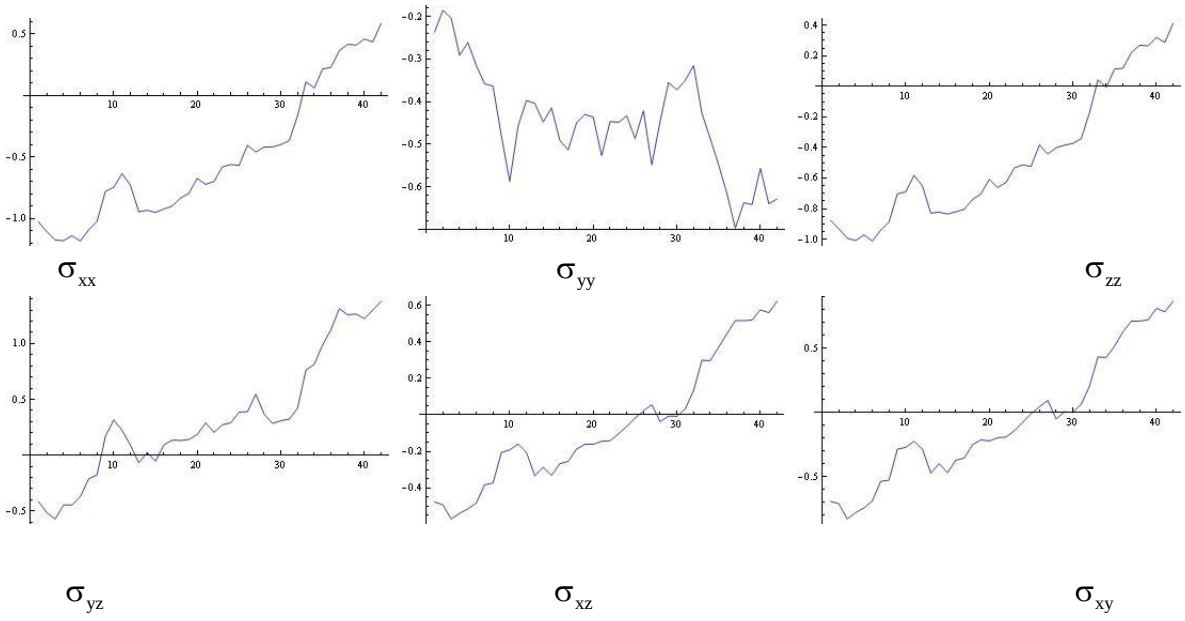

Figure 2-18: Variation of stress as a function of x at constant y (=20).

2.5 Identification and characterization of sources of error

In this section we will analyze various sources of error in the SMART technique. Both experimental and geometrical factors affect the stress values calculated using the SMART technique. Two kinds of errors, random error and systematic error, occur in any experimental measurement. Random errors are those errors which can be revealed by repetition of measurement; those which cannot be revealed are systematic error. The concept of precision is related to random error. Minimizing the random error in measurement increases the precision of the result whereby increasing the repeatability and reproducibility (R and R)[1]. The concept of accuracy is related to systematic error. Systematic error is the bias in the experimental system which pushes the results in the same direction. If identified, this kind of error can be eliminated most of the time. It is also been argued that the in our analysis and interpretation, random error are more of a concern than systematic error. Here we will analyze both the components of error and suggested ways to eliminate or minimize them.

Choice of three crystallographic planes:

Three reticulographs to be chosen must not have same zone axis. If all the three planes belong to same zone axis then their plane normal will lie on a plane and hence they will not be independent. Therefore three planes $(h_1 \quad k_1 \quad l_1)$, $(h_2 \quad k_2 \quad l_2)$ and $(h_3 \quad k_3 \quad l_3)$ must be chosen such that

$$\begin{vmatrix} h_1 & k_1 & l_1 \\ h_2 & k_2 & l_2 \\ h_3 & k_3 & l_3 \end{vmatrix} \neq 0 \qquad \text{Equation 2-18}$$

Plane normal of all the three chosen plane should be as "perpendicular to each other" as possible, this will reduce the error in calculations. In this section we discuss the error arising from choice of three reticulograph. This error will fall in the category of systematic error. This error is inherent to the system and is fundamental to the technique. This error cannot be

[1] *Repeatability is the closeness of agreement between mutually independent test results obtained with the same method on identical test material in the same laboratory by the same operator using the same equipment within short intervals of time. Reproducibility is the closeness of agreement between test results obtained with the same method on identical test material in different laboratories with different operators using different equipment.*

minimized simply by increasing the precision of the measurement but rather by changing the experimental setup.

Considering three plane normal vectors:

$\bar{n}_1 = h_1\hat{i} + k_1\hat{j} + l_1\hat{k}, \bar{n}_2 = h_2\hat{i} + k_2\hat{j} + l_2\hat{k}$ and $\bar{n}_3 = h_3\hat{i} + k_3\hat{j} + l_3\hat{k}$. Assuming that the plane normal vector $\bar{n}_1$, $\bar{n}_2$ and $\bar{n}_3$ are unit vector. Volume V of the parallelepiped defined by the three vectors $\bar{n}_1$, $\bar{n}_2$ and $\bar{n}_3$ is

$$V = \bar{n}_1 \times \bar{n}_2 \cdot \bar{n}_3 \qquad \text{Equation 2-19}$$

This volume is zero (0) when all the three vectors are coplanar. The maximum value of V is 1 when all the three vectors are perpendicular to each other. In order to maximize the precision or reduce the error of calculations, three reticulographs should be chosen in order to maximize V. This is demonstrated below mathematically:

Consider equations 2-11A, 2-11D and 2-11G

$$n_{1x} = n^0_{1x} - \left(n^0_{1x}\frac{\partial u_x}{\partial x} + n^0_{1y}\frac{\partial u_y}{\partial x} + n^0_{1z}\frac{\partial u_z}{\partial x} \right)$$
$$n_{2x} = n^0_{2x} - \left(n^0_{2x}\frac{\partial u_x}{\partial x} + n^0_{2y}\frac{\partial u_y}{\partial x} + n^0_{2z}\frac{\partial u_z}{\partial x} \right)$$
$$n_{3x} = n^0_{3x} - \left(n^0_{3x}\frac{\partial u_x}{\partial x} + n^0_{3y}\frac{\partial u_y}{\partial x} + n^0_{3z}\frac{\partial u_z}{\partial x} \right)$$

Rearranging we get

$$\left(n^0_{1x}\frac{\partial u_x}{\partial x} + n^0_{1y}\frac{\partial u_y}{\partial x} + n^0_{1z}\frac{\partial u_z}{\partial x} \right) = n^0_{1x} - n_{1x}$$
$$\left(n^0_{2x}\frac{\partial u_x}{\partial x} + n^0_{2y}\frac{\partial u_y}{\partial x} + n^0_{2z}\frac{\partial u_z}{\partial x} \right) = n^0_{2x} - n_{2x}$$
$$\left(n^0_{3x}\frac{\partial u_x}{\partial x} + n^0_{3y}\frac{\partial u_y}{\partial x} + n^0_{3z}\frac{\partial u_z}{\partial x} \right) = n^0_{3x} - n_{3x}$$

Solution to these equations will be:

$$\frac{\partial u_x}{\partial x}=\frac{\begin{vmatrix} n^0_{1x}-n_{1x} & n^0_{1y} & n^0_{1z} \\ n^0_{2x}-n_{2x} & n^0_{2y} & n^0_{2z} \\ n^0_{3x}-n_{3x} & n^0_{3y} & n^0_{3z} \end{vmatrix}}{\begin{vmatrix} n^0_{1x} & n^0_{1y} & n^0_{1z} \\ n^0_{2x} & n^0_{2y} & n^0_{2z} \\ n^0_{3x} & n^0_{3y} & n^0_{3z} \end{vmatrix}}, \frac{\partial u_y}{\partial x}=\frac{\begin{vmatrix} n^0_{1x} & n^0_{1x}-n_{1x} & n^0_{1z} \\ n^0_{2x} & n^0_{2x}-n_{2x} & n^0_{2z} \\ n^0_{3x} & n^0_{3x}-n_{3x} & n^0_{3z} \end{vmatrix}}{\begin{vmatrix} n^0_{1x} & n^0_{1y} & n^0_{1z} \\ n^0_{2x} & n^0_{2y} & n^0_{2z} \\ n^0_{3x} & n^0_{3y} & n^0_{3z} \end{vmatrix}}, \frac{\partial u_z}{\partial x}=\frac{\begin{vmatrix} n^0_{1x} & n^0_{1y} & n^0_{1x}-n_{1x} \\ n^0_{2x} & n^0_{2y} & n^0_{2x}-n_{2x} \\ n^0_{3x} & n^0_{3y} & n^0_{3x}-n_{3x} \end{vmatrix}}{\begin{vmatrix} n^0_{1x} & n^0_{1y} & n^0_{1z} \\ n^0_{2x} & n^0_{2y} & n^0_{2z} \\ n^0_{3x} & n^0_{3y} & n^0_{3z} \end{vmatrix}}$$

Equation 2-20 A, B, C

Similarly solving equation 2-11B, 2-11E and 2-11H we get:

$$\frac{\partial u_x}{\partial y}=\frac{\begin{vmatrix} n^0_{1y}-n_{1y} & n^0_{1y} & n^0_{1z} \\ n^0_{2y}-n_{2y} & n^0_{2y} & n^0_{2z} \\ n^0_{3y}-n_{3y} & n^0_{3y} & n^0_{3z} \end{vmatrix}}{\begin{vmatrix} n^0_{1x} & n^0_{1y} & n^0_{1z} \\ n^0_{2x} & n^0_{2y} & n^0_{2z} \\ n^0_{3x} & n^0_{3y} & n^0_{3z} \end{vmatrix}}, \frac{\partial u_y}{\partial y}=\frac{\begin{vmatrix} n^0_{1x} & n^0_{1y}-n_{1y} & n^0_{1z} \\ n^0_{2x} & n^0_{2y}-n_{2y} & n^0_{2z} \\ n^0_{3x} & n^0_{3y}-n_{3y} & n^0_{3z} \end{vmatrix}}{\begin{vmatrix} n^0_{1x} & n^0_{1y} & n^0_{1z} \\ n^0_{2x} & n^0_{2y} & n^0_{2z} \\ n^0_{3x} & n^0_{3y} & n^0_{3z} \end{vmatrix}}, \frac{\partial u_z}{\partial y}=\frac{\begin{vmatrix} n^0_{1x} & n^0_{1y} & n^0_{1y}-n_{1y} \\ n^0_{2x} & n^0_{2y} & n^0_{2y}-n_{2y} \\ n^0_{3x} & n^0_{3y} & n^0_{3y}-n_{3y} \end{vmatrix}}{\begin{vmatrix} n^0_{1x} & n^0_{1y} & n^0_{1z} \\ n^0_{2x} & n^0_{2y} & n^0_{2z} \\ n^0_{3x} & n^0_{3y} & n^0_{3z} \end{vmatrix}}$$

Equation 2-20 D, E, F

Solving equation 2-11C, 2-11F and 2-11I we get:

$$\frac{\partial u_x}{\partial z}=\frac{\begin{vmatrix} n^0_{1z}-n_{1z} & n^0_{1y} & n^0_{1z} \\ n^0_{2z}-n_{2z} & n^0_{2y} & n^0_{2z} \\ n^0_{3z}-n_{3z} & n^0_{3y} & n^0_{3z} \end{vmatrix}}{\begin{vmatrix} n^0_{1x} & n^0_{1y} & n^0_{1z} \\ n^0_{2x} & n^0_{2y} & n^0_{2z} \\ n^0_{3x} & n^0_{3y} & n^0_{3z} \end{vmatrix}}, \frac{\partial u_y}{\partial z}=\frac{\begin{vmatrix} n^0_{1x} & n^0_{1z}-n_{1z} & n^0_{1z} \\ n^0_{2x} & n^0_{2z}-n_{2z} & n^0_{2z} \\ n^0_{3x} & n^0_{3z}-n_{3z} & n^0_{3z} \end{vmatrix}}{\begin{vmatrix} n^0_{1x} & n^0_{1y} & n^0_{1z} \\ n^0_{2x} & n^0_{2y} & n^0_{2z} \\ n^0_{3x} & n^0_{3y} & n^0_{3z} \end{vmatrix}}, \frac{\partial u_z}{\partial z}=\frac{\begin{vmatrix} n^0_{1x} & n^0_{1y} & n^0_{1z}-n_{1z} \\ n^0_{2x} & n^0_{2y} & n^0_{2z}-n_{2z} \\ n^0_{3x} & n^0_{3y} & n^0_{3z}-n_{3z} \end{vmatrix}}{\begin{vmatrix} n^0_{1x} & n^0_{1y} & n^0_{1z} \\ n^0_{2x} & n^0_{2y} & n^0_{2z} \\ n^0_{3x} & n^0_{3y} & n^0_{3z} \end{vmatrix}}$$

Equation 2-20 G, H, I

In all nine (9) of the displacement derivative terms $\frac{\partial u_i}{\partial j}$, denominator is constant V volume defined by the three unit plane normal vector. In order to minimize the error or maximize the accuracy of the calculations, V should be maximized. Therefore ideally one should chose

three plane normal perpendicular to each other. Practically it may not be possible to simultaneously record three reticulograph such that their plane normal vectors are perpendicular to each other. In the section 2-6, it is proved mathematically that the results (strain or stress values) are independent of choice of reticulographs but the precession or the accuracy of measurement depend on the choice of the reticulographs or the diffracting planes.

Error in the values of strain and stress arising due to experimental measurements, random error is discussed next. Main sources of experimental error come from the measurement of specimen to film distance and the measurement of coordinate points on the reticulograph. These errors are possible to minimize using precise experimental setup and sophisticated detector. However these errors may not be completely eliminated.

Some other minor source of error such as warpage of film due to uneven film holder can be analyzed as error in the coordinate point measurement. Because, slight tilt and twist of the film will result in slight deviation of array points.

Error due to specimen to film distance: Specimen to film distance is measured using a ruler in the beamline prior to the exposure. After processing the X-ray film, it is compared with the simulated Laue pattern program [ref] and more precise specimen to film distance (sfd) value is determined. It is estimated that the precision with which sfd measurement can be determined is about 1mm. A schematic representation of the error introduced due to inaccuracy in film position is shown in Figure 2-19.

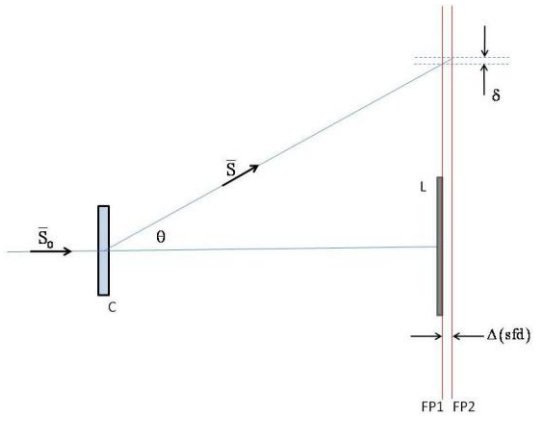

Figure 2-19: Schematic of experimental setup showing the error introduced in the calculations due to error in measurement in specimen to film distance. C, L, FP1 and FP2 represents crystal sample, Lead beam-stop, film position 1 and film position 2 respectively.

Two positions of film, film position 1 (FP1) and film position 2 (FP2) are separated by a small distance $\Delta(\text{sfd})$. Assuming that the diffracted beam is at an angle θ, with respect to incident beam. It can be shown that:

$\delta = tan(\theta)\Delta(\text{sfd})$ Equation 2-21

Similarly for stress free location:

$\delta_0 = tan(\theta_0)\Delta(\text{sfd})$ Equation 2-22

Displacement in the diffracted beam position on the film caused by variation of sfd is in same direction for all locations in the crystal including stress free location. Therefore the net error is the difference between the displacement at a stressed location and stress free location.

Net error in displacement = $\delta - \delta_0 = tan(\theta)\Delta(\text{sfd}) - tan(\theta_0)\Delta(\text{sfd})$

or, $\delta - \delta_0 = \left[tan(\theta) - tan(\theta_0)\right]\Delta(\text{sfd})$ Equation 2-23

In order to estimate the error in stress due to variation in specimen to film distance we first estimate the maximum limit of $(\delta - \delta_0)$.

Assuming 422 reticulograph, $\theta_0 = 47^0$, $\theta = 47.01^0$, $\Delta(\text{sfd}) = 1\text{mm}$ we get $(\delta - \delta_0) = \mathbf{.35}\mu\text{m}$

Since the resolution of X-ray film is about 2μm, therefore the error due to specimen to film distance is not detectable with our current detection system.

Error due to determination of coordinate points: Coordinate points are determined on a TIFF format image using image recognition software [Appendix G]. This software determines the coordinate points of the grid-corner by analyzing the change in contrast in the image. The possible error is due to the resolution of the X-ray film and the blurring in the film image itself. It is estimated that the maximum error in determining the coordinate point on the film is about 2μm. This error in displacement on the film will contribute to the error in the plane normal direction. Error in plane normal vector direction will result in error in the displacement derivative components $\left[u_{ij}\right]$ or $\left[\frac{\partial u_i}{\partial j}\right]$. Uncertainty or error in displacement-derivative

components will in turn lead to uncertainty in strain components. Error in strain will cause error in stress components. A schematic 2D diagram shown in Figure 2-21 indicates the variation in plane normal caused by uncertainty in the coordinate position in the reticulograph.

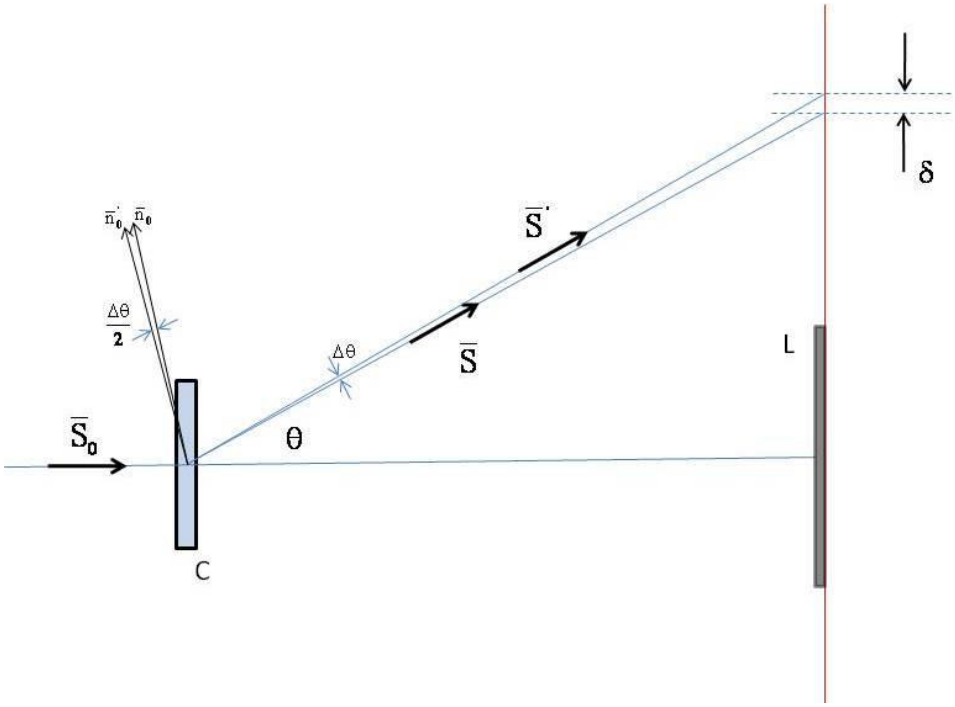

Figure 2-20: Schematic representation of error introduced in the plane normal vector due to variation in coordinate position in the reticulograph. δ is the error in diffracted beam position in the reticulograph. $\delta\theta$ change in diffracted beam angle leads to $\frac{\delta\theta}{2}$ angular rotation in plane normal vector.

Assuming δ is the error of measurement in the X-ray film. This implies that the error generated in finding the coordinate points will translate into error in determining diffraction direction which in turn will create error in plane normal direction. It can be shown that variation in diffracted beam angle $(\Delta\theta)$ will cause $\left(\frac{\Delta\theta}{2}\right)$ variation in plane normal vector. It can also be shown that the error in the angle $(\Delta\theta)$ is related to error in coordinate point measurement δ by the Equation 2-24:

$$(\Delta\theta) = \frac{\delta}{\text{sfd}} \qquad \text{Equation 2-24}$$

This is schematically shown in Figure 2-20.

First we determine analytical expression of displacement-derivative terms. We start with the expression of $\frac{\partial u_x}{\partial x}$ (Equation 2-19 a).

$$\frac{\partial u_x}{\partial x} = \frac{\begin{vmatrix} n^0_{1x} - n_{1x} & n^0_{1y} & n^0_{1z} \\ n^0_{2x} - n_{2x} & n^0_{2y} & n^0_{2z} \\ n^0_{3x} - n_{3x} & n^0_{3y} & n^0_{3z} \end{vmatrix}}{\begin{vmatrix} n^0_{1x} & n^0_{1y} & n^0_{1z} \\ n^0_{2x} & n^0_{2y} & n^0_{2z} \\ n^0_{3x} & n^0_{3y} & n^0_{3z} \end{vmatrix}}$$

Expanding the numerator and assigning the denominator as V, we get:

$$\frac{\partial u_x}{\partial x} = \frac{1}{V}\left[\left(n^0_{1x} - n_{1x}\right)\left(n^0_{2y}n^0_{3z} - n^0_{2z}n^0_{3y}\right) - n^0_{1y}\left(n^0_{3y}n^0_{2x} - n^0_{3y}n_{2x} - n^0_{2z}n^0_{3x} + n^0_{2z}n_{3x}\right) + n^0_{1z}\left(n^0_{3y}n^0_{2x} - n^0_{3y}n_{2x} - n^0_{2y}n^0_{3x} + n^0_{2y}n_{3x}\right)\right]$$

Equation 2-25

Therefore,

$$\Delta\left(\frac{\partial u_x}{\partial x}\right) = \frac{1}{V}\left[-\Delta n_{1x}\left(n^0_{2y}n^0_{3z} - n^0_{2z}n^0_{3y}\right) - n^0_{1y}\left(n^0_{3y}\Delta n_{2x} - n^0_{2z}\Delta n_{3x}\right) + n^0_{1z}\left(-n^0_{3y}\Delta n_{2x} + n^0_{2y}\Delta n_{3x}\right)\right]$$

After rearranging:

$$\Delta\left(\frac{\partial u_x}{\partial x}\right) = \frac{1}{V}\left[\Delta n_{1x}\left(n^0_{2z}n^0_{3y} - n^0_{2y}n^0_{3z}\right) - \Delta n_{2x}\left(n^0_{1z}n^0_{3y} - n^0_{1y}n^0_{3y}\right) + \Delta n_{3x}\left(n^0_{1z}n^0_{2y} - n^0_{1y}n^0_{2z}\right)\right]$$

Simplifying further we can write the right hand side in the determinant format:

$$\Delta\left(\frac{\partial u_x}{\partial x}\right) = \frac{1}{V}\begin{vmatrix} \Delta n_{1x} & \Delta n_{2x} & \Delta n_{3x} \\ n^0_{1z} & n^0_{2z} & n^0_{3y} \\ n^0_{1y} & n^0_{2y} & n^0_{3y} \end{vmatrix}$$

Similar expression can be written for all the nine components:

$$\Delta\left(\frac{\partial u_x}{\partial x}\right)=\frac{1}{V}\begin{vmatrix}\Delta n_{1x} & \Delta n_{2x} & \Delta n_{3x}\\ n^0_{1z} & n^0_{2z} & n^0_{3y}\\ n^0_{1y} & n^0_{2y} & n^0_{3y}\end{vmatrix};\Delta\left(\frac{\partial u_y}{\partial x}\right)=\frac{1}{V}\begin{vmatrix}\Delta n_{1x} & \Delta n_{2x} & \Delta n_{3x}\\ n^0_{1x} & n^0_{2x} & n^0_{3x}\\ n^0_{1z} & n^0_{2z} & n^0_{3z}\end{vmatrix};\Delta\left(\frac{\partial u_z}{\partial x}\right)=\frac{1}{V}\begin{vmatrix}\Delta n_{1x} & \Delta n_{2x} & \Delta n_{3x}\\ n^0_{1y} & n^0_{2y} & n^0_{3y}\\ n^0_{1x} & n^0_{2x} & n^0_{3x}\end{vmatrix}$$

$$\Delta\left(\frac{\partial u_x}{\partial y}\right)=\frac{1}{V}\begin{vmatrix}\Delta n_{1y} & \Delta n_{2y} & \Delta n_{3y}\\ n^0_{1z} & n^0_{2z} & n^0_{3y}\\ n^0_{1y} & n^0_{2y} & n^0_{3y}\end{vmatrix};\Delta\left(\frac{\partial u_y}{\partial y}\right)=\frac{1}{V}\begin{vmatrix}\Delta n_{1y} & \Delta n_{2y} & \Delta n_{3y}\\ n^0_{1x} & n^0_{2x} & n^0_{3x}\\ n^0_{1z} & n^0_{2z} & n^0_{3z}\end{vmatrix};\Delta\left(\frac{\partial u_z}{\partial y}\right)=\frac{1}{V}\begin{vmatrix}\Delta n_{1y} & \Delta n_{2y} & \Delta n_{3y}\\ n^0_{1y} & n^0_{2y} & n^0_{3y}\\ n^0_{1x} & n^0_{2x} & n^0_{3x}\end{vmatrix}$$

$$\Delta\left(\frac{\partial u_x}{\partial z}\right)=\frac{1}{V}\begin{vmatrix}\Delta n_{1z} & \Delta n_{2z} & \Delta n_{3z}\\ n^0_{1z} & n^0_{2z} & n^0_{3y}\\ n^0_{1y} & n^0_{2y} & n^0_{3y}\end{vmatrix};\Delta\left(\frac{\partial u_y}{\partial z}\right)=\frac{1}{V}\begin{vmatrix}\Delta n_{1z} & \Delta n_{2z} & \Delta n_{3z}\\ n^0_{1x} & n^0_{2x} & n^0_{3x}\\ n^0_{1z} & n^0_{2z} & n^0_{3z}\end{vmatrix};\Delta\left(\frac{\partial u_z}{\partial z}\right)=\frac{1}{V}\begin{vmatrix}\Delta n_{1z} & \Delta n_{2z} & \Delta n_{3z}\\ n^0_{1y} & n^0_{2y} & n^0_{3y}\\ n^0_{1x} & n^0_{2x} & n^0_{3x}\end{vmatrix}$$

Equation 2-26 A, B, C, D, E, F, G, H, I

From the above analytical expressions for error in displacement derivative terms, error in the strain components can be readily calculated.

For normal component $\Delta(\varepsilon_{xx})=\Delta\left(\frac{\partial u_x}{\partial x}\right)$ Equation 2-27

and for sheer component

$$\Delta(\varepsilon_{xy})=\frac{1}{2}\left(\Delta\left(\frac{\partial u_y}{\partial x}\right)+\Delta\left(\frac{\partial u_x}{\partial y}\right)\right)$$ Equation 2-28

Similar equations can be written for other strain components. This error in strain will translate to error in stress, for example:

$$\Delta\sigma_{xx}=C_{11}\Delta\varepsilon_{xx}+C_{12}\Delta\varepsilon_{yy}+C_{13}\Delta\varepsilon_{zz}+2C_{14}\Delta\varepsilon_{xz}+2C_{15}\Delta\varepsilon_{zx}+2C_{16}\Delta\varepsilon_{xy}$$ Equation 2-29

Using the above generalized analytical results we can now estimate the error in the residual stress. This will be the resolution or the minimum amount of absolute residual stress that can be calculated without ambiguity.

Using value of δ as 2μm, resolution of X-ray films used for the experiments we estimate the value of error in stress in Silicon dies to be 10MPa

In most engineering investigation, usually precision is more important than accuracy. Precision is achieved by reducing the random error while accuracy is achieved by increasing the systematic error. It has been pointed out by Norton [61] that the investigator is more interested in precision

than accuracy. Investigator usually wants to know the difference in stress level from one location to another or the change in stress level at a point before and after processing. A large error say 30 percent of the absolute magnitude of measured stress would rarely change the conclusion reached in the investigation.

Error due to shape of crystal: Assuming a rectangular shaped crystal before packaging. After processing at higher temperature and subsequent cooling of the package leads to bending of the packaged assembly as shown in the Figure 2-21.

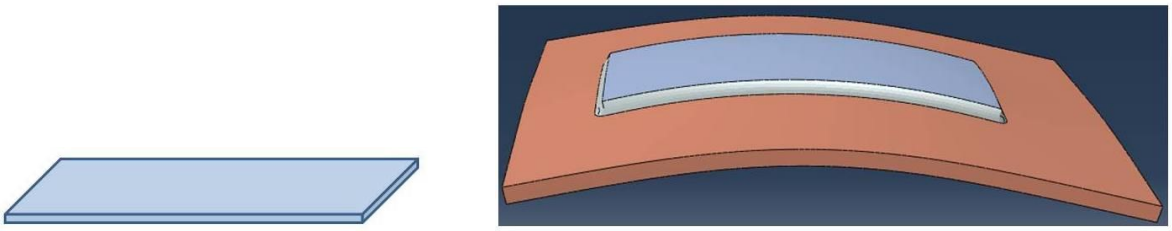

(A) (B)

Figure 2-21: Schematic of a Silicon die (A) before packaging and (B) after packaging

As a result of this bending in-plane normal stress are maximum at the top (tensile) and minimum (compressive) at the bottom. Shape of the crystal itself does not play a role in stress determination using SMART technique. However, bending of crystallographic plane will occur if the crystal changes shape due to bending. The bending of crystallographic planes is incorporated in the smart technique and no special consideration is required for change in shape. In summary a table is generated for various sources of error and the possible error in stress value.

Table 2-3: Maximum value of error resulting from different sources

Source of random error	Maximum error in stress level in Si
Specimen to film distance	2 MPa
Coordinate point determination	10 MPa

2.6 Analytical proof of SMART technique

In this section a proof of the SMART technique is described. Here we have proved that the results obtained (strain and stress values) in this technique are independent of the choice of reticulograph. The fact that any three diffracting planes can be used for calculation is one of the useful results which make the SMART technique a powerful tool.

In order to mathematically validate this technique, it is ***necessary and sufficient*** to prove that same results are obtained by choice of any three *randomly selected* reticulographs.

Let us consider a general experimental setup in transmission geometry in which multiple reticulographs were recorded. First consider the results are obtained by choosing three reticulograph (R1, R2 and R3).

$$\left.\frac{\partial u_x}{\partial x}\right|_{R1,R2,R3} = \frac{\begin{vmatrix} n^0_{1x} - n_{1x} & n^0_{1y} & n^0_{1z} \\ n^0_{2x} - n_{2x} & n^0_{2y} & n^0_{2z} \\ n^0_{3x} - n_{3x} & n^0_{3y} & n^0_{3z} \end{vmatrix}}{\begin{vmatrix} n^0_{1x} & n^0_{1y} & n^0_{1z} \\ n^0_{2x} & n^0_{2y} & n^0_{2z} \\ n^0_{3x} & n^0_{3y} & n^0_{3z} \end{vmatrix}}$$ Equation 2-30 (Result obtained by choosing R1, R2 and R3)

Now if we consider another set of reticulographs (say R1, R2 and R4) then

$$\left.\frac{\partial u_x}{\partial x}\right|_{R1,R2,R4} = \frac{\begin{vmatrix} n^0_{1x} - n_{1x} & n^0_{1y} & n^0_{1z} \\ n^0_{2x} - n_{2x} & n^0_{2y} & n^0_{2z} \\ n^0_{4x} - n_{4x} & n^0_{4y} & n^0_{4z} \end{vmatrix}}{\begin{vmatrix} n^0_{1x} & n^0_{1y} & n^0_{1z} \\ n^0_{2x} & n^0_{2y} & n^0_{2z} \\ n^0_{4x} & n^0_{4y} & n^0_{4z} \end{vmatrix}}$$ Equation 2-31 (Result obtained by choosing R1, R2 and R4)

Now we are only required to prove $\left.\frac{\partial u_x}{\partial x}\right|_{R1,R2,R3} = \left.\frac{\partial u_x}{\partial x}\right|_{R1,R2,R4}$

Since all the four plane normal are not parallel to each other, fourth vector can be written as a combination of other three.

i.e. $\bar{n}_4 = \alpha\bar{n}_1 + \beta\bar{n}_2 + \gamma\bar{n}_3$ Equation 2-32

In the above equation the constants α, β and γ can be chosen such that $\bar{n}_4$ is a unit vector. Change in plane normal before and after distortion can be written as:

$\bar{n}_1^0 \rightarrow \bar{n}_1$

$\bar{n}_2^0 \rightarrow \bar{n}_2$

$\bar{n}_3^0 \rightarrow \bar{n}_3$

Combining these three equations after multiplying with appropriate constants we get:

$\alpha\bar{n}_1^0 + \beta\bar{n}_2^0 + \gamma\bar{n}_3^0 \rightarrow \alpha\bar{n}_1 + \beta\bar{n}_2 + \gamma\bar{n}_3$
or, $\bar{n}_4^0 \rightarrow \bar{n}_4$ where
$\bar{n}_4^0 = \alpha\bar{n}_1^0 + \beta\bar{n}_2^0 + \gamma\bar{n}_3^0$ Equation 2-33
$\bar{n}_4 = \alpha\bar{n}_1 + \beta\bar{n}_2 + \gamma\bar{n}_3$

Separating x, y and z components:

$$\bar{n}_{4x}^0 = \alpha\bar{n}_{1x}^0 + \beta\bar{n}_{2x}^0 + \gamma\bar{n}_{3x}^0;\ \bar{n}_{4y}^0 = \alpha\bar{n}_{1y}^0 + \beta\bar{n}_{2y}^0 + \gamma\bar{n}_{3y}^0;\ \bar{n}_{4z}^0 = \alpha\bar{n}_{1z}^0 + \beta\bar{n}_{2z}^0 + \gamma\bar{n}_{3z}^0$$
$$\bar{n}_{4x} = \alpha\bar{n}_{1x} + \beta\bar{n}_{2x} + \gamma\bar{n}_{3x};\ \bar{n}_{4y} = \alpha\bar{n}_{1y} + \beta\bar{n}_{2y} + \gamma\bar{n}_{3y};\ \bar{n}_{4z} = \alpha\bar{n}_{1z} + \beta\bar{n}_{2z} + \gamma\bar{n}_{3z}$$

Starting with RHS of Equation 2-31: $\left.\frac{\partial u_x}{\partial x}\right|_{R1,R2,R4} = \frac{\begin{vmatrix} n_{1x}^0 - n_{1x} & n_{1y}^0 & n_{1z}^0 \\ n_{2x}^0 - n_{2x} & n_{2y}^0 & n_{2z}^0 \\ n_{4x}^0 - n_{4x} & n_{4y}^0 & n_{4z}^0 \end{vmatrix}}{\begin{vmatrix} n_{1x}^0 & n_{1y}^0 & n_{1z}^0 \\ n_{2x}^0 & n_{2y}^0 & n_{2z}^0 \\ n_{4x}^0 & n_{4y}^0 & n_{4z}^0 \end{vmatrix}} = \frac{N}{D}$

where N and D represents numerator and denominator.

$$D = \begin{vmatrix} n_{1x}^0 & n_{1y}^0 & n_{1z}^0 \\ n_{2x}^0 & n_{2y}^0 & n_{2z}^0 \\ n_{4x}^0 & n_{4y}^0 & n_{4z}^0 \end{vmatrix} = \begin{vmatrix} n_{1x}^0 & n_{1y}^0 & n_{1z}^0 \\ n_{2x}^0 & n_{2y}^0 & n_{2z}^0 \\ \alpha\bar{n}_{1x}^0 + \beta\bar{n}_{2x}^0 + \gamma\bar{n}_{3x}^0 & \alpha\bar{n}_{1y}^0 + \beta\bar{n}_{2y}^0 + \gamma\bar{n}_{3y}^0 & \alpha\bar{n}_{1y}^0 + \beta\bar{n}_{2y}^0 + \gamma\bar{n}_{3y}^0 \end{vmatrix}$$

Performing the determinant operation: $\text{Row}\boldsymbol{3} \to \text{Row}\boldsymbol{3} - \alpha\text{Row}\boldsymbol{1}$

$$D = \begin{vmatrix} n_{1x}^{0} & n_{1y}^{0} & n_{1z}^{0} \\ n_{2x}^{0} & n_{2y}^{0} & n_{2z}^{0} \\ \beta\bar{n}_{2x}^{0} + \gamma\bar{n}_{3x}^{0} & \beta\bar{n}_{2y}^{0} + \gamma\bar{n}_{3y}^{0} & \beta\bar{n}_{2y}^{0} + \gamma\bar{n}_{3y}^{0} \end{vmatrix}$$

Performing the determinant operation: $\text{Row}\boldsymbol{3} \to \text{Row}\boldsymbol{3} - \beta\text{Row}\boldsymbol{1}$

$$D = \begin{vmatrix} n_{1x}^{0} & n_{1y}^{0} & n_{1z}^{0} \\ n_{2x}^{0} & n_{2y}^{0} & n_{2z}^{0} \\ \gamma\bar{n}_{3x}^{0} & \gamma\bar{n}_{3y}^{0} & \gamma\bar{n}_{3y}^{0} \end{vmatrix} = \gamma \begin{vmatrix} n_{1x}^{0} & n_{1y}^{0} & n_{1z}^{0} \\ n_{2x}^{0} & n_{2y}^{0} & n_{2z}^{0} \\ \bar{n}_{3x}^{0} & \bar{n}_{3y}^{0} & \bar{n}_{3y}^{0} \end{vmatrix}$$

Now consider N,

$$N = \begin{vmatrix} n_{1x}^{0} - n_{1x} & n_{1y}^{0} & n_{1z}^{0} \\ n_{2x}^{0} - n_{2x} & n_{2y}^{0} & n_{2z}^{0} \\ n_{4x}^{0} - n_{4x} & n_{4y}^{0} & n_{4z}^{0} \end{vmatrix} = \begin{vmatrix} n_{1x}^{0} - n_{1x} & n_{1y}^{0} & n_{1z}^{0} \\ n_{2x}^{0} - n_{2x} & n_{2y}^{0} & n_{2z}^{0} \\ \alpha\bar{n}_{1x}^{0} + \beta\bar{n}_{2x}^{0} + \gamma\bar{n}_{3x}^{0} - n_{4x} & \alpha\bar{n}_{1y}^{0} + \beta\bar{n}_{2y}^{0} + \gamma\bar{n}_{3y}^{0} & \alpha\bar{n}_{1z}^{0} + \beta\bar{n}_{2z}^{0} + \gamma\bar{n}_{3z}^{0} \end{vmatrix}$$

Performing the determinant operation: $\text{Row}\boldsymbol{3} \to \text{Row}\boldsymbol{3} - \alpha\text{Row}\boldsymbol{1}$

$$N = \begin{vmatrix} n_{1x}^{0} - n_{1x} & n_{1y}^{0} & n_{1z}^{0} \\ n_{2x}^{0} - n_{2x} & n_{2y}^{0} & n_{2z}^{0} \\ \alpha n_{1x} + \beta\bar{n}_{2x}^{0} + \gamma\bar{n}_{3x}^{0} - n_{4x} & \beta\bar{n}_{2y}^{0} + \gamma\bar{n}_{3y}^{0} & \beta\bar{n}_{2z}^{0} + \gamma\bar{n}_{3z}^{0} \end{vmatrix}$$

Performing the determinant operation: $\text{Row}\boldsymbol{3} \to \text{Row}\boldsymbol{3} - \beta\text{Row}\boldsymbol{1}$

$$N = \begin{vmatrix} n_{1x}^{0} - n_{1x} & n_{1y}^{0} & n_{1z}^{0} \\ n_{2x}^{0} - n_{2x} & n_{2y}^{0} & n_{2z}^{0} \\ \alpha n_{1x} + \beta n_{2x} + \gamma\bar{n}_{3x}^{0} - n_{4x} & \gamma\bar{n}_{3y}^{0} & \gamma\bar{n}_{3z}^{0} \end{vmatrix}$$

Substituting $\bar{n}_{4x} = \alpha\bar{n}_{1x} + \beta\bar{n}_{2x} + \gamma\bar{n}_{3x}$

$$N = \begin{vmatrix} n^0_{1x} - n_{1x} & n^0_{1y} & n^0_{1z} \\ n^0_{2x} - n_{2x} & n^0_{2y} & n^0_{2z} \\ \gamma\bar{n}^0_{3x} - \gamma\bar{n}^0_{3x} & \gamma\bar{n}^0_{3y} & \gamma\bar{n}^0_{3z} \end{vmatrix} = \gamma \begin{vmatrix} n^0_{1x} - n_{1x} & n^0_{1y} & n^0_{1z} \\ n^0_{2x} - n_{2x} & n^0_{2y} & n^0_{2z} \\ \bar{n}^0_{3x} - \bar{n}^0_{3x} & \bar{n}^0_{3y} & \bar{n}^0_{3z} \end{vmatrix}$$

Substituting expressions for N and D we get:

$$\left.\frac{\partial u_x}{\partial x}\right|_{R1,R2,R4} = \frac{N}{D} = \frac{\gamma \begin{vmatrix} n^0_{1x} - n_{1x} & n^0_{1y} & n^0_{1z} \\ n^0_{2x} - n_{2x} & n^0_{2y} & n^0_{2z} \\ \bar{n}^0_{3x} - \bar{n}^0_{3x} & \bar{n}^0_{3y} & \bar{n}^0_{3z} \end{vmatrix}}{\gamma \begin{vmatrix} n^0_{1x} & n^0_{1y} & n^0_{1z} \\ n^0_{2x} & n^0_{2y} & n^0_{2z} \\ \bar{n}^0_{3x} & \bar{n}^0_{3y} & \bar{n}^0_{3y} \end{vmatrix}} = \frac{\begin{vmatrix} n^0_{1x} - n_{1x} & n^0_{1y} & n^0_{1z} \\ n^0_{2x} - n_{2x} & n^0_{2y} & n^0_{2z} \\ \bar{n}^0_{3x} - \bar{n}^0_{3x} & \bar{n}^0_{3y} & \bar{n}^0_{3z} \end{vmatrix}}{\begin{vmatrix} n^0_{1x} & n^0_{1y} & n^0_{1z} \\ n^0_{2x} & n^0_{2y} & n^0_{2z} \\ \bar{n}^0_{3x} & \bar{n}^0_{3y} & \bar{n}^0_{3y} \end{vmatrix}} = \left.\frac{\partial u_x}{\partial x}\right|_{R1,R2,R3}$$

Similarly other displacement-derivative terms can be proved.

Without the loss of generality, using the above result we can say that:

$$\left.\frac{\partial u_x}{\partial x}\right|_{R1,R2,R4} = \left.\frac{\partial u_x}{\partial x}\right|_{R2,R4,R5} = \left.\frac{\partial u_x}{\partial x}\right|_{R4,R5,R6}$$

Therefore

$\left.\frac{\partial u_x}{\partial x}\right|_{R1,R2,R3} = \left.\frac{\partial u_x}{\partial x}\right|_{R4,R5,R6}$ and by similar argument, equivalency of rest of the components can be demonstrated, i.e.

$$\left.\frac{\partial u_x}{\partial x}\right|_{R1,R2,R3} = \left.\frac{\partial u_x}{\partial x}\right|_{R4,R5,R6}; \quad \left.\frac{\partial u_y}{\partial x}\right|_{R1,R2,R3} = \left.\frac{\partial u_y}{\partial x}\right|_{R4,R5,R6}; \quad \left.\frac{\partial u_z}{\partial x}\right|_{R1,R2,R3} = \left.\frac{\partial u_z}{\partial x}\right|_{R4,R5,R6}$$
$$\left.\frac{\partial u_x}{\partial y}\right|_{R1,R2,R3} = \left.\frac{\partial u_x}{\partial y}\right|_{R4,R5,R6}; \quad \left.\frac{\partial u_y}{\partial y}\right|_{R1,R2,R3} = \left.\frac{\partial u_y}{\partial y}\right|_{R4,R5,R6}; \quad \left.\frac{\partial u_z}{\partial y}\right|_{R1,R2,R3} = \left.\frac{\partial u_z}{\partial y}\right|_{R4,R5,R6}$$
$$\left.\frac{\partial u_x}{\partial z}\right|_{R1,R2,R3} = \left.\frac{\partial u_x}{\partial z}\right|_{R4,R5,R6}; \quad \left.\frac{\partial u_y}{\partial z}\right|_{R1,R2,R3} = \left.\frac{\partial u_y}{\partial z}\right|_{R4,R5,R6}; \quad \left.\frac{\partial u_z}{\partial z}\right|_{R1,R2,R3} = \left.\frac{\partial u_z}{\partial z}\right|_{R4,R5,R6}$$

Therefore strain or the stress results are independent of any three randomly chosen reticulographs.

2.7 Conclusion

A new technique is developed for determination of residual stress tensor at any point in a single crystal. This technique Stress Mapping Analysis via Ray Tracing (SMART) is based on the X-ray diffraction and ray tracing method. This method is applied successfully using synchrotron radiation because of its unique properties such as high intensity, low divergence and natural collimation. Residual stress maps are generated over the crystal area. Synchrotron white beam reticulography is used and Laue pattern is recorded on the X-ray film. Applying basic geometrical analysis and mathematical calculations analytical expression for residual strain is determined. Further applying fundamentals of solid mechanics and Hook's law in tensor form, residual stress is determined. Transmission X-ray geometry is used in carrying out synchrotron experiments, calculated stress values represents average stress in the thickness of the material. This technique has various advantages over other available residual stress measurement techniques. The technique described in this chapter determines all the six tensor components of strain and stress in a non-invasive and non-destructive method. A computer program is written which calculates the strain and stress components at an array of points on the crystal and generates stress and strain maps. Even though calculations are relatively simple and mathematically not complicated the huge amount of data points in the system makes it necessary to use a computer program. Various sources of error are documented and an estimation of error in residual stress calculation is determined. Mathematical proof of SMART technique is also presented which validates our technique. This technique has been applied to various other single crystal materials such as SiC and Sapphire.

Chapter 3 Residual stress mapping and depth profiling in packaged silicon integrated circuit using white beam synchrotron x-ray diffraction topography

3.1 Introduction

In the previous chapter we have determined the residual stress in transmission geometry using SMART technique. The results obtained were the average value of stress level through the thickness of the crystal. This result provides information about the spatial stress distribution in the crystal which is average over the thickness of the crystal. It did not provide stress value at a particular depth inside the crystal, or the stress level at the surface of the crystal. Sometimes it is useful to estimate the stress level at a particular depth in the crystal. The knowledge of stress level at particular depth is useful in designing the devise for its mechanical and electrical stability and performance. Here we have applied the same principle of SMART and X-ray reticulography in reflection geometry in order to determine stress depth profile of individual stress components as a function of depth. In this method stress tensor at an arbitrary point within the crystal can be determined.

Small angle geometry, also referred as reflection geometry, is used for the reticulographic experiments. Reflection geometry is used in order to limit the interaction of X-ray with the crystal to a particular depth so that the information received from the reticulographic image (stress value) is the result from a particular depth. The amount of material (volume or the depth) with which X-ray interacts, can be controlled by the diffraction geometry. For example, by varying the angle of incident one can control the penetration depth [49]. Other factors such as diffracted beam angle and wavelength also affect penetration depth. In our approach of determining residual stress as a function of depth, we have used the concept of penetration depth. A short review of the concept of penetration depth in X-ray diffraction topography is given in Section 1-8.

Due to absorption, intensity of X-rays reduces exponentially as it penetrates into the crystal. Therefore, in all the X-ray diffraction method used for stress determination, provides the exponentially weighted average (Laplace profile) of strain and stress with respect to penetration depth of the X-rays [62], [63]. Here we have derived the actual stress profile from the weighted

average (Laplace profile) stress profile. The solution of this problem can get quite complicated and requires numerical solution [64]

X-ray reticulographs were recorded in reflection geometry by placing a grid close to the sample and parallel to the sample surface. The purpose of grid is to track the corresponding points in individual reticulograph. A schematic of the experimental setup is shown in Figure 3-1. Typically a range of angle is chosen between 1^0 and 10^0 for recording the reticulographs.

The central idea behind the stress depth profiling is same as in the stress determination in the transmission geometry as described in Chapter 2. The deviation of crystallographic plane normal at a point from its original stress free plane normal is due to strain at that location. Plane normal vector at any arbitrary location in the crystal and at a stress free location is determined using experimental data. Each corner point in a reticulographic image can be traced to the corresponding point in the crystal surface, which in turn can be used in calculating diffraction vector. From the knowledge of incident and diffracted beam vector, the plane normal vector is determined. Plane normal vector direction varies from one point to another point is due to the fact that the active diffraction plane is warped due to residual strain in the crystal.
In reflection geometry, interaction of X-rays with the material depends on the penetration depth. Penetration depth t_p is given by the expression

$$t_p = \frac{1}{\mu(\lambda)\left[\cos ec(\phi_0) + \cos ec(\phi_h)\right]} \qquad \text{Equation 3-1}$$

where

ϕ_0 is the entrance angle that is the angle between the incident beam and the surface

ϕ_h is the exit angle or the angle the diffracted beam makes with the crystal surface

$\mu(\lambda)$ is the mass absorption coefficient which is a function of wavelength λ

For derivation of the above equation refer to Section 1-8.

A plot of mass absorption coefficient of Silicon as a function of wavelength is given in Figure F-1 in Appendix F. An analytical function is determined for mass absorption coefficient as a function of wavelength using curve fitting technique. This function is used for determining mass absorption coefficient at any wavelength.

$$\mu = -0.1508\lambda^6 + 1.3684\lambda^5 - 7.2723\lambda^4 + 50.179\lambda^3 - 6.6116\lambda^2 + 2.775\lambda - 0.0166 \quad \text{Equation 3-2}$$

Where mass absorption coefficient μ is in cm^{-1} and wavelength λ is in Angstrom, within the range of .3A to 2.75A.

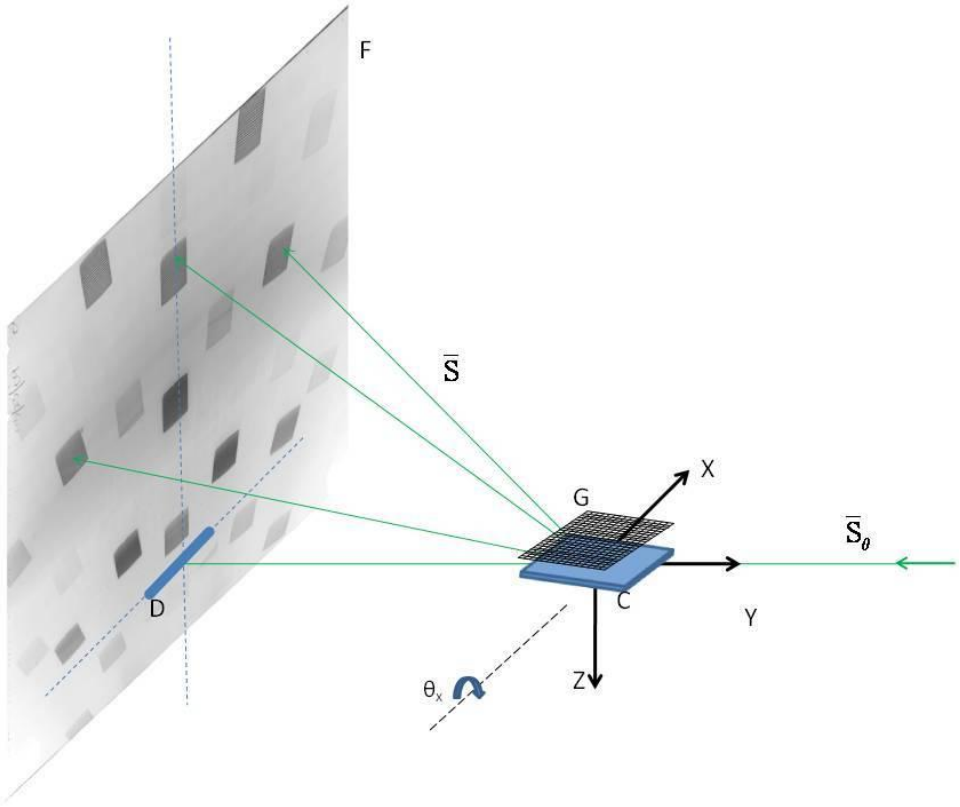

Figure 3-1: Schematic of experimental setup in reflection geometry for recording X-ray reticulograph. Grid is placed parallel and very close to the sample. C, G and F represents crystal, grid and X-ray film respectively. D is the direct beam.

3.2 Penetration depth calculation

Each reticulograph is from a specific crystallographic plane and have different interplaner spacing. Penetration depth of each reticulograph is calculated individually since each reflection has different penetration depth because of different angle of diffraction and different wavelength. In order to determine the penetration depth, we need to determine the exit angle ϕ_h. Let us first consider a general case where crystal surface makes an angle ϕ_0 with respect to incident beam. The measured value of ϕ_0 can further be determined precisely, by comparing the recorded Laue

pattern with the simulated Laue pattern generated by the software LauePt [48]. X-Y coordinate points of the diffraction spot on the film can also be determined from the LauePt program.

a= X coordinate of diffraction spot

b=Y coordinate of diffraction spot

The exit angle ϕ_h can be calculated as:

$$\phi_h = \tan^{-1}\left[\frac{b}{\sqrt{a^2+(sfd)^2}}\right] - \phi_0 \qquad \text{Equation 3-3}$$

The above equation can be readily derived using geometry. A schematic of diffraction in reflection geometry for the purpose of deriving Equation 3-3 is shown in Figure 3-2. All the variables on the right side of equation are known and therefore ϕ_h can be calculated. Wavelength for particular reflection is determined from LauePt [48] program and therefore mass absorption coefficient can be calculated using Equation 3-2.

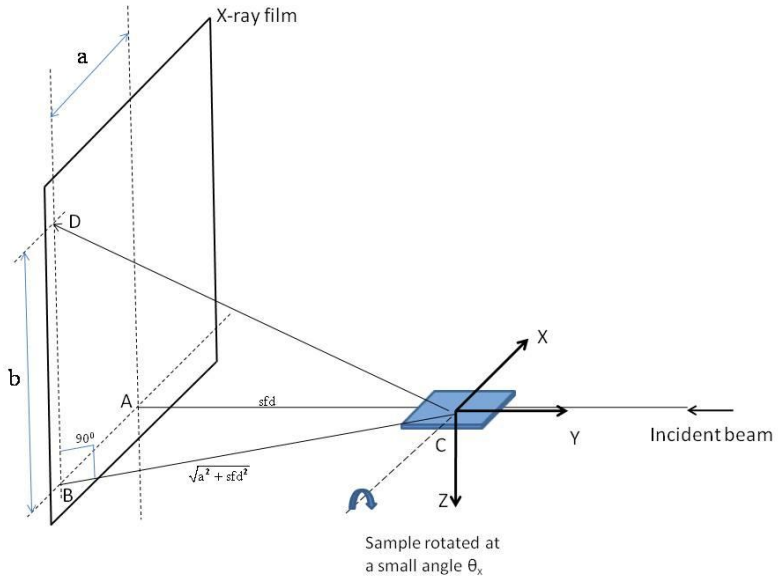

Figure 3-2: Schematic of reflection geometry. Intersection of diffracted beam and the film is point D. Intersection of direct beam and the film is point A. B is the intersection of horizontal and vertical line passing through A and D respectively.

As an example, penetration depth is calculated for the reflection -4 0 -8 when crystal is placed at an angle of $\phi_0 = 5^0$ with respect to incident beam. A screen shot of LauePt program is given in Figure 3-2 and the X-ray film with recorded reticulographs.

Figure 3-3: (A) A screen shot of LauePt program[48] (HKL)=(-1 1 0), (hkl)= (1 1 0), θ_x =5^0. Reflection -4 0 -8, indicated in circle (B) An example of reticulographs recorded in reflection geometry and

In this particular example:

a= -75mm, b= 206mm, sfd= 210mm, $\phi_0 = 5^0$

Therefore $\phi_h = 37.73^0$

Since $\lambda = .48A$, according to Equation 3-2, mass absorption coefficient μ=5.5056cm^{-1}.

Substituting values of $\phi_0, \phi and\ \mu$ into Equation 2-1, we determine penetration depth as

$t_p = 150.9\mu m$

For each reticulographs penetration depth increases continuously with increasing ϕ_0 and reaches a maximum. Figure 3-4 shows the variation of penetration depth with respect to tilt angle of -2 2 -8 reflection in the crystal. Intuitively, penetration depth should increase as the tilt is increased, but this is not the case as it can be seen from Figure 3-4. The reason being, we are

tracking the same reflection as the crystal is tilted, by further tilting the sample Bragg's angle θ increases which implies longer wavelength is required to satisfy the Bragg's law $\lambda=2d\sin\theta$. Longer wavelength (lower the X-ray energy) have higher mass absorption coefficient which results in lower penetration depth at higher tilt angle.

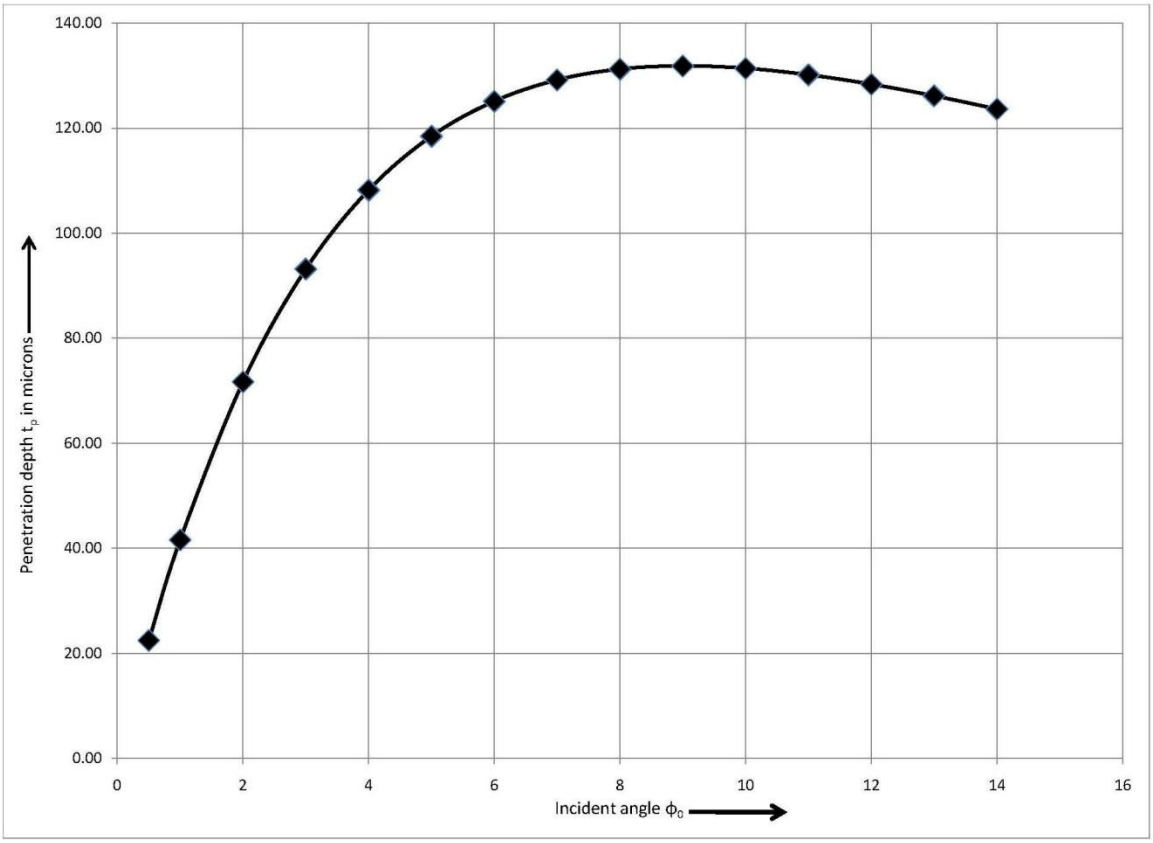

Figure 3-4: Variation of penetration depth of -2 2 -8 reflection as a function of sample rotation θ_x. Note that the penetration depth reaches maximum value of about 140μm.

3.3 Theory and mathematical principle

In determining the stress profile of a crystal, we have used the fundamental concept of SMART technique as previously described in transmission geometry. Point-to-point variation in crystallographic plane normal is measured and this variation forms the basis for strain determination. Using the three chosen reticulographs, residual stress is determined using the SMART technique. This calculated stress value represents a weighted average (exponentially decaying) stress value. This stress value is of very little use and importance than the actual stress

distribution in the real space. The reason that the stress value is weighted average and not a simple average is that the diffraction data has more information from volume which is near the surface rather than further deep into the crystal because X-ray intensity reduces exponentially as it penetrates into the crystal. In general any diffraction technique in the reflection geometry will result in a stress value $\bar{\sigma}(\tau)$ which is Laplace transform of real space stress distribution $\sigma(z)$ given by Equation 3-4 [62-65]:

$$\bar{\sigma}(\tau) = \frac{1}{\tau}\mathcal{L}\left[\sigma(z), \frac{1}{\tau}\right] = \frac{1}{\tau}\int_0^{\infty} \sigma(z) e^{-\frac{z}{\tau}} dz \qquad \text{Equation 3-4}$$

where

τ is the penetration depth

$\bar{\sigma}(\tau)$ is the Laplace transform of real-space stress profile which is equivalent to experimentally determined stress value by diffraction experiment

$\sigma(z)$ is the real-space stress function or profile

z =depth from the crystal surface

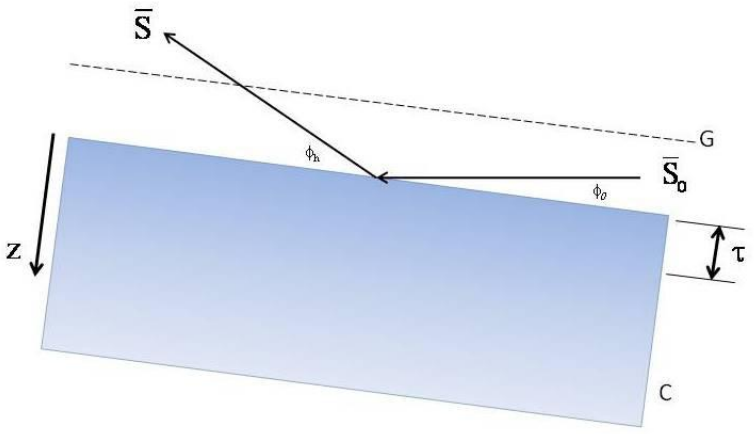

Figure 3-5: Schematic of reflection geometry. z is the coordinate axis going into the crystal, z=0 at the surface of crystal. τ is the penetration depth for a particular reflection. ϕ_0 and ϕ_h are incident and exit beam angles with respect to the surface plane. $\bar{S}_0$ and $\bar{S}$ are incident and diffracted beam vector. C and G represent crystal and grid respectively.

A brief review of Laplace transformation and inverse Laplace transformation is provided in Appendix C. Note that in Equation 3-4 $\bar{\sigma}(\tau)$ is a continuous function and therefore in order to determine analytical form of function $\bar{\sigma}(\tau)$ a number of experimental results are required for various penetration depth. In order to calculate the stress value at a depth z, the inverse Laplace transform has to be applied on the experimentally calculated stress distribution $\bar{\sigma}(\tau)$. Experimentally, a number of data points can be obtained for various values of penetration depth τ_k, where k is 1,2,3 . . .n. Where n is the total number of data points obtained. Various data points can be generated by tilting the crystal to a different angle and recording reticulographs. Tilting the sample to a different angle, effectively changes the penetration depth of reticulographs. A schematic of diffraction in reflection geometry is presented in Figure 3-1 for illustration.

Assuming that an analytical function $\bar{\sigma}(\tau)$ is determined that fits the data points. In order to further simplify the Equation [3-4] and to reduce the equation to a standard form of Laplace transform we apply the following substitution:

$$s = \frac{1}{\tau} \qquad \text{Equation 3-5}$$

$$\bar{\sigma}\left(\frac{1}{s}\right) = s\int_0^\infty \sigma(z)e^{-zs}dz \quad \text{Equation 3-6}$$

Rearranging we get

$$\frac{1}{s}\bar{\sigma}\left(\frac{1}{s}\right) = \int_0^\infty \sigma(z)e^{-zs}dz \quad \text{Equation 3-7}$$

Defining another function $F(s)$ and substituting

$$F(s) = \frac{1}{s}\bar{\sigma}\left(\frac{1}{s}\right) \quad \text{Equation 3-8}$$

We get

$$F(s) = \int_0^\infty \sigma(z) e^{-zs} dz \quad \text{Equation 3-9}$$

or, $F(s) = \mathcal{L}[\sigma(z)]$ Equation 3-10

The above Equation 3-10 is now the standard form of Laplace transform. Now $\sigma(z)$ can be determined by evaluating inverse Laplace of the function $F(s)$ provided we have already determined the function $F(s)$

$$\sigma(z) = \mathcal{L}^{-1}[F(s)] \quad \text{Equation 3-11}$$

Since the function $\bar{\sigma}(\tau)$ has already been determined, therefore calculating the function $F(s)$ is straightforward. $F(s)$ can be simply determined by replacing τ by $\frac{1}{s}$ in the function $\bar{\sigma}(\tau)$ and then multiplying it by $\frac{1}{s}$.

As an example if $\bar{\sigma}(\tau) = \frac{a}{\tau} + b\tau + c\tau^2 + d\tau^3 + e$ then $F(s) = \frac{1}{s}\left(as + \frac{b}{s} + \frac{c}{s^2} + \frac{d}{s^3} + e\right)$

By taking inverse Laplace transform of the analytical function $F(s)$ we can determine the stress distribution function $\sigma(z)$ and thereby the actual stress value at particular depth z.

There are mainly two problems in determination of stress function $\sigma(z)$. Firstly the scatter of data points can cause difficulty in determining the analytical form of the function $\sigma(\tau)$. The scatter in data points can generate uncertainty in $\sigma(z)$. Second, the choice of analytical function of $\sigma(\tau)$ has an impact on the function $\sigma(z)$. More than one analytical function can fit the data points which can lead to uncertainty in the function $\sigma(z)$. The variation due to error in the experimental data or the scatter in the data can lead to unstable mathematical condition in case the analytical fitting function has too many fitting parameter. This problem can only be handled

by reducing the scatter of data. A similar problem related to stress distribution in case of polycrystalline material is discussed in [65].

3.4 Experimental method

White beam synchrotron X-ray diffraction reticulography experiments were performed at NSLS beamline X19C located at Brookhaven National Laboratory. Multiple images were recorded in reflection geometry by varying the incident angle in steps of 1^0. Reflection geometry allows us to vary experimental parameters to achieve optimum diffraction condition. A fine scale tungsten grid, described in Appendix x, is placed just above and parallel to the sample. Spacing between the bars in the grid is .020" (508μm) and bar width is .004" (102μm). Depth profiles are calculated at locations beneath the surface of the crystal at points defined by the grid-bar intersection locations. It should be noted here that the spatial resolution of this technique is solely depends on the spacing between the bars in the grid. A finer grid (having higher price) will provide better spatial resolution. Incident X-ray beam after interacting with the crystal up to certain depth (penetration depth) diffracts in certain direction governed by Bragg's law. Diffracted beam after passing through the tungsten grid forms an image on the photographic film (Agfa structurix D3-SC) which essentially is the shadow or the inverse image of the grid. Reticulographic images were recorded using Agfa Structurix D3-SC photographic film.

A series of scans of the X-ray film recorded at various incident beam angle is given in Figure 3-6. A simulated plot of Laue pattern is generated using the software LauePt for comparison and indexing purpose. In the transmission geometry it was not necessary to index the reticulographs and it was also not necessary to determine the wavelength or the penetration depth of a particular reticulograph. Unlike transmission geometry it is necessary to index the reticulograph because wavelength information is required for penetration depth calculations. LauePt program not only provides the index of the pattern but also the wavelength for each diffraction spot and the geometrical location of the spot on the film. These data are required for penetration depth calculation.

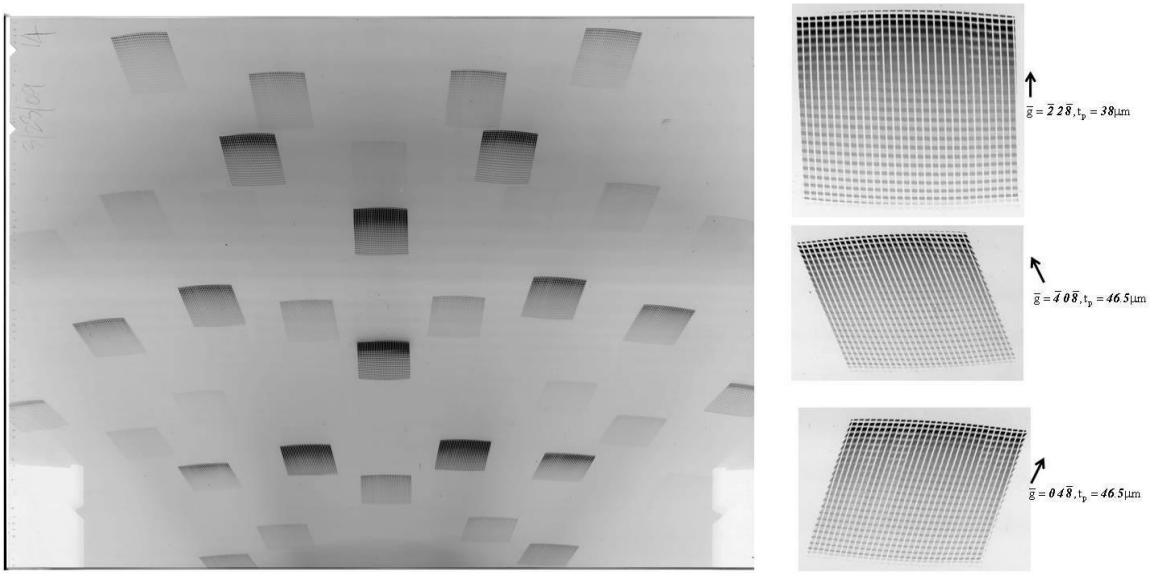
$\bar{g} = \bar{2}\,2\,\bar{8}, t_p = 38\mu m$
$\bar{g} = \bar{4}\,0\,\bar{8}, t_p = 46.5\mu m$
$\bar{g} = 0\,4\,\bar{8}, t_p = 46.5\mu m$

(A)

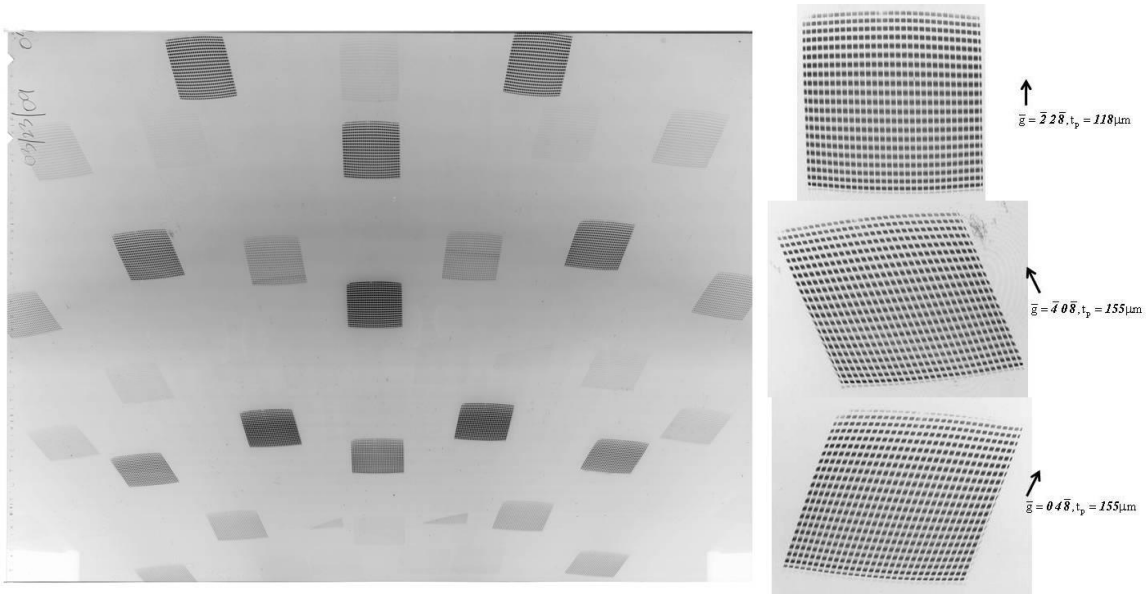
$\bar{g} = \bar{2}\,2\,\bar{8}, t_p = 118\mu m$
$\bar{g} = \bar{4}\,0\,\bar{8}, t_p = 155\mu m$
$\bar{g} = 0\,4\,\bar{8}, t_p = 155\mu m$

(B)

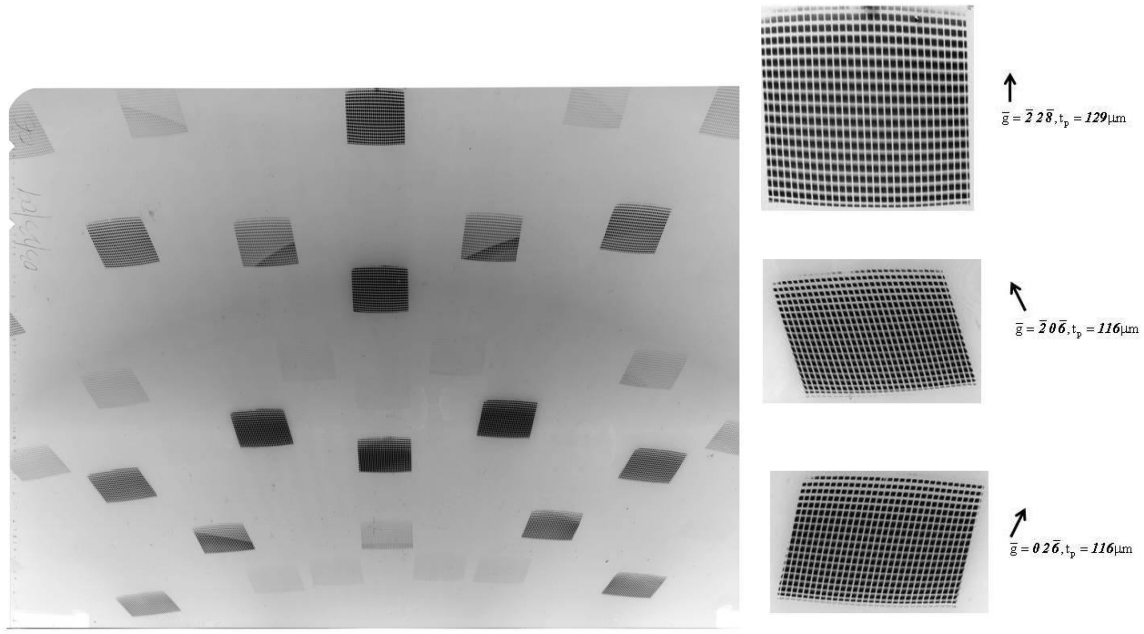

(C)

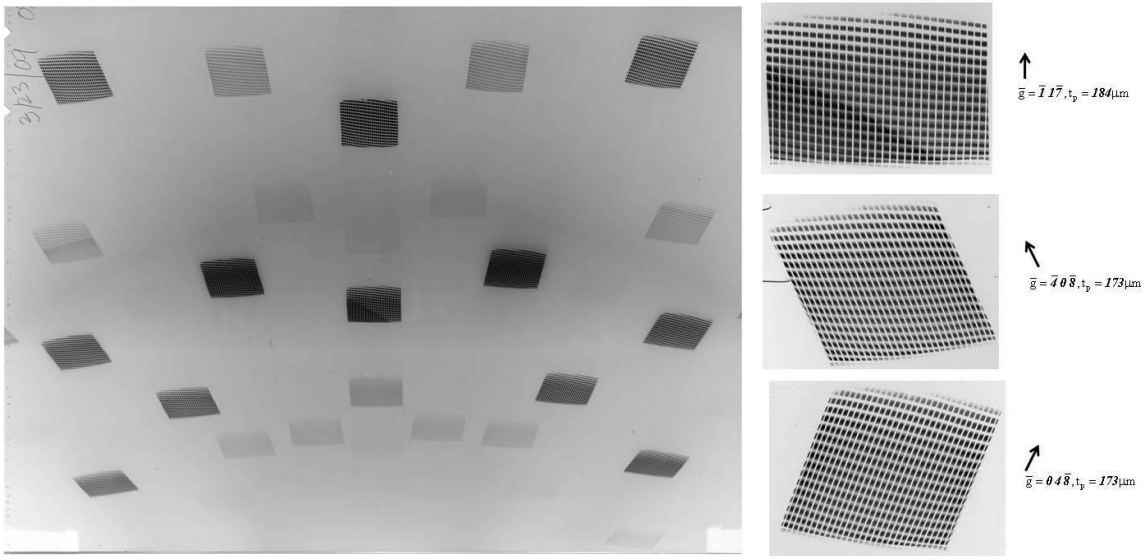

(D)

Figure 3-6: Scan of a X-ray films,Laue pattern is recorded in the reflection geometry. LauePt [] program is used for indexing the pattern, calculating the location of the diffracted spot and the wavelength of the diffracted beam. (A) is recorded at 1^0 tilt, (B) is recorded at 5^0 tilt, (C) is recorded at 7^0 tilt and (D) is recorded at 9^0 tilt,

After exposure to X-rays, films are processed by developing, fixing rinsing and followed by drying. Films are scanned at a resolution of 2400 dots per inches (dpi). An electronic image file (.tiff) is generated. Image recognition software is used to detect the grid corner points in the three chosen reticulograph.

In principle any three reticulographs can be chosen but in general, an arbitrarily chosen reticulograph can have widely different penetration depth. In order to resolve this issue, three set of reticulographs are to be chosen whose peneteration depth are close to each other. First we determine penetration depth of all the reticulographs that were recorded on the X-ray film, and then we chose a set of three reticulograph with penetration depth which are as close as possible to each other. One way to do this is to select a reticulograph from the vertical center line (line of symmetry) and other two symmetrical reflections having penetration depth near the previous reflection. The average of three penetration depth is considered as the "information depth" as the calculated stress represents the average (exponentially decaying) from that depth. Three chosen reticulographs in each of the film are shown in Figure 3-6.

Using image recognition software program, grid corner coordinate points in the three reticulographs are calculated. Corner points of three reticulographs formed by the intersection of grid-bars are calculated.

$F_{1i} = \left(x^F_{1i}, y^F_{1i}, z^F_{1i}\right)$: Array of coordinate points from reticulograph 1

$F_{2i} = \left(x^F_{2i}, y^F_{2i}, z^F_{2i}\right)$: Array of coordinate points from reticulograph 2

$F_{3i} = \left(x^F_{3i}, y^F_{3i}, z^F_{3i}\right)$: Array of coordinate points from reticulograph 3

F indicates points on the film and i is 1, 2, 3, . . . n array of points formed by grid at which stress is being measured.

Coordinate points on the crystal surface $C_i = \left(x_i^C, y_i^C, z_i^C\right)$ are also known. C indicates points on the crystal and i as previously defined.

Diffraction vector $\bar{S}$ is determined simply by subtracting coordinate points of rericulograph (F_i) from corresponding coordinate points of crystal (C_i). We divide this vector by its magnitude in order to make the diffraction vector a unit vector.

$\bar{S}_{1i} = \frac{(F_{1i} - C_i)}{|F_{1i} - C_i|}$: Unit diffraction vector of reticulograph 1 of array point i. Equation 3-12

$\bar{S}_{2i} = \frac{(F_{2i} - C_i)}{|F_{2i} - C_i|}$: Unit diffraction vector of reticulograph 2 of array point i. Equation 3-13

$\bar{S}_{3i} = \frac{(F_{3i} - C_i)}{|F_{3i} - C_i|}$: Unit diffraction vector of reticulograph 3 of array point i. Equation 3-14

Incident beam vector is $\bar{S}_0 = -\hat{j}$ following the coordinate system of Figure 3-1.

Unit plane normal vector $\bar{n}$ can therefore be calculated by subtracting the incident and diffracted beam vector.

$$n_{1i} = \frac{\bar{S}_{1i} - \bar{S}_0}{|\bar{S}_{1i} - \bar{S}_0|}; n_{2i} = \frac{\bar{S}_{2i} - \bar{S}_0}{|\bar{S}_{2i} - \bar{S}_0|}; n_{3i} = \frac{\bar{S}_{3i} - \bar{S}_0}{|\bar{S}_{3i} - \bar{S}_0|} \quad \text{Equation 3-15}$$

This calculation is repeated for each point on the crystal to generate local plane normal at each array point i and for three different reticulographs. These plane normal are then used in the equation 2-11 A through I to calculate nine unknown tensor components $[u_{ij}] = \frac{\partial u_i}{\partial j}$ where i,j are x, y or z at each array points. By using the values of $\frac{\partial u_i}{\partial j}$ strain and hence stress is calculated using Equation 1-18 and 1-19 respectively at each array point i. The strain and stress values are generated and mapped over the entire crystal surface. An example is shown in Figure 3-7 Experimental condition: tilt angle 5, reticulograph used -2 2 -8, -4 0 -8, 0 4 -8 . This strain and stress values represent exponentially weighted average of strain and stress up to the "information" (penetration) depth. As mentioned previously these weighted average stress and strain values are of very little use. Real space stress values are calculated using the Laplace stress profile.

3.5 Results and discussion

Three reticulographs were selected in a X-ray film based on the criteria that all three of them have similar penetration depth. Even though, it is not a requirement of the SMART technique to have a symmetric diffraction pattern, it is useful for calculation purposes if one starts with a symmetric diffraction pattern. It can be seen that the recorded Laue patterns in Figure 3-6 are symmetrical about its vertical center line. A comparison of simulated Laue pattern generated by program LauePt is shown side by side which is useful in indexing the pattern. It should be noted that the corresponding symmetrical spots belong to the same family of crystallographic planes in the Silicon and also because of symmetry reasons, both of the diffraction spots have same penetration depth.

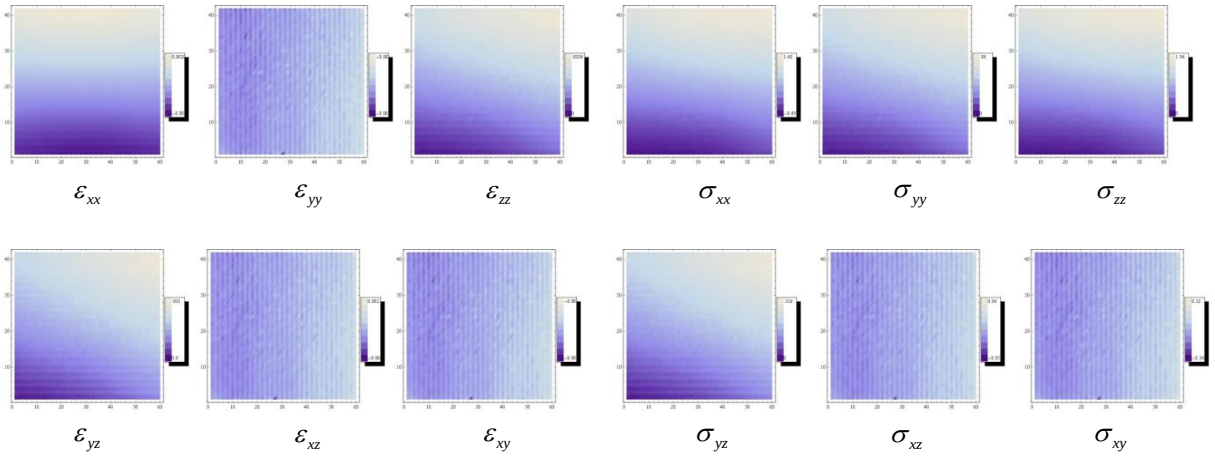

Strain	ε_{xx}	ε_{yy}	ε_{zz}	ε_{yz}	ε_{xz}	ε_{xy}
Min.	-0.0017	0.0000	0.0000	0.0000	-0.0028	-.0011
Max.	0.0021	0.0027	0.0034	0.0011	0.0028	.0010

Stress	σ_{xx}	σ_{yy}	σ_{zz}	σ_{yz}	σ_{xz}	σ_{xy}
Min.	-0.4945	0.0000	0.0000	-0.3460	-0.8536	0.0000
Max.	1.4099	1.4000	1.9486	0.3248	0.8413	3.1617

Figure 3-7: Weighted average strain and stress maps at the depth of 50 μm.

Strain and stress calculations were done for four different penetration depths by choosing x-ray films recorded at different incidence angle. Summary of experimental condition, reticulograph used, and penetration depth information is given in table below:

Table 3-1: Summary of reflections used and corresponding penetration depth

Sl. No.	Tilt angle ϕ_0	Reticulograph1 h k l (λ), t_p	Reticulograph2 h k l (λ), t_p	Reticulograph3 h k l (λ), t_p	Avg. penetration depth
A	5^0	-2 2 -8 (.53), 118	-4 0 -8 (.48), 155	0 4 -8 (.48), 155	142.6
B	7^0	-2 2 -8(.57), 129	-2 0 -6(.58), 116	0 2 -6(.58), 116	120.3
C	9^0	-1 1 -7(.53), 184	-4 0 -8(.55), 173	0 4 -8(.55), 173	176.7
D	1^0	-2 2 -8(.45), 38	-4 0 -8(.4), 46.5	0 4 -8(.4), 46.5	43.7

In order to calculate stress depth profile at an arbitrary location, we first plot calculated weighted average stress versus penetration depth and generate a best fit curve. This weighted average stress function is then transformed in order to reduce the equation into standard Laplace transform. Inverse Laplace Transform of this function will give the stress as a function of depth (z).

As an example, calculation for stress depth profiling of the component σ_{zz} is demonstrated at a location on crystal surface. Experimentally determined weighted average stress at various penetration depth is given in Table 3-3 below:

Table 3-2: Table of penetration depth (τ_p) and calculated stress value $\bar{\sigma}_{zz}(t_p)$

Reticulograph #	Penetration depth	$\bar{\sigma}_{zz}$
-	0	0
1	52	-1.88
2	120	-0.8855
3	143	2.29
4	177	.266

A plot of average stress as a function of depth is shown in Figure 3-8 and the analytical function for this set of data is determined using Mathematica is:

$$\bar{\sigma}_{zz} = 0.082 - 0.112\tau + 0.0016\tau^2 - 5.323 * 10^{-6}\,\tau^3 \quad \text{Equation 3-16}$$

Transforming Equation 3-16 by substituting τ by 1/s and multiplying by 1/s we get:

$$F(s) = \frac{1}{s}\left(0.082 - \frac{5.323 * 10^{-6}}{s^3} + \frac{0.0016}{s^2} - \frac{0.112}{s}\right) \quad \text{Equation 3-17}$$

Taking Inverse Laplace of this function will give the real stress depth profile, is given by the analytical function:

$$\sigma_{zz} = 0.082 - 0.112z + 0.0008z^2 - 8.88 * 10^{-7} z^3 \quad \text{Equation 3-18}$$

A plot of the stress profile is given in Figure 3-8 up to 200μm in depth.

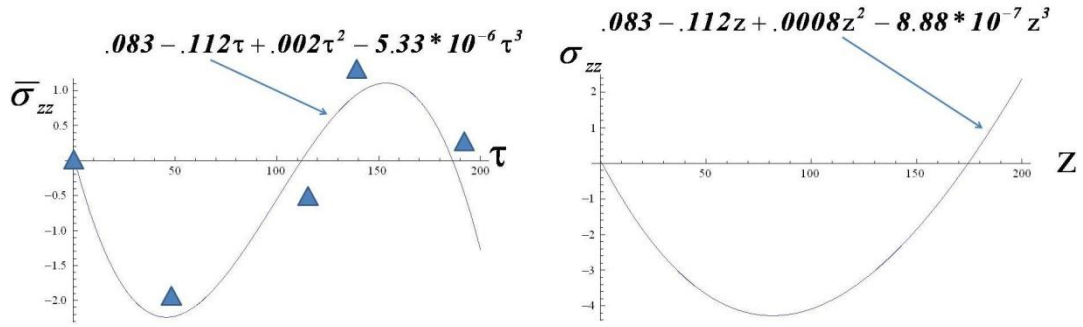

(A) (B)

Figure 3-8: (A) Experimentally calculated weighted average stress profile (zz component), best fit curve is generated using the data points (B) Real stress profile is generated by taking inverse Laplace transform of function F(s) generated by weighted average stress profile.

Given below is the code in Mathematica that is used for generating these equations and plots:

```
datazz={{0,0.00}, {52,-1.88},{120,0.88},{143,2.29},{177,0.266}};
curvezz = Fit[datazz,{1,x,x^2,x^3},x];
 %
Plot[curvezz,{x,0,200}]
curvezz1=(1/s)*(curvezz/.x→1/s);
curvezz1
sigmazz=InverseLaplaceTransform[curvezz1,s,t];
Plot[sigmazz,{t,0,200}]
```

Similar calculation is been done for other five stress components. A complete stress depth profile at a location in the crystal is given in Figure 3-9.

We have repeated this calculation over the crystal area in order to determine the full state of stress determined at each point within the crystal. Using the stress depth profiles we have generated stress maps at a depth below the surface, as an example stress maps at 50μm, 100μm and 150μm is plotted in Figure 3-10.

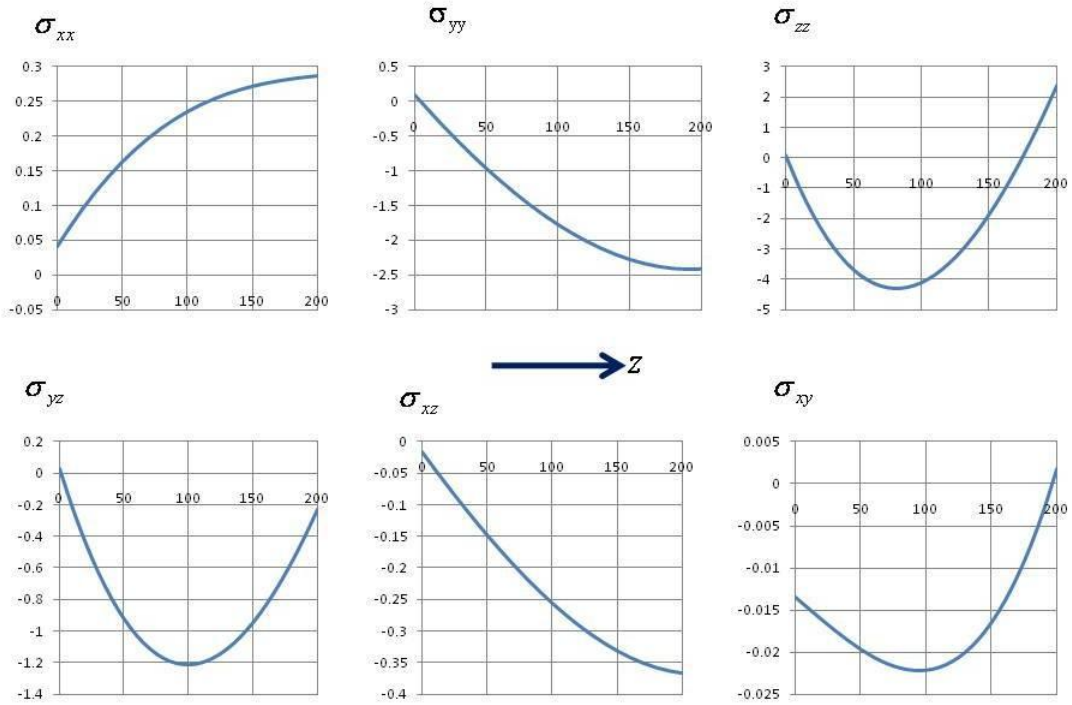

Figure 3-9: Six components of stress at a location as a function of depth.

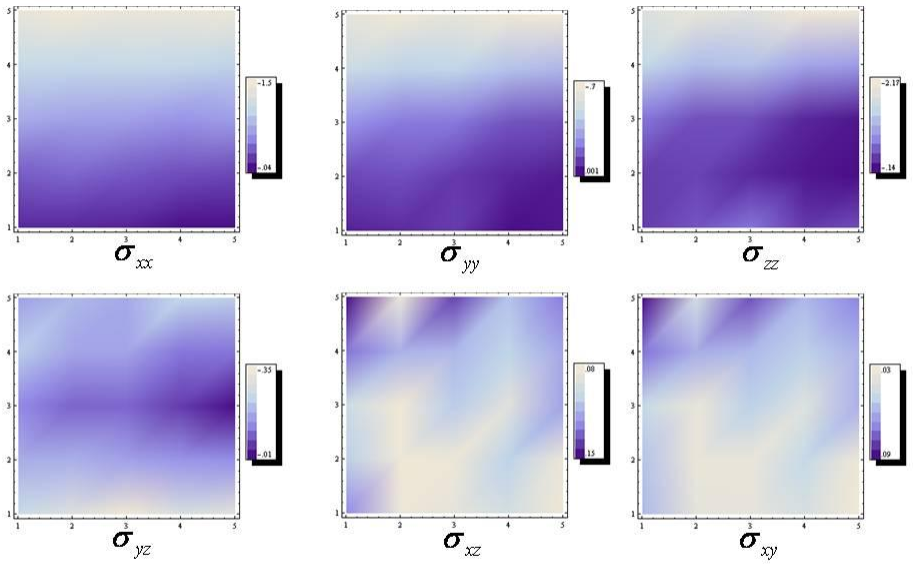

(GPa)	σ_{xx}	σ_{yy}	σ_{zz}	σ_{xy}	σ_{xz}	σ_{yz}
Min.	-1.50	-.70	-2.17	-.35	.08	.03
Max.	-.04	.001	-.14	-.01	.15	.09

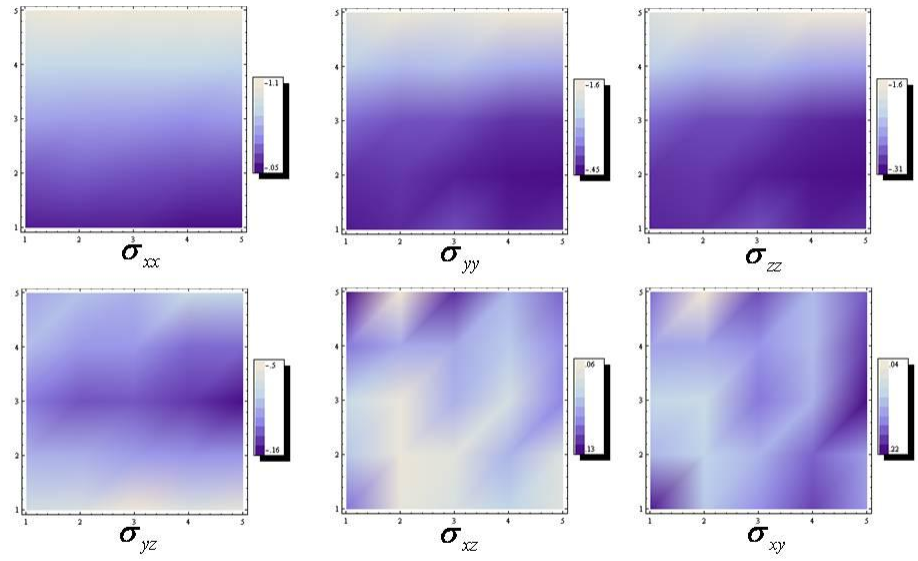

(GPa)	σ_{xx}	σ_{yy}	σ_{zz}	σ_{xy}	σ_{xz}	σ_{yz}
Min.	-1.1	-1.6	-1.6	-.5	.06	.04
Max.	-.05	-.45	-.31	-.16	.13	.22

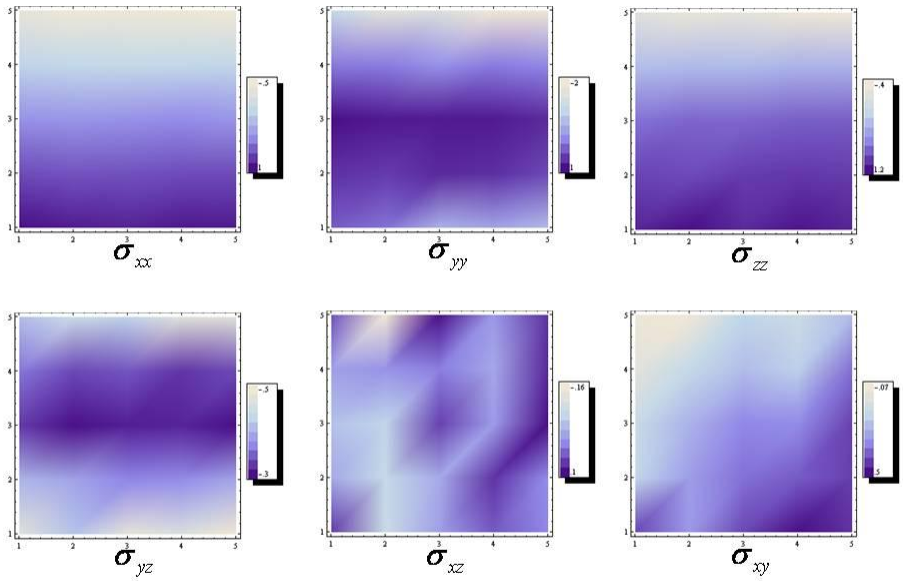

(GPa)	σ_{xx}	σ_{yy}	σ_{zz}	σ_{xy}	σ_{xz}	σ_{yz}
Min.	-.5	-2.0	-.40	-.50	-.16	-.07
Max.	1.0	1.0	-1.2	-.30	-.10	.50

Figure 3-10: Stress maps of all six stress components at a depth of 50μm, 100μm and 150μm below the surface.

Errors in stress calculations in reflection geometry are similar to the errors in transmission geometry, namely error in determination of coordinate points and specimen to film distance. The definition of penetration depth whether 1/e or 1/10 also affects the depth profile by the same proportion but the overall shape of the curve remains the same.

3.6 Alternate approach to SMART technique

In our approach to stress measurement using SMART technique we have assumed a stress free location in the crystal. In many instances a stress free location in the crystal does not exist. In those cases we have taken least stress location, determined by the least distortion at the same corresponding location in three reticulographs simultaneously.

SMART technique of stress measurement calculates stress at a location which is relative to the least stress location. Therefore all the stress values are relative stress values with respect to least stress location.

In order to determine absolute stress, we have calculated stress free plane normal by determining diffraction spot's coordinate in the stress free crystal. This stress free plane normal can then be used for determining stress at any arbitrary location in the crystal. This alternative approach for stress determination is applied in both transmission and reflection geometry. A description of this technique and the results obtained are discussed below. In this approach essentially the stress free plane normal vector is calculated from the theoretical location of Laue points in stress free crystal.

Transmission geometry: A packaged Silicon die is used for determining stress at selected locations in the crystal. Similar to SMART technique, a Laue pattern is recorded at a known specimen to film distance. Crystal is aligned as much as possible such that a symmetric Laue pattern is recorded. Using the software program LauePt [48], a theoretical Laue pattern is generated with spot size same as the sample size as shown in Figure 3-11. X-ray film is superimposed on the theoretical Laue pattern on the computer screen. Angular rotation (θ_x, θ_y & θ_z) and specimen to film distance is precisely adjusted in the LauePt program such that all the Laue spots on X-ray film matches with the simulated program. Coordinates of selected Laue spots are determined from the LauePt software by double clicking left mouse button on the spot. From the stress free (theoretical) coordinate points, stress free plane normal vector is calculated. Plane normal vectors at selected locations are also calculated from the film. From these two plane normal vectors stress tensor is determined following the procedure of SMART technique as described in section 2-2. Stress tensor values calculated at selected locations are given in Figure 3-12.

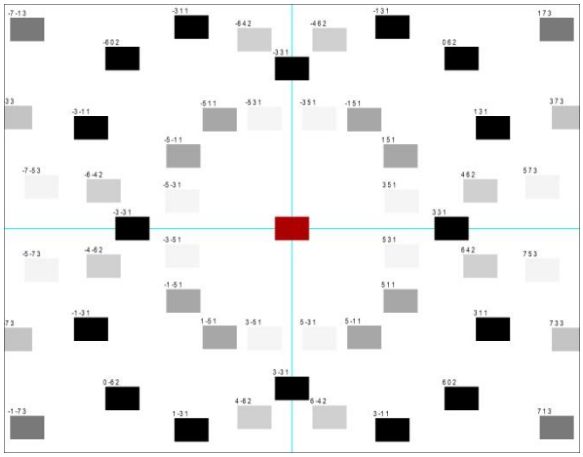

Figure 3-11: Simulated Laue pattern generated to match with the X-ray film.

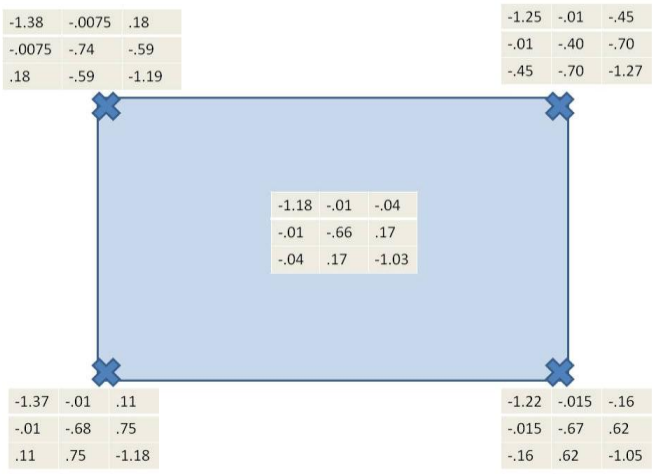

Figure 3-12: Stress tensor values determined at selected locations using alternate approach to SMART.

Reflection geometry: In reflection geometry, same concept is applied as in transmission geometry where the stress free plane normal vector is calculated from theoretical coordinate points of Laue spots. X-ray films superimposed on the computer screen of LauePt program and angles (θ_x, θ_y & θ_z) and specimen to film distance are precisely adjusted such that the Laue spots on the film matches with the Laue spots on the computer screen of the program. Coordinate points of theoretical Laue spots are calculated for selected three spots. Three Laue spots are chosen such that they have similar penetration depth.

Stress free plane normal vector is calculated from the coordinate points of theoretical Laue spots. Plane normal vector of the selected points on the crystal is calculated from the coordinate points on the film.

Following the procedure, described in Section 3-3 stress tensor at selected location is calculated from stress free and stressed plane normal vectors.

A total of four sets of calculations were carried out for different penetration depths. Stress values were measured at same location on crystal surface and at different penetration depth.

Summary of reflection used and penetration depths are given in Table 3-3 below. Results of the stress values at different penetration depth are summarized in Figure 3-13 below.

Table 3-3: Summary of reflections used and penetration depth.

Sl. No.	Tilt angle	Reflection 1	Reflection 2	Reflection 3	Avg. pen. depth
A	5^0	-1 1 -5	-3 1 -7	-1 3 -7	63µm
B	7^0	-2 2 -8	-1 3 -7	-3 1 -7	83µm
C	5^0	-2 2 -8	-2 0 -6	0 2 -6	120µm
D	9^0	-1 1 -7	-4 0 -8	0 4 -8	176µm

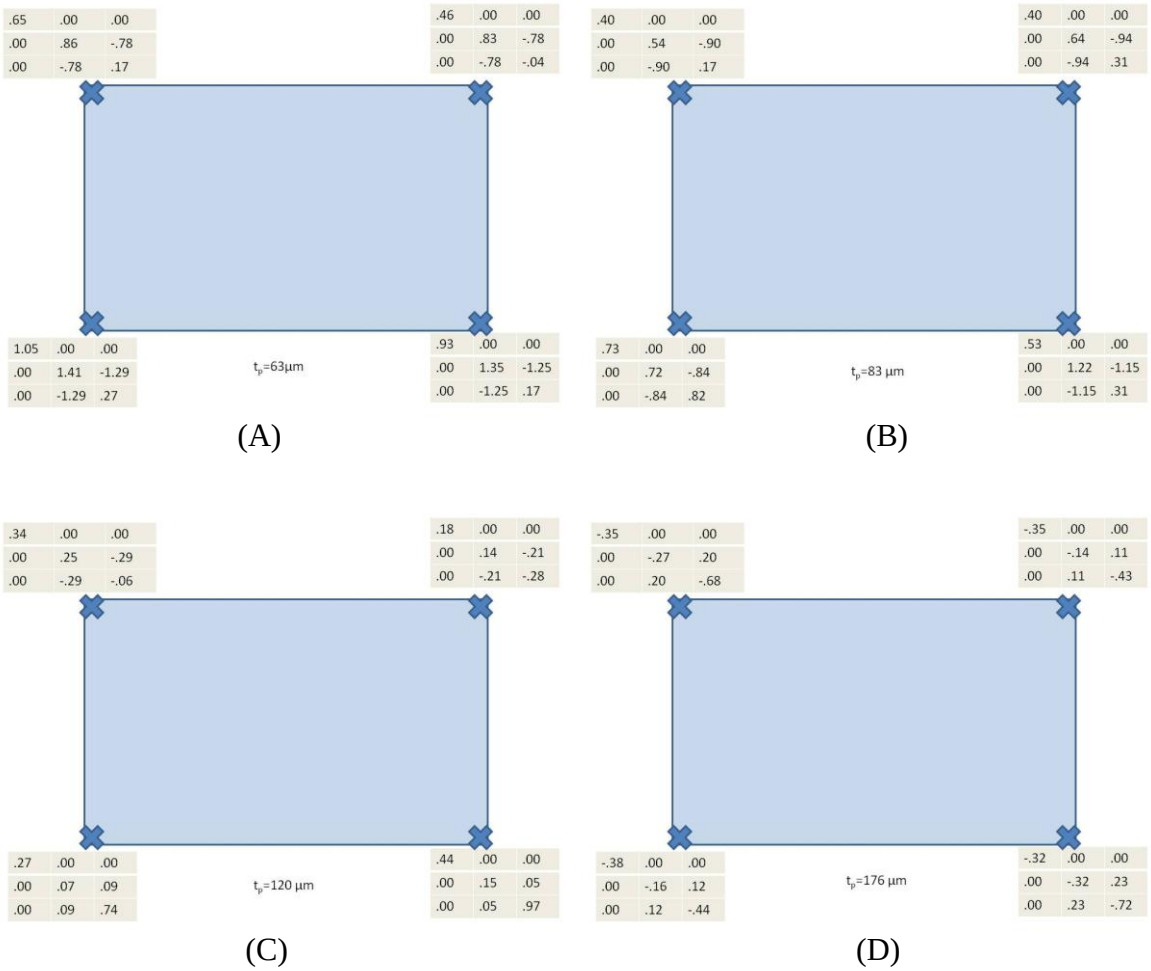

Figure 3-13: Stress values calculated at different penetration depth (t_p) using alternate method of SMART

From the calculated stress values at different depths and applying the procedure of Section 3-3, depth profile of each stress component is determined. Values of stress tensor at surface are determined from the stress profile at z=0 is given in Figure 3-14 below. Note that the surface stress tensor value can be determined either by setting z=0 in the depth profile (real space stress profile) or by setting z=0 in the weighted average stress profile (Laplace space stress profile).

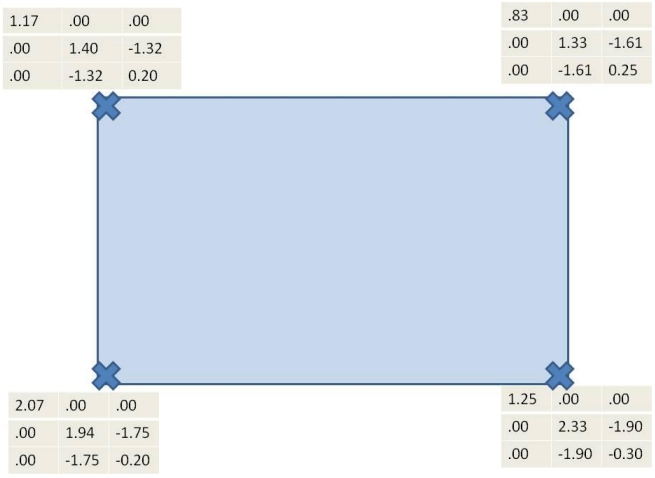

Figure 3-14: Surface stress tensor values after extrapolation to z=0.

σ_{xx} and σ_{yy} are positive implying tensile in-plane stress which is considerably greater than rest of the components. σ_{zz} is relatively small and ideally will be zero.

Error associated with depth profiling: Error associated with stress values in depth profiling is more than error for stress calculation at a location using SMART technique. This can be seen quite simply from the schematic graph in Figure 3-14.

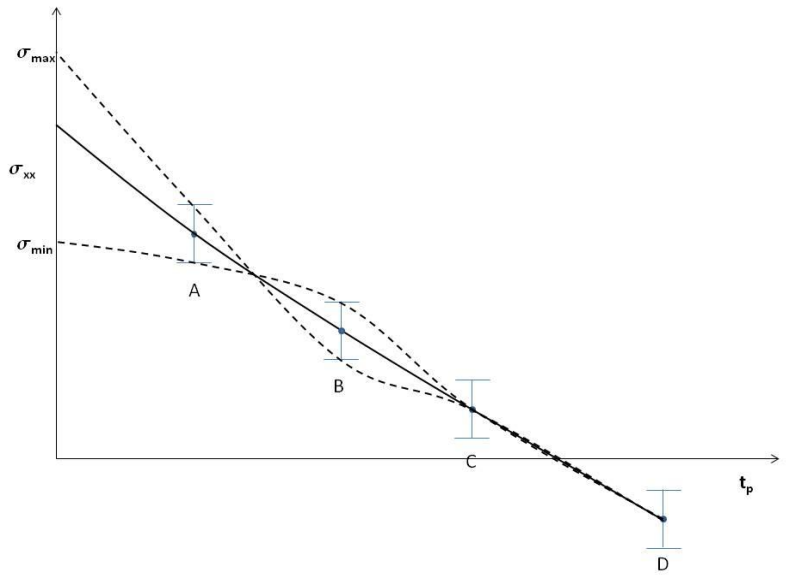

Figure 3-15: Schematic plot of depth profile showing error associated in determining surface stress.

Assuming an error of ±10% in stress value, error bars are shown for corresponding stress values. In case the top point in A and the bottom point for B is chosen the stress value at surface is significantly higher (σ_{max}). In the opposite case if lowest value of stress at point A and highest value of stress at point B is taken the resultant stress at surface is significantly lower (σ_{min}). Therefore, in depth profiling the error in surface stress value derived from curve fitting and interpolation is higher than error in direct stress calculation using SMART.

As an example if we consider stress profile σ_{xx} of bottom left corner, surface stress is 2.07GPa. If we consider stress at 63µm to be 10% higher (1.155GPa) and stress at 83µm to be 10% lower (.657GPa) then after interpolation the surface stress is 2.44GPa. In the other case, if we consider stress at 63µm to be 10% lower (.945GPa) and stress at 83µm to be 10% higher (.803GPa) then after interpolation the surface stress is 1.69GPa. Therefore in this example the error in surface stress estimation is from 2.44GPa to 1.69GPa.

3.7 Conclusion

A novel non-destructive technique using white beam synchrotron X-ray reticulography to determine all strain and stress tensor components has been demonstrated in packaged silicon die and can be extended to any single crystal material. Using this method, strain and stress tensor

components are determined at an arbitrary location inside the crystal up to the penetration depth of the crystal. The spatial resolution of this technique is dependent on the grid spacing. A finer scale grid will have higher spatial resolution.

Diffraction data if generated by utilizing white beam synchrotron radiation in reflection geometry. Reflection geometry allows us to control the penetration depth of X-ray. Residual stress is calculated using these data, which represents exponentially decaying weighted average stress value with respect to penetration depth. Combining various weighted average stress value for different penetration depth we generated an analytical form of Laplace stress profile. Inverse Laplace transform of this stress profile will yield real space stress profile. This calculation is repeated for each array points on the crystal surface defined by the grid and complete stress profile is generated for the crystal up to penetration depth.

Thermo-mechanical stresses introduced in the crystal during semiconductor processing and final packaging can be determined as the crystal goes through various processing steps. This can provide as a standard quality tool which can be incorporated in the production and can provide insight into state of stress within the crystal which can be used for process optimization. Understanding of state of stress at various locations within the crystal is critical in designing the integrated circuit. Residual stress can create not only unintended electrical performance but also crack the crystal.

Efforts is been made in order to transfer this technique from synchrotron source to lab source. Because of this techniques uniqueness, versatility and the simplicity a completely automated turnkey system can be developed for use in industrial setup. Steps taken toward this goal and future work are described in Chapter 5.

Chapter 4 Edge defect characterization of dies

4.1 Introduction

During microelectronic chip manufacturing, wafers are sliced into rectangular dies before they are encapsulated into a package. The dicing process usually performed using diamond saw, laser, scribing and breaking or with their combination. These process causes damage to the newly formed surface. Cut quality of Silicon wafer and the effect of various processing parameters is studied by Tang et al. [66]. The effect of ultra-precision grinding on the microstructural changes in single crystal silicon and grinding induced subsurface cracks in Silicon wafers are studied by Zarudi et al. [67, 68] and Pei et al. [69] respectively. These damages including surface scratch, dislocations and nano-crack that can propagate into the bulk of the crystal and interfere with the device function and ultimately may destroy the device. Therefore, understanding the nature and origin of these defects is important in order to prevent or minimize its occurrence. Here we have done an in-depth characterization of surface defects using various characterization techniques including synchrotron white beam X-ray diffraction topography (SWBXT), Nomarski optical microscopy (OM), scanning electron microscopy (SEM) and transmission electron microscopy (TEM).

The mechanical and electrical reliability of a semiconducting chip is affected by the quality of the surface created by the dicing and grinding process. The substrate is attached to the die using an under-fill which acts as an adhesive between the die and the substrate. The thermal mismatch between the die and substrate causes residual stress and bending in the assembly. Surface and edge defects are the main cause of concern for mechanical reliability of the device. Defects, which are the weak spot in any crystal, can act as a crack initiating region. Three different modes of crack initiation and propagation are shown schematically in Figure 4-1, cracks can initiate in a die surface at the tension side or from the edge of die[3]. In our current study we have investigated defect structure at the edge caused by dicing process.

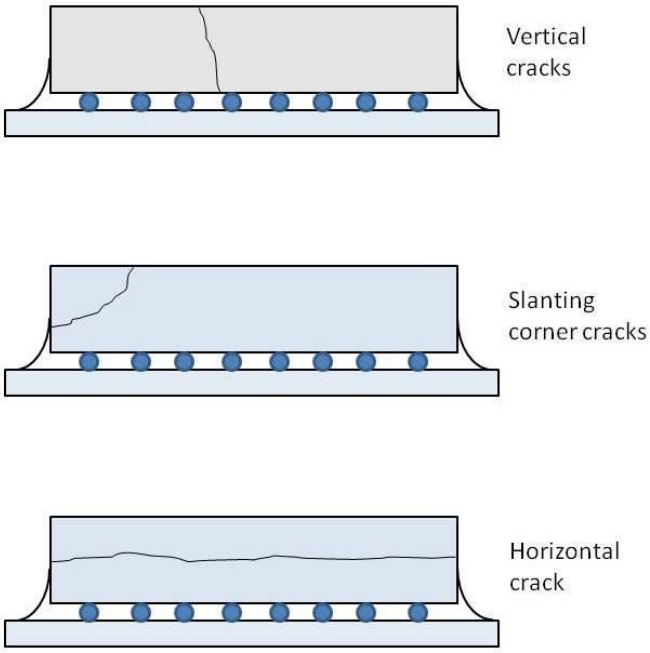

Figure 4-1: Schematic of various crack modes in a die.

The nucleation and propagation of defects from die edges, caused by damage from cutting and processing, strongly influence the reliability and performance of the device. Understanding of the type and density of edge defects and their propagation under thermo-mechanical stress during temperature cycling can facilitate the development of optimized cutting process by minimizing the generation of edge defects. In order to simulate temperature cycle in a working chip we designed and developed an environmental chamber for in-situ X-ray diffraction topography. Design of the environmental chamber (furnace) and the experimental setup is described in Section 4-5.

4.2 Surface characterization

Various techniques has been cited in literature for inspecting surface and subsurface damage including optical microscopy [70], X-ray diffraction [71], transmission electron microscopy [72] and laser light scattering [73] . X-ray diffraction topography is an important tool for surface characterization of single crystal material [74]. It is a non-destructive method to inspect surface and sub-surface damage. X-ray diffraction topography provides information (image) of strain fields around the defect and crystallographic misorientation. Standard

commercial X-ray diffraction equipments are available for imaging as large as 300 mm diameter wafers in both reflection and transmission geometry [75] 300mm Silicon wafers are topographed using white beam is reported by Danilewsky et al. [76]. Monochromatic 300mm-wide synchrotron radiation is used by Kawado et al. [77] in asymmetric reflection geometry to detect point-to-point variation in surface strain at different stages of Silicon wafer manufacturing such as slicing, lapping, etching, grinding and polishing. Glancing angle X-ray topography, where incident angle is greater than critical angle for total external reflection is reported by Black et al. [78] to image Silicon thin film to penetration depth as little as 6nm. Grazing incident X-ray diffraction topography using total external reflection where incident and exit angle are less than critical angle is also been reported for observing surface and up to few Angstrom in depth. For example synchrotron X-ray topography is used in total external reflection mode to observe strain induced surface bumps due to underlying misfit dislocation [79, 80]. X-ray diffraction topography is used as a complimentary technique used along with other surface characterization method in order gain richer understanding of surface and sub-surface defect structure. One of the advantages of this technique is the tunability of the depth from which information is extracted or the penetration depth. Penetration depth can be changed simply by changing the diffraction condition i.e. angle of incident (or exit) between incoming (or diffracted) X-ray beam and crystal surface. By varying the imaging conditions such as choice of diffracting planes, wavelength (energy) of X-rays, angle of incidence and diffraction angle one can control the penetration depth and hence isolating the structure below the penetration depth.

An X-ray diffraction topograph is an image recorded on a detector, of a diffracted beam when an area-filling X-ray beam illuminates a crystal sample. Synchrotron white beam X-ray topography (SWBXT) experiments were carried out at the Stony Brook Topography Facility (Beamline X-19C) at the National Synchrotron Light Source, at Brookhaven National Laboratory. The X-ray beam had a wavelength spectrum ranging from 0.1 to 2.00 Å, with peak intensity at around 0.8 Å. Primarily two different geometries are used for recording surface X-ray diffraction topograph. Schematic of experimental setup for both configurations are shown in Figure 4-1 A and B respectively. In configuration A, edge is perpendicular to incident beam whereas in configuration B edge is parallel to the incident beam. X-ray film can be place anywhere around the sample, two film positions which were commonly used in order to image desired topograph are shown in the schematic, one in front and another on top of sample. The

specimen-film distances were set to be 15cm -20cm in front geometry and about 40-45 cm in top geometry, depending on background noise and desired diffraction topograph.

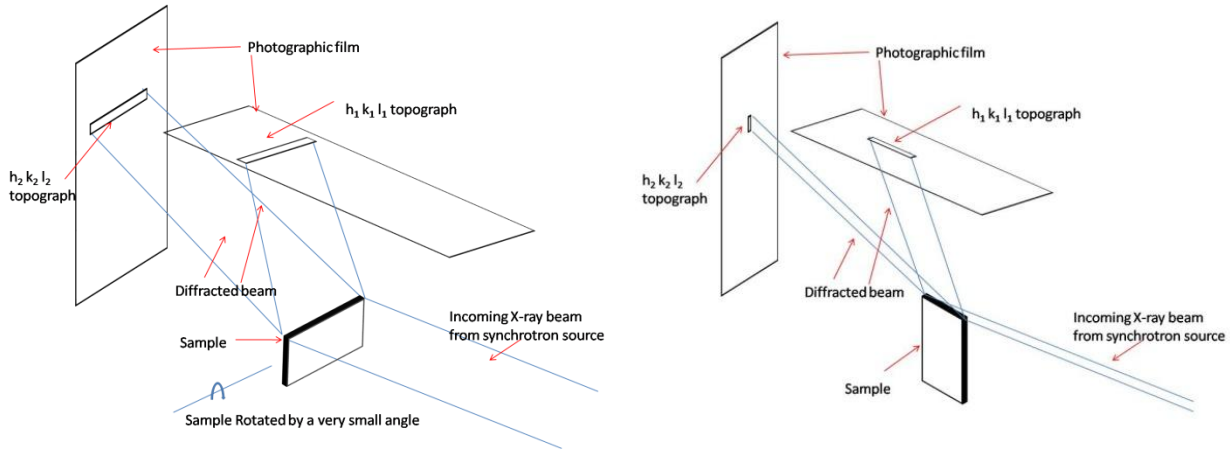

Figure 4-2: Schematic of experimental setup for recording surface X-ray diffraction topograph in reflection geometry.

X-ray topographic images were recorded from the edge surface of the die as shown in Figure 4-2. The Laue pattern is recorded on the photographic film (Agfa Structurix D3-SC), enabling us to observe multiple topographic images simultaneously. Selected topograph of the edge is shown in Figure 4-2 and high magnification image of a selected region in the topograph is also shown.

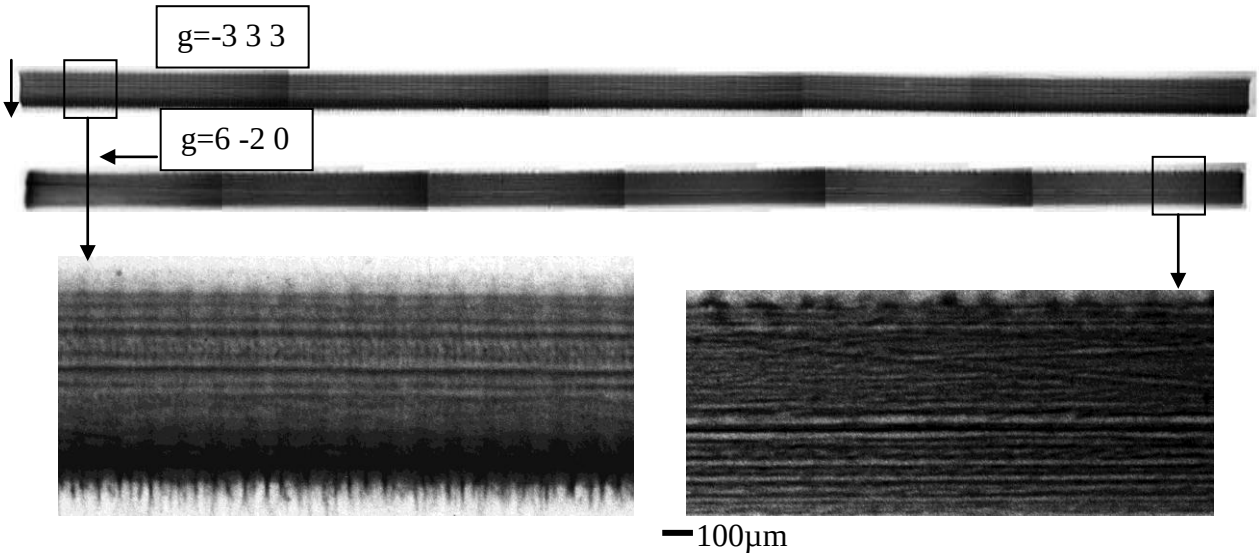

Figure 4-3: Topograph of the entire edge and high magnification image of a selected region in the topograph with different $\bar{g}$ vector. (A) -3 3 3 reflection (B) 6 -2 0 reflection (C) High

magnification image of selected region in the of -3 3 3 topograph (D) High magnification image of selected region in the of 6 -2 0 topograph. Strain fields are more pronounced with sharper contrast in the 6 -2 0 topograph as the g vector is parallel to the edge indicating that the strain fields are parallel to the edge due to cutting process.

Comparison with optical images: Optical images of die edge are taken using Nomarski optical microscope. The Nomarski optical microscopy was performed using a Nikon Ellipse E600 JSL Optical Microscope. Image of a section of the edge is shown in Figure 4-3. A high magnification image of a selected area on the edge is also shown. Features such as surface striation, scratch and an interface can be seen on both the low and high magnification images.

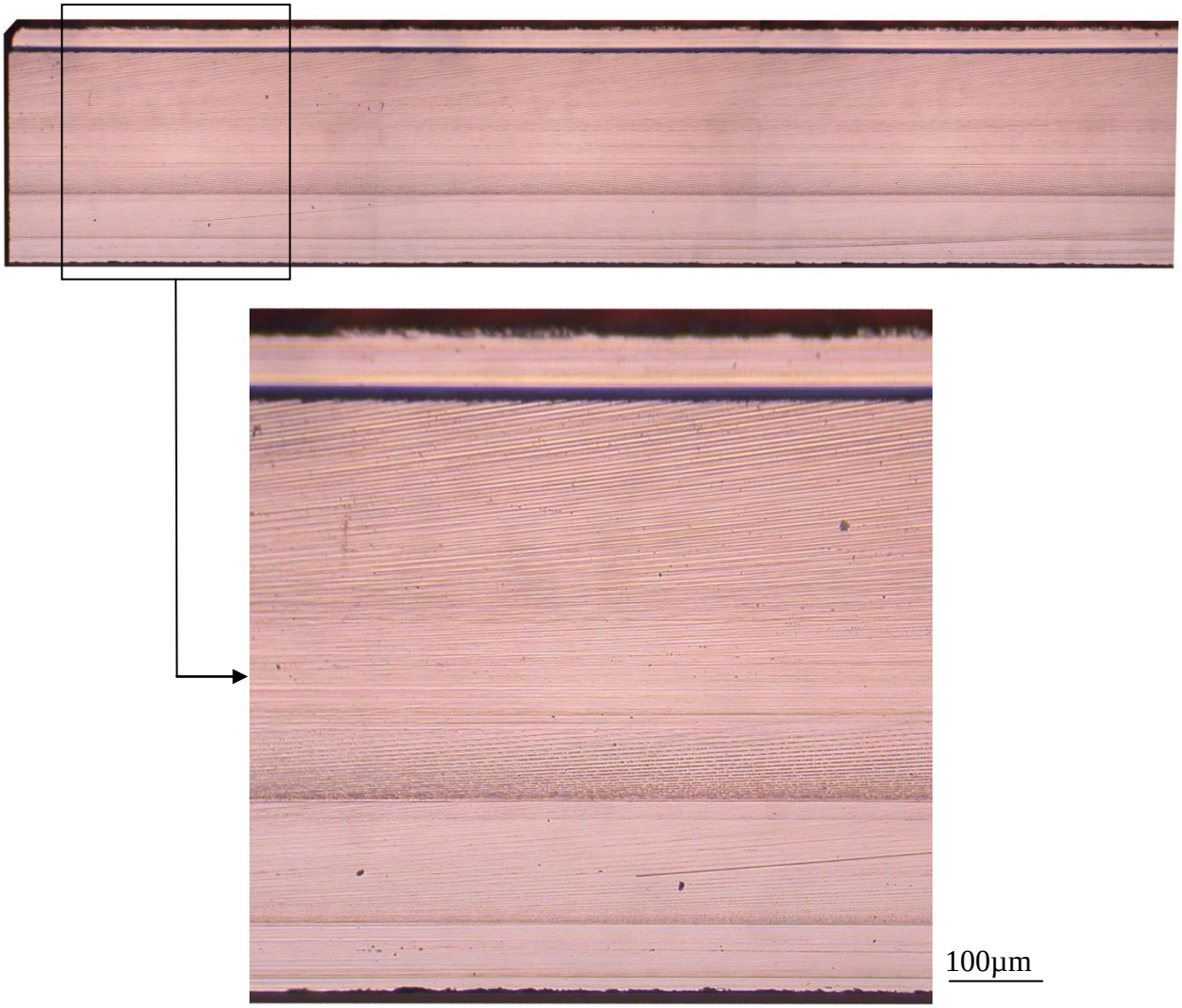

Figure 4-4: Optical images taken using Nomarski microscope. (A) Section of the edge is shown and (B) high magnification image of a selected area is shown.

Comparison with scanning electron microscopy (SEM): SEM images were taken using microscope model LEO1515. Optical observation (Figure 4-4) and SEM observation (Figure 4-5) revealed the rough surface, which agree with the result from SWBXT. Detailed investigation of the microstructures of the films is carried out using cross sectional TEM.

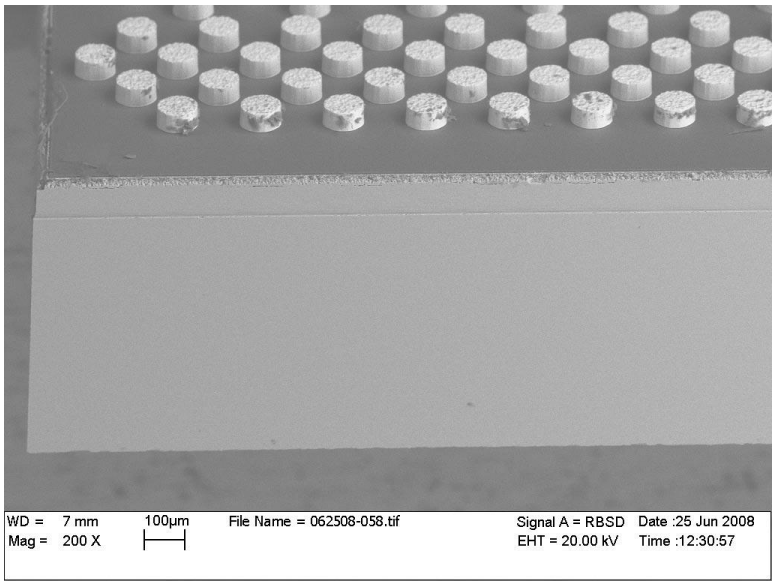

(A)

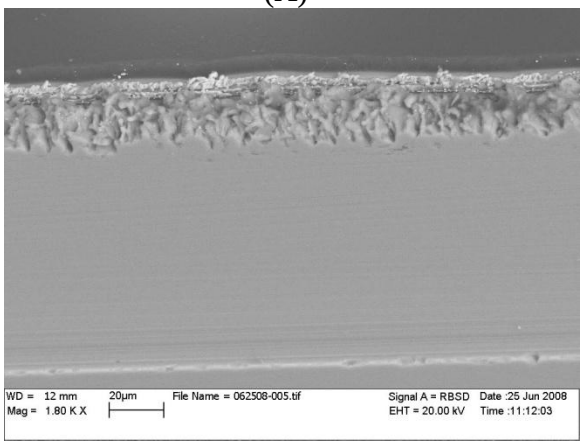

(B)

Figure 4-5: (A) SEM micrograph of selected area of the surface created by the dicing process. Surface roughness near the top of the edge can be seen. (B)Magnified image of a region from the top of the edge is shown.

4.3 X-ray diffraction topography in transmission geometry

Many problems in semiconductor manufacturing can be traces to stress in the device. Edges of the devices are in general more susceptible to stress. It has been reported by many researchers [1, 18] that the dislocations nucleate on defects such as surface damage, oxide precipitates or preexisting dislocations. Dislocations structure in Silicon is well known and can be described with the use of Thompson's tetrahedron [81]. Generation, motion and interaction of dislocations in Silicon during thermal treatment have been studied by many investigators [82-86] by X-ray diffraction topography.

In order to investigate defect structure near the edge of the die, X-ray diffraction topographs of die near the edge is taken in transmission geometry. Topographs were taken such that the beam covers only a small area near the edge as shown in Figure 4-4. Specimen is mounted on the goniometer and the beam size is adjusted, such that entire edge of the sample is covered by the beam.

Crystal orientation and diffraction geometry: First the Silicon die is oriented such that the (0 0 1) plane is oriented perpendicular to the incident beam and right side plane is (1 1 0) as shown in Figure 4-5. In order to record -2 2 0 topograph sample is rotated by 12^0 about y-axis and is also be verified by using LauePt software[48].

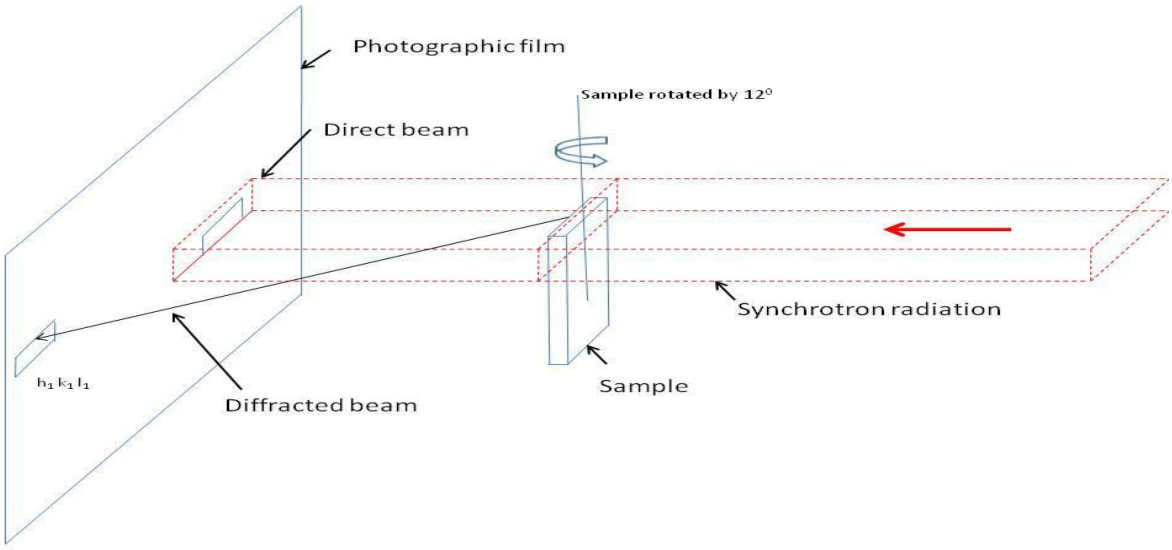

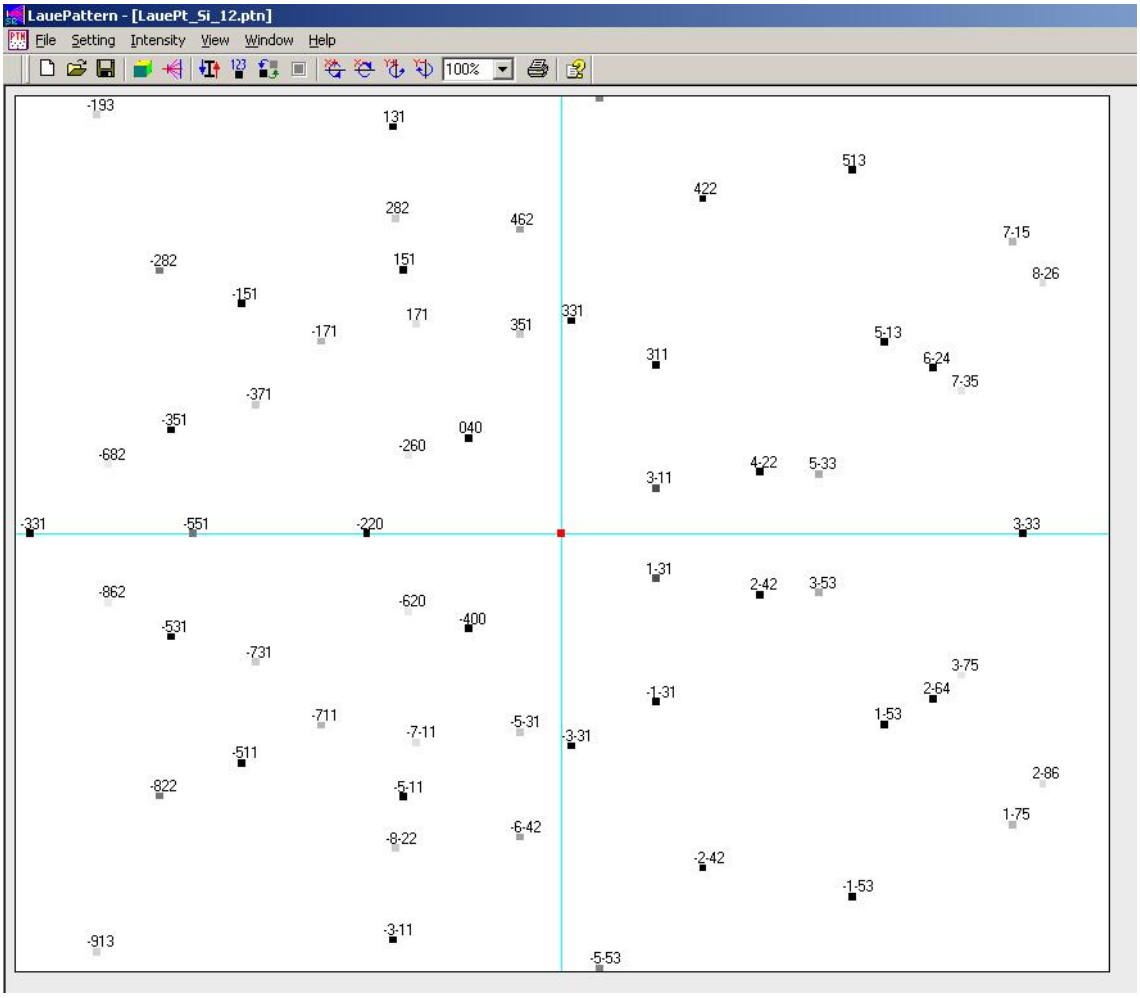

Figure 4-6: (A) Crystal orientation and diffraction geometry (B) Laue pattern generated using simulation software LauePt [48]. -2 2 0 topograph is recorded (λ=.80 A)

-2 2 0 topograph is recorded on the Agfa X-ray film. All four edges of the die are imaged. Topograph of the entire edge of the die crystal is given in Figure 4-6. In order to observe finer features in the topographs, high magnification images of selected regions is also given in Figure 4-7.

Figure 4-7: -2 2 0 transmission topograph recorded from edge of the die.

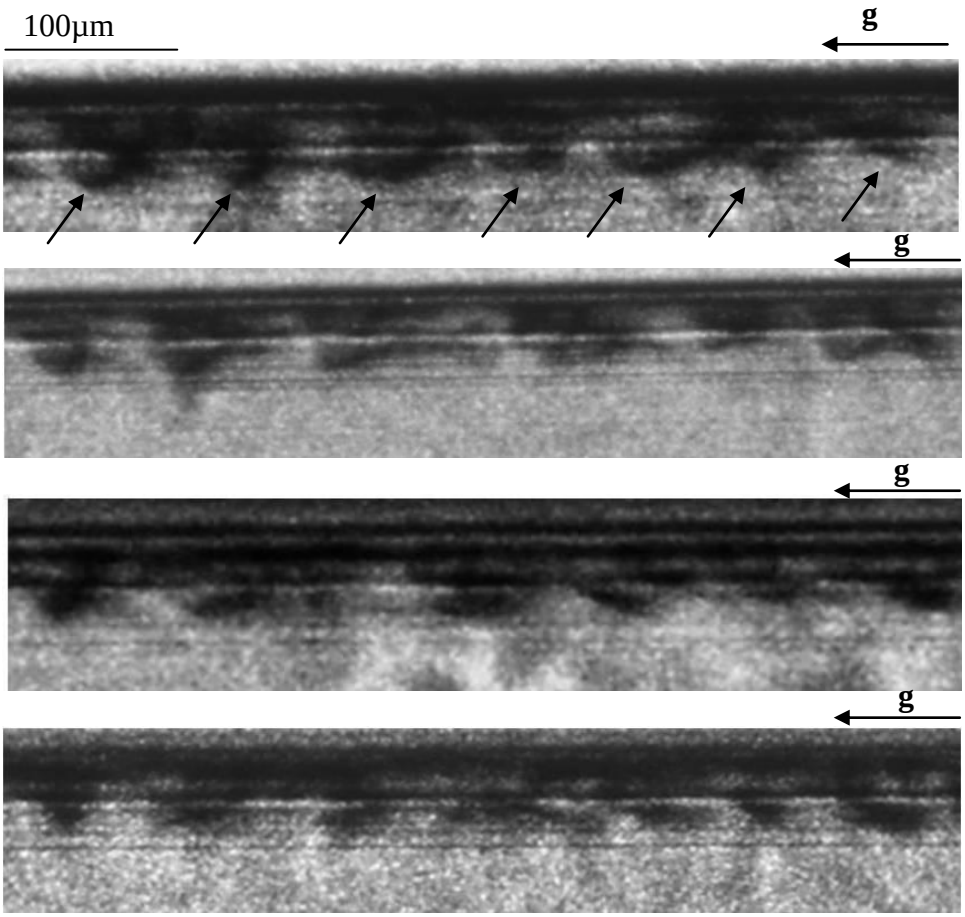

Figure 4-8: High magnification images of selected region in the -2 2 0 topograph. Half looped shaped features are observed over the entire length of crystal edge.

4.4 Results and discussion

In the topographs, contrast in the shape of half loop can be seen. These half loop structure, maked by arrow in the Figure 4-7 are uniformly distributed along the length of the crystal. These contrasts appear to be arising from the dislocations present near the edge. A further validation of our assumption is in the next section where we carried out high temperature in-situ topography. These dislocations may have originated during the dicing process. Dislocations can lie on {1 1 1} slip plane in a Silicon crystal, which essentially comprised of four independent slip planes: (1 1 1), (-1 1 1), (1 -1 1) and (1 1 -1) having slip direction <1 -1 0>. These four possible slip planes are shown schematically in Figure 4-8.

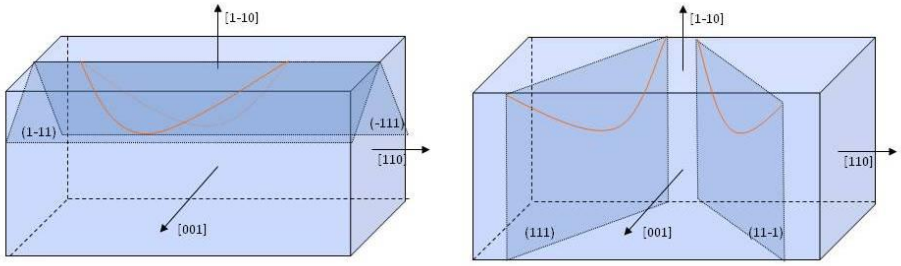

(A) (B)

Figure 4-9: Four possible dislocation half loop configuration in Silicon. In configuration (A) dislocation can move (slip) sideways and can have any possible length and in configuration (B) dislocations end are restricted at the side of crystal and therefore have restricted length.

In the configuration (A) which includes the slip planes (-1 1 1) and (1 -1 1), dislocation can expand sideways by slip process and can have any arbitrary length. Whereas in the case of slip planes (1 1 1) and (1 1 -1), as shown in configuration (B) the length of dislocation is confined to the thickness of the crystal. Since we observed the contrast of dislocation in the topograph as constant size, we suspect the dislocations are of the configuration (B), since the dislocations in configuration (A) have possibility of variable lengths. A substantial evidence of this hypothesis is provided by the high temperature topography results and is described in the following section.

Since the Burger's vector is invariant for a dislocation, i.e. the magnitude and the direction of the Burger's vector is constant throughout the length of the dislocation line, the character (% screw and % edge) of the dislocation changes along the length of the dislocation. Therefore the dislocation is mostly a mixed type of dislocation because the dislocation line is a curved line. We apply $\bar{g}\cdot\bar{b}$ analysis to this dislocation in order to determine Burger's vector.

Stereographic projection of cubic crystal is given in Figure 4-10 with (0 0 1) as front plane and (1 1 0) as the side plane. Several planes lie on the equator of the stereographic projection. Topographs of some of these planes are recorded by rotating the crystal to various angle and recording the topograph on the horizontal plane. Some of the recorded topographs are: 2 2 0, -3 -3 3, -2 -2 4, 2 2 4, 3 3 3

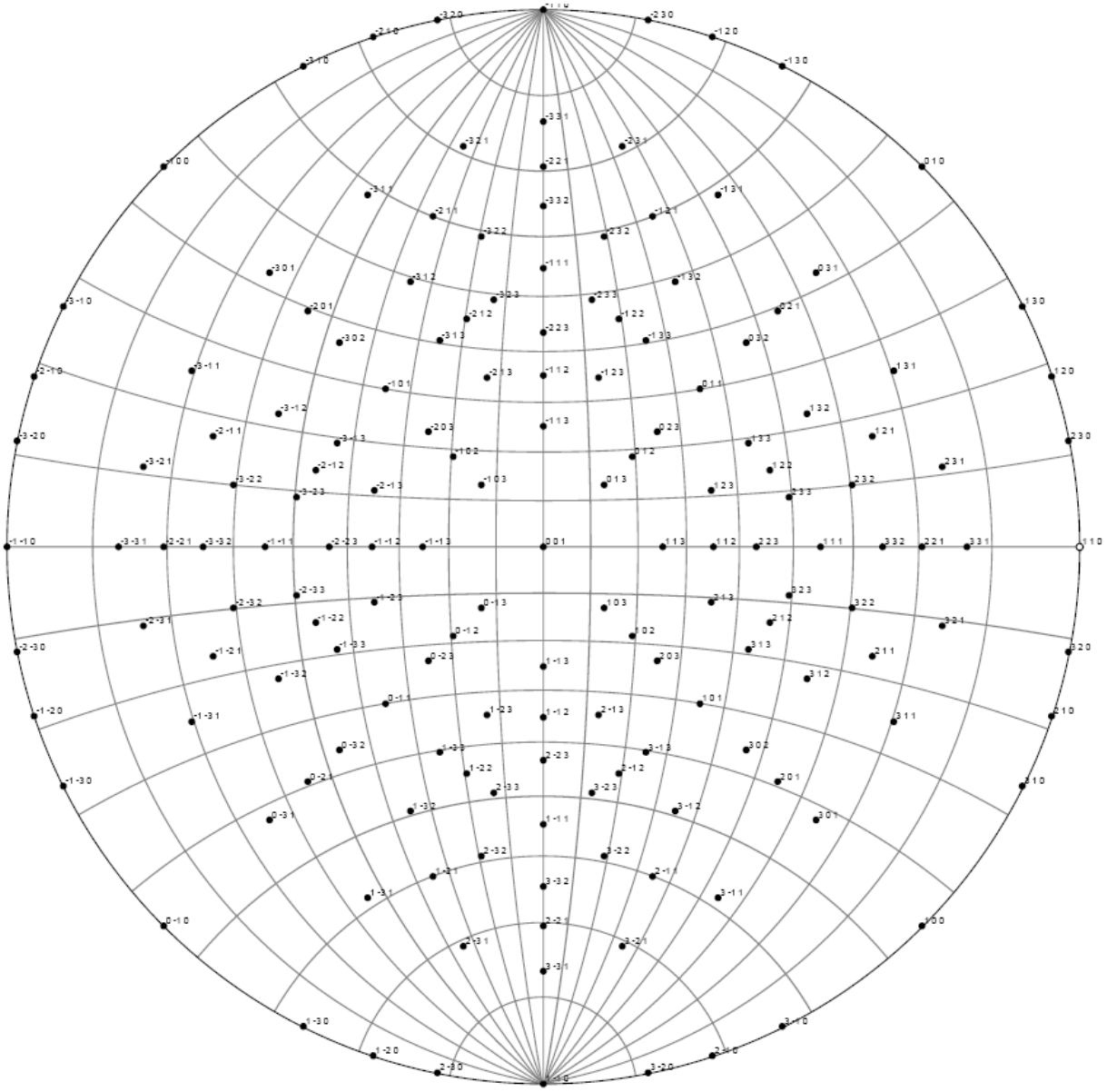

Figure 4-10: Stereographic projection of cubic crystal such that (001) is front plane and (110) is right side plane.

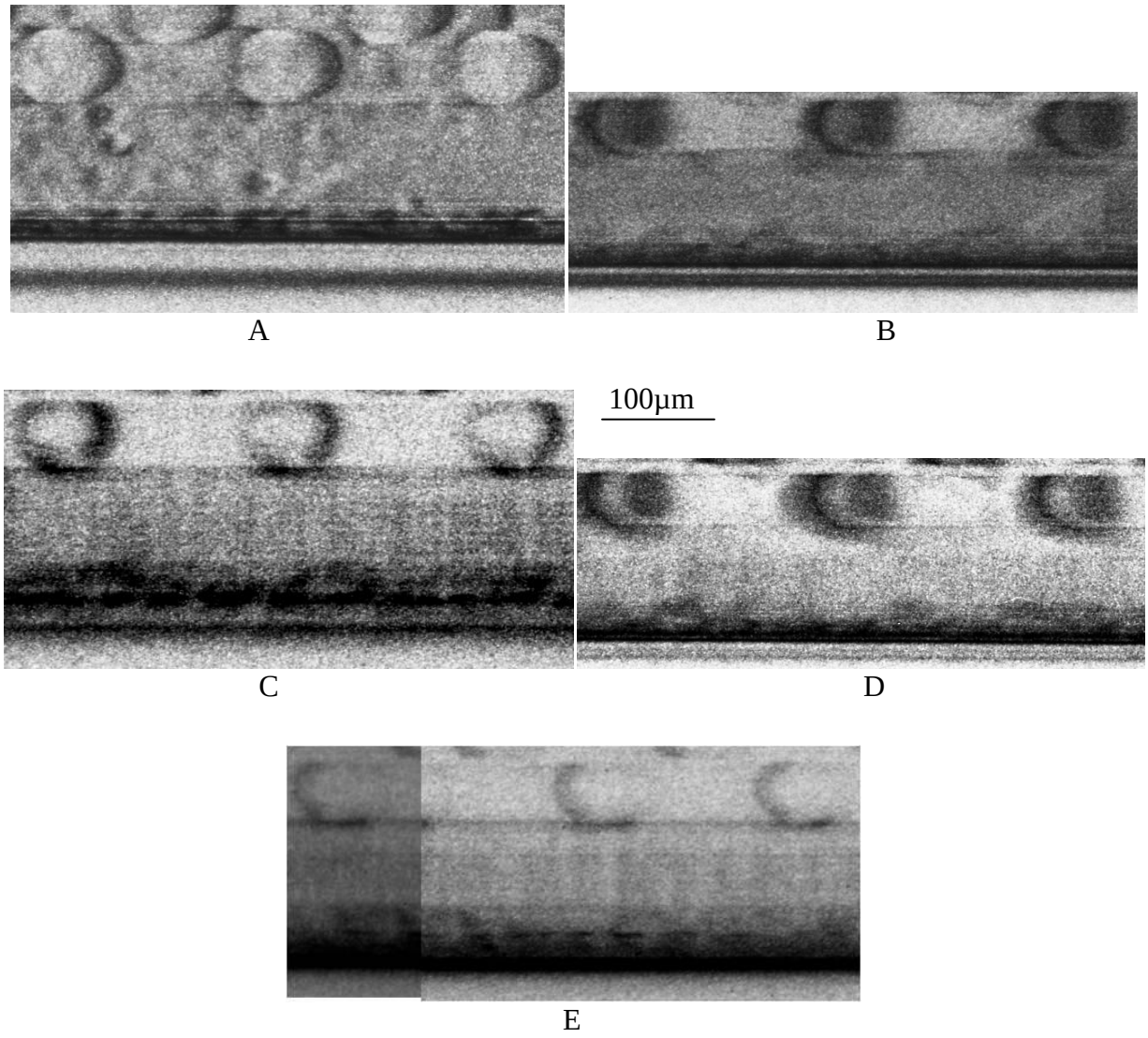

Figure 4-11: Magnified image of selected region of topograph recorded with different g vector. Images are from the same region of the sample. A -2 2 0 B -3 3 -3 C 2 -2 -4 D 3 -3 -3 E 2 2 4

Out of four available slip system we have identified two possible slip systems by observing the uniform length of all dislocation. (1 1 1) and (1 1 -1) are two slip systems where dislocation length is restricted to a constant projected length. Table 4-1 given below summarizes two slip systems and corresponding slip direction (Burger's vector). In Figure 4-11, contrasts due to dislocations are very week which indicate the slip plane (1 1 1) and (1 1 -1).

Table 4-1: List of possible slip systems

Slip plane	Slip direction
1 1 1	1 -1 0
1 1 1	1 0 -1
1 1 1	0 1 -1
1 1 -1	1 -1 0
1 1 -1	1 0 1
1 1 -1	0 1 1

4.5 TEM studies

It is a well known fact that grinding and polishing of Silicon dies edges, introduces sub-surface damage such as cracks [67-69]. TEM studies were carried out to verify that the nature of defect features observed on X-ray topographs i.e. dislocations and cracks. In order to study sub-surface defects such as dislocations and nano-cracks created by cutting and grinding operation of the die, TEM studies were carried out. Samples were chosen from the edge of the die and were thinned down to make it electron transparent. One of key step for success in TEM analysis is the sample preparation i.e. cutting, polishing, and ion milling. Steps involved in sample preparation are outlined below. Schematic of steps used for sample preparation are shown in Figure 4-12.

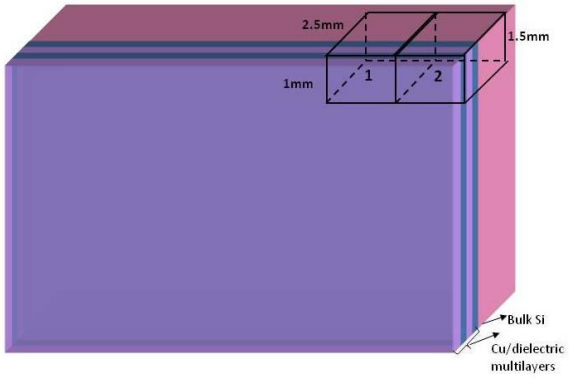

(A)

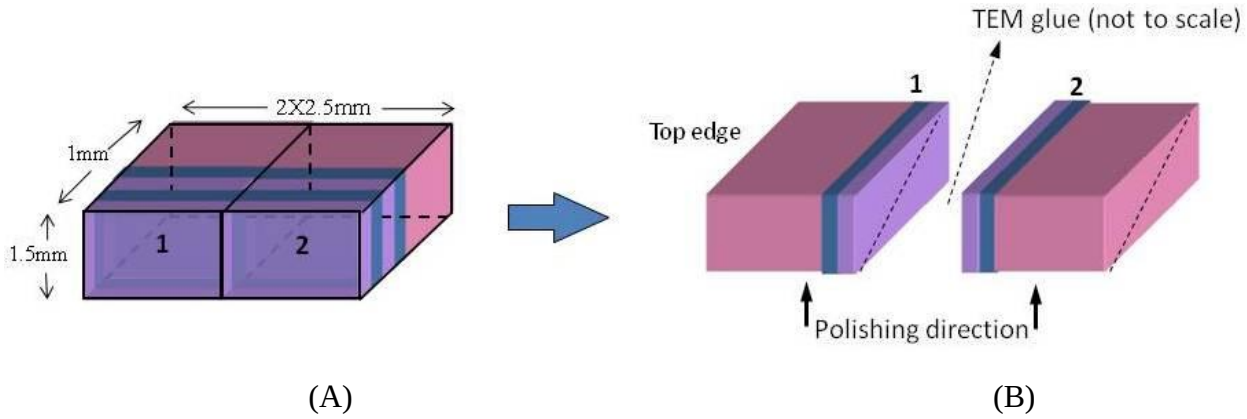

(A) (B)

Figure 4-12: Schematic of sectioning steps for TEM sample preparation. (A) Two small pieces are cut from edge of the sample (B) both pieces with front faces glued together.

As shown in the Figure 4-12 (A), two small pieces are is first cut using low speed diamond saw (cutting wheel). Both the pieces were treated with Nitric Acid (HNO_3) to clean the metallization layer on top and prepare it for gluing together. Both the pieces were glued together using TEM glue (M-Bond 610 epoxy resin). Pieces were glued together in order to protect the edge of the sample during thinning process. Standard procedure for TEM wedge method of sample preparation was followed. Sample is mounted using wax on the polishing fixture (T-Tool). Sample is polished using "Diamond Lapping Film". Lapping film of size 30µm, 15µm, 6µm, 3µm, 1µm and .5µm respectively to achieve sample thickness of approximately 5µm. Sample is first lapped to a thickness about 20µm using coarse lapping film (30µm and 15µm) followed by successive polishing with finer lapping film (6µm, 3µm, 1µm and .5µm), until surface is scratch free under optical microscope to achieve final sample thickness of about 5 µm. Sample is then mounted on a Copper grid followed by ion milling (Fischione Instruments, Model 1010). Sample was then analyzed using TEM (JEOL model number 2100F). Polishing was carried out at our lab, ion milling and TEM imaging were carried out at Brookhaven National Laboratory.

TEM micrographs were recorded; various dislocation configurations and nano-size cracks were observed. Some images of micrographs are shown in Figure 4-13 and 4-14.

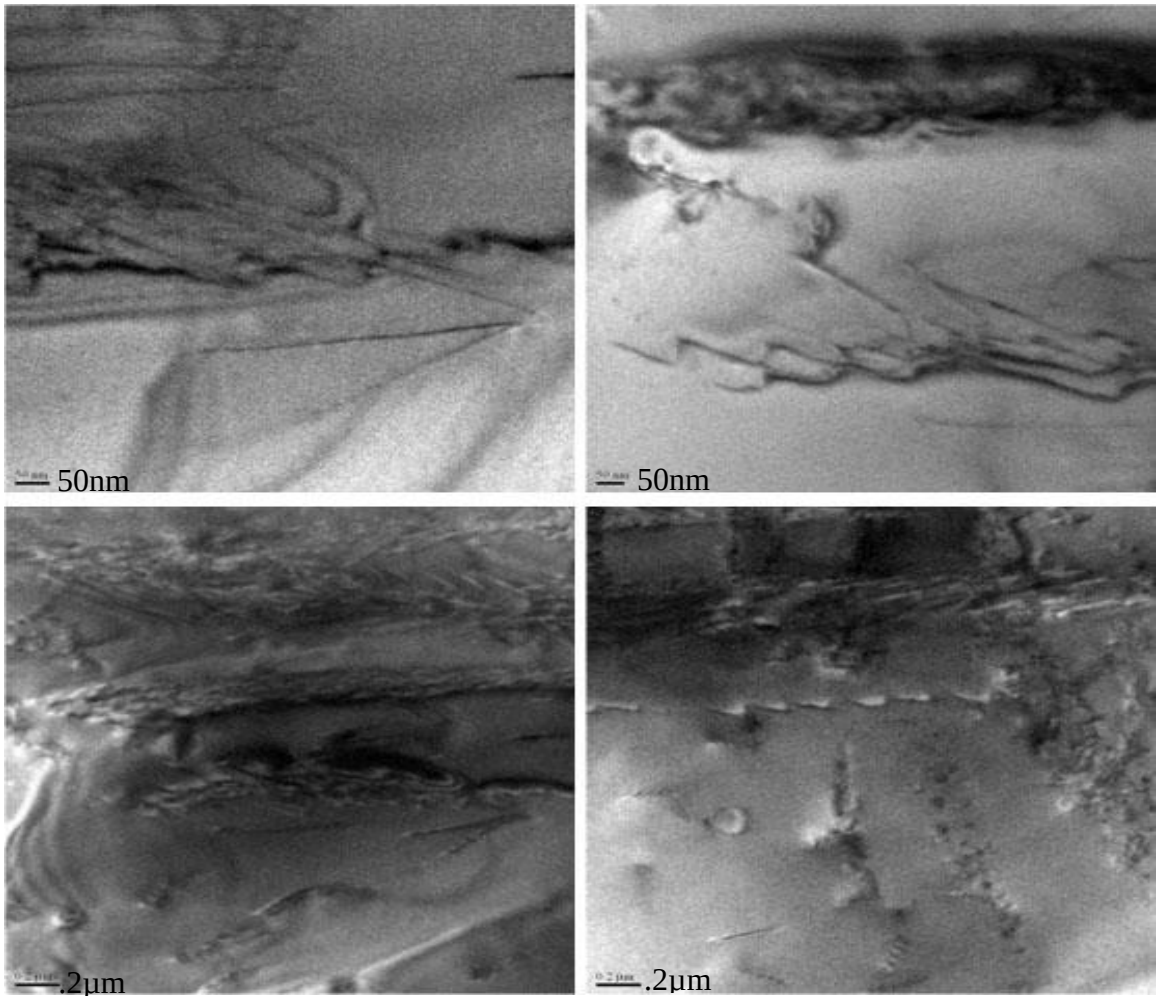

Figure 4-13: TEM micrographs, various dislocation configurations can be seen.

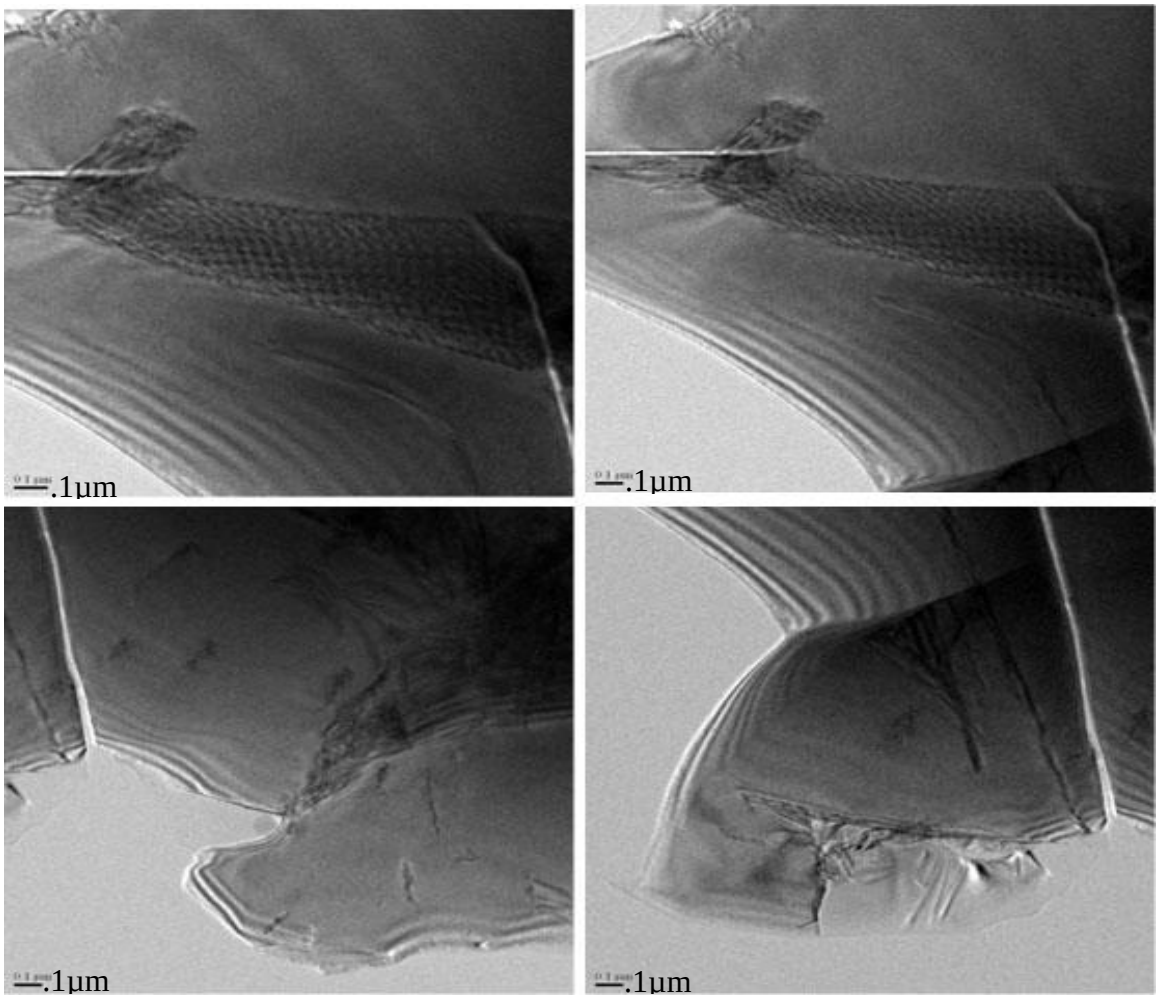

Figure 4-14: Cracks are seen on the micrographs, plastic deformation resulting in dislocation network formation at the end of crack can be seen.

4.6 In situ high temperature diffraction topography

Defects created at the edges during the fabrication process could propagate or change its character during life cycle of the device. Dislocations or other defects if extends into the device, can effectively destroy the device. During the life cycle of the device, it goes through electrical on-off cycle which essentially leads to thermal cycling of material. In order to mimic the actual device condition, we have designed a furnace for thermal cycling of IC and simultaneously take the topographs.

High intensity X-ray source available from synchrotron radiation have made possible in-situ studies of solid state processes. Very short exposure time required for synchrotron radiation

has enabled dynamic and real time observation of experiments. For example, dislocation movement can be observed by taking a series of topographs while applying external stimuli to the crystal such as heat. Various real time in-situ X-ray diffraction topography experiments have been carried out, such as observation of phase transformation [87], plastic deformation [88] and residual stress due to applied electrical bias voltage [89]. In-situ studies have been carried out using laboratory X-ray sources, but these are far from real time as the time required for imaging is very long. Synchrotron X-ray diffraction topography is an excellent technique, useful for understanding real time defect structure and propagation in single crystal material by setting up in-situ experiments.

Furnace design and description:

In order to understand defect behavior at higher temperature and during thermal cycling we have designed and manufactured an environmental chamber (furnace) capable of in-situ X-ray diffraction topography. Even though there is substantial amount literature on high temperature diffractometer and powder diffraction there is very few literature reported on high temperature X-ray diffraction topographgy such as Kune [90] and recently by Danilewisky et al. [19]. High temperature diffraction study has been pursued for many years. A comprehensive survey of the literature and the devices has been compiled by Goldschmidt [91]. We designed and assembled a compact furnace in order to study real time defect behavior using X-ray diffraction topography.

The important features of our furnace are:

1. Lightweight and small size: Furnace is designed to be light so that it can be easily mounted (and demounted) on top of goniometer inside the hutch of X-19C beamline at BNL-NSLS.
2. Flexibility for sample alignment during operation allows us to adjust the orientation of sample to precise angular position for topographic imaging.
3. Lower thermal gradient: Uniform distribution of heating element and small size helped achieve lower thermal gradient.
4. Simple and compact design which can be adaptable with different beamline or diffractometer.

Furnace is designed such that not only fine angular rotation is possible during high temperature furnace operation but also large rotation about vertical (Y) axis is possible.

Main elements of the furnace are:

1. Frame or the structure of furnace
2. Window for incoming and diffracted beam
3. Heating elements
4. Insulation
5. Temperature controller and thermocouple
6. Fixture for holding sample

A description of each of the furnace elements and the reason to choose one over the other is given.

Frame description: The frame of the furnace is made out of square Aluminum alloy tubing (Ultra-Corrosion-Resistant Architectural Aluminum (Alloy 6063)), McMaster Carr part number: 88875K48. The square tubing has dimension of 4”(H)X4”(W)X6’(L) and has a wall thickness of 1/8” +\- .013”. This tubing is cut to the desired length of the furnace (7 inches). Aluminum alloy is chosen instead of Steel, as we intended to keep the furnace light for direct mounting on goniometer. The schematic drawing of the Aluminum tubing used for furnace is given in Figure 4-15. Two sidewalls are also made out of Aluminum and both of the pieces are attached to the frame using screws for easy mounting and removal of sample.

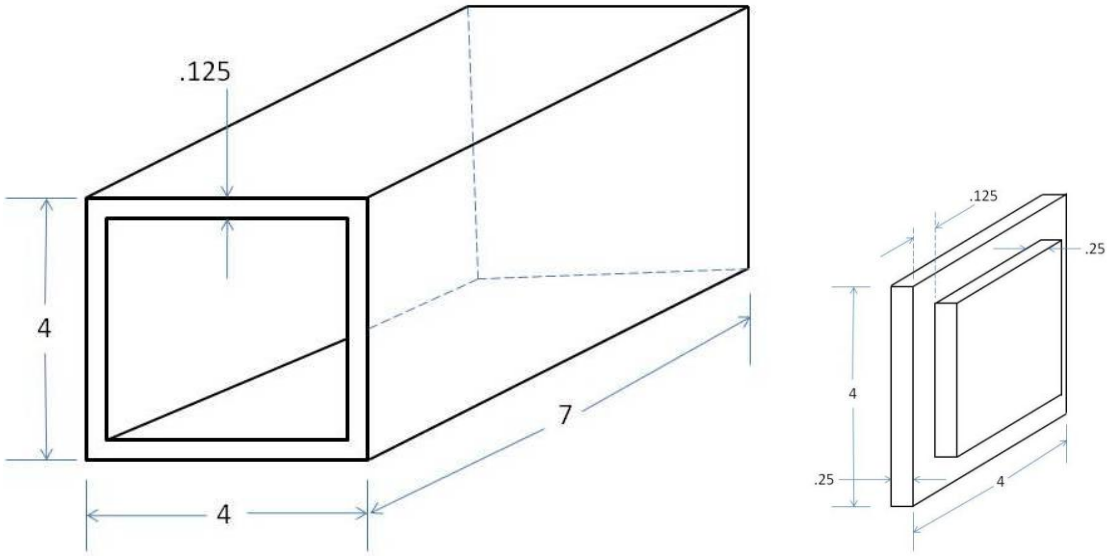

A B

Figure 4-15: (A) Aluminum alloy square tubing is used for furnace construction. Length of furnace is chosen to be 6" and height X width is 4"X4" (B) 2 X Side walls are also made out of Aluminum alloy

Furnace window: One of the design requirements of the furnace is to have at least two X-ray transparent windows, one for incoming beam and another for diffracted beam. We have intentionally kept the window for diffracted beam to be wide enough, such that broad range of diffraction angle can be accepted by the window. In the literature, various materials are used and described as window material, such as Kapton, Mylar, Aluminized Mylar, Beryllium, high purity Aluminum foil, Mica and Silicon Nitride Si3N4 [92], [93]. Beryllium is generally used as vacuum window for hard X-ray in synchrotron radiation beam-line. The important criteria for window material are high X-ray transmittance and mechanical strength.

We have chosen .002" thick Kapton sheet, McMaster Carr part number: 2271K2. This material has an operating temperature range from -425° to +752° F. In order to reduce the heat loss from the window we kept the window size to smallest possible without interfering with the X-rays.

Heating element: Finned strip heater is used as heating element. It is attached at the base of the furnace. Sketch, specification, drawing and description of these strip heaters are given in Appendix D.

Furnace insulation: Insulation is used inside the furnace frame to prevent heat loss to the surrounding. Flexible ceramic insulation is used in all the area of the inside walls of the furnace except the window area. Six different pieces of the flexible ceramic insulation is cut to the size of inside wall dimension of the furnace. In two of those pieces extra cut has been made to clear the window of the furnace.

McMaster Carr part number 4057K9: Extra-High Temp Ceramic Insulation Strip 1/8" Thick, 3" X 25'
McMaster Carr part number 9323K21: Fiberglass Insulation Paper 1/8" Thick, 16" Width, 10' Length

Temperature controller, relay and thermocouple: Temperature controller is used in order to monitor and regulate the process temperature. The controller was acquired from Omega Engineering Inc. (Part number: CN7823 1/16 DIN Controller). The control method use by this controller is PID (proportional–integral–derivative). This controller can be programmed for desired temperature profile or temperature cycling. An image of the controller is shown in Figure 4-16A. During operation, two temperature value are displayed, PV and SV. PV indicates present value or the current temperature of the furnace, whereas SV represents set value or the current set point or the desired temperature at that time. The operation manual of this controller can be found at Omega's web site http://www.omega.com/Manuals/manualpdf/M4437.pdf
A solid state relay is used to control the resistance heating furnace in conjunction with temperature controller. A relay is basically a SPST (single pole single throw) switch which turns on and off the power to the furnace, after receiving the signal (in form of small voltage) from the controller. A relay from Omega Engineering Inc. part number SSRL240DC10 is chosen for controlling input power to the furnace is shown in Figure 4-16B. The operation, installation and users manual can be found at Omega's web site:
http://www.omega.com/manuals/manualpdf/m3813.pdf.

Figure 4-16: (a) PID temperature controller and (b) Solid state relay for controlling the furnace temperature

Thermocouple type K is used for measuring temperature of the furnace and as a feedback loop to the controller. We have chosen thermocouple from Omega Engineering Inc. (Part number: TC-GG-K-24-36). Each term in the part number is explained as follows:

TC : Thermocouple
GG: Glass braid insulated
K : K type thermocouple
24 : 24 AWG (American Wire Gauge) or .0201 inch diameter
36 : Thermocouple length in inches

Fixture for holding sample: A very simple fixture is designed to hold the sample. Fixture height is adjusted such that the region in the crystal to be topographed is in the same height as furnace window.

Electrical wiring diagram of the controller and the furnace is given in the Figure 4-12. One end of the thermocouple wire is connected to the controller and the other end is inserted inside the furnace through a very small hole on top of the furnace. Output of the controller is

connected to the solid state relay control voltage which in turn acts as an on/off switch for the voltage to the furnace

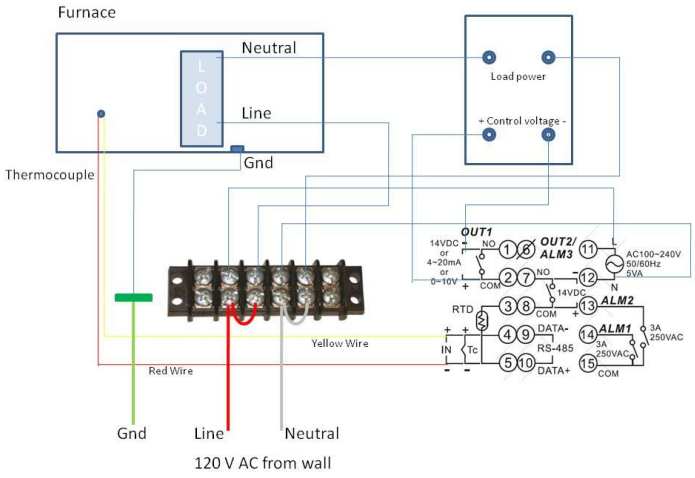

Figure 4-17: Schematic of wiring diagram of the controller and the furnace.

Table 4-2: Features of high temperature X-ray diffraction furnace

Heating method	Shape	Atmosphere	Max. temp. ^{0}C	Heating element	Sample	Use
Radiation /convection	Rectangular box	Air	250^{0}C	Strip resistance heater	Single crystal Si	Diffraction topography

The furnace is placed on top of goniometer, a small ceramic washer is placed between goniometer and the furnace for heat insulation. No trouble occurred during the continuous operation of thermal cycling for 48hrs.

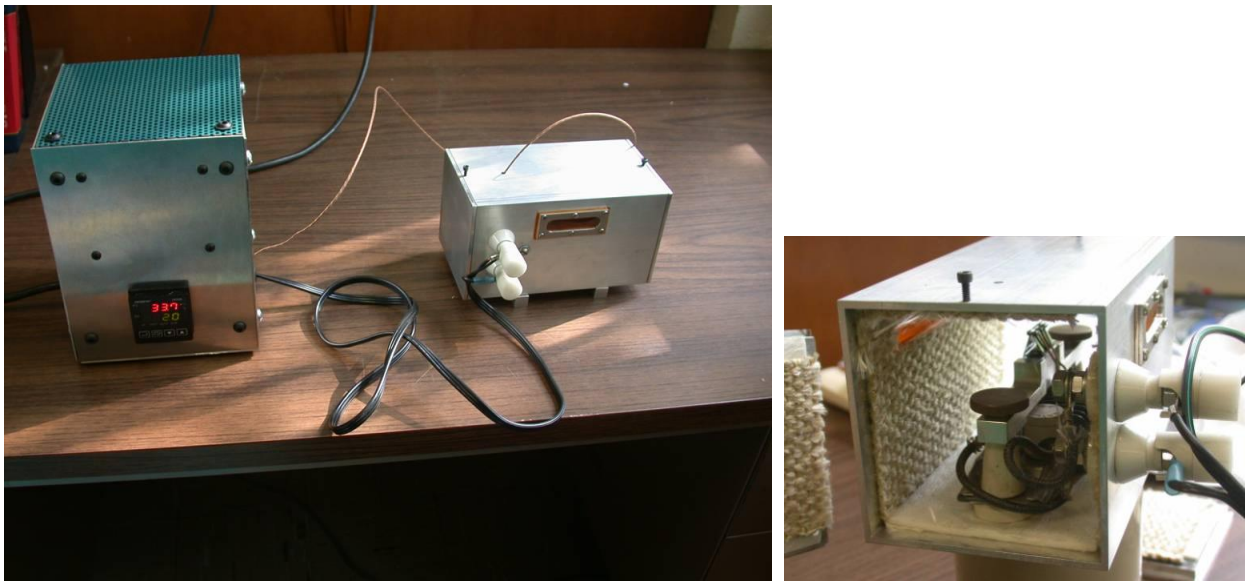

A B

Figure 4-18: (A) Photograph of furnace with controller (B) Inside view of furnace

4.7 Results and discussion

Sample is placed in the furnace and a symmetric Laue pattern is recorded, in this configuration (0 0 1) plane is perpendicular to the incoming X-ray beam and the plane (1 1 0) is the right side plane. Furnace/Sample assembly is then rotated 12^0 about Y-axis and 2 2 0 topographs were recorded at 13cm specimen to film distance. Referring to Figure 4-6(B), the simulated LauePt program [48], it can be seen that 2 2 0 reflection can be recorded at about 57mm to the left of direct beam.

Sample is subjected to thermal cycling in order to simulate the IC during operation. Furnace was thermally cycled and topographs were taken at regular interval. Cycle profile is given below in Figure 4-19. Even though controller was programmed to cycle between 200^0C and 50^0C in 1/2 hr period, furnace could not reach 50^0C in ½ hr, it was able to reach only 100^0C. In order to understand the real time dynamic behavior of defects and specially dislocations, topographs were taken every ½ hr and the experiment was carried out for 40hrs.

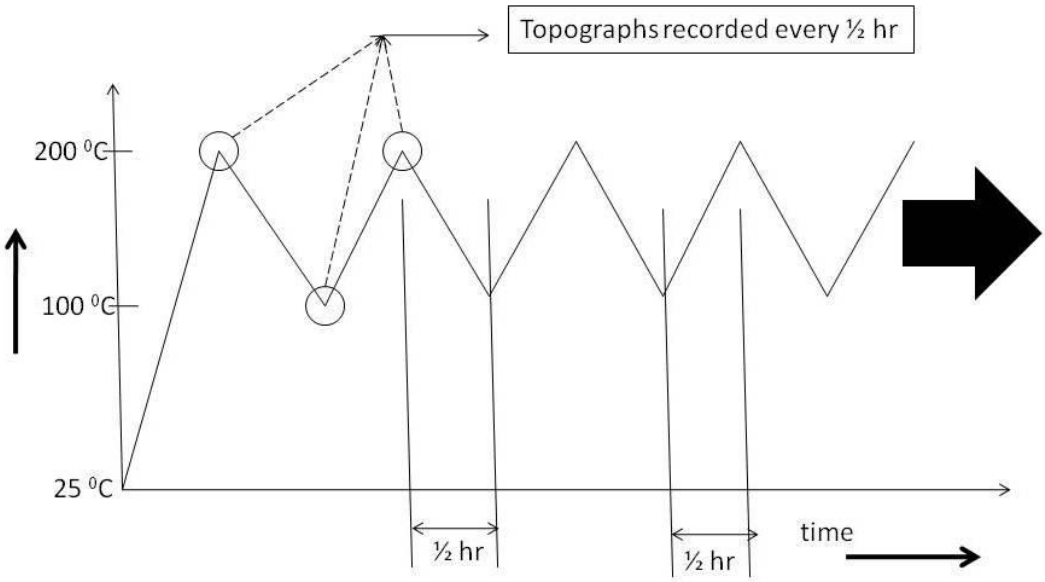

Figure 4-19: Temperature cycle profile. Furnace subjected to thermal cycle and topographs recorded at regular interval, at lower temperature and at elevated temperature.

Selected topographs at various time intervals are shown in Figure 4-20. Comparison of topographs from the same region shows that dislocations have moved toward the crystal edge and in some cases completely disappeared. This result was somewhat expected, because without any external driving force, such as external or residual stress in the crystal (in the region where crystal is located), dislocations should reduce in length. This can be explained with the help of thermodynamics, as reduction in length of dislocation results in reduction of free energy of the system.

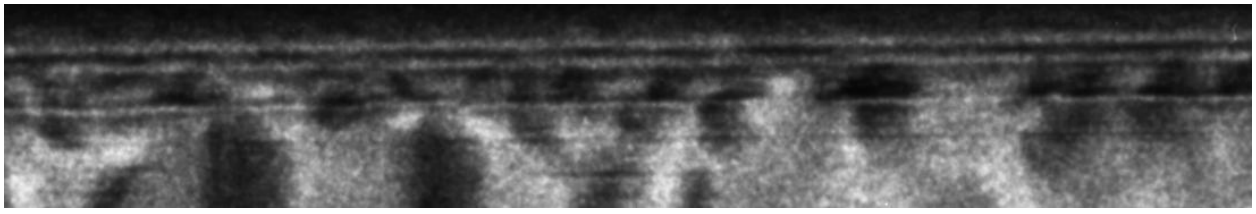

100µm

A

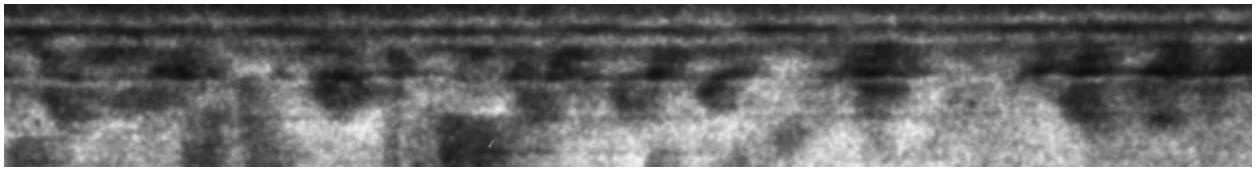

B

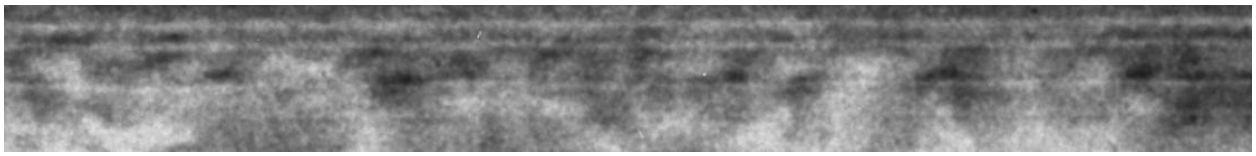

C

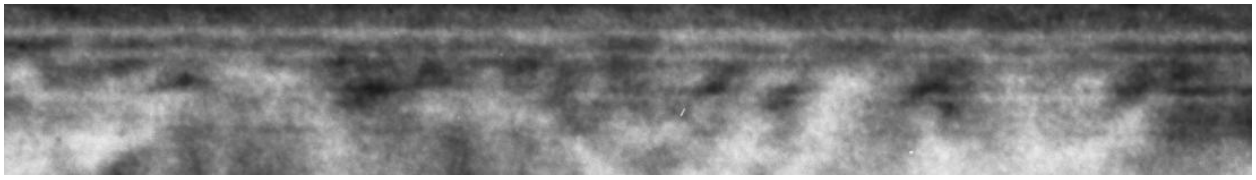

D

Figure 4-20: 2 2 0 Topograph from same selected region of the crystal at various interval of time. A: t=0hrs ; B: t=0.5hrs ; C: t=21.5 hrs ; D: t=39.5 hrs.

Chapter 5 Conclusion and future work

5.1 Conclusion

In this work we have addressed few problems frequently found in Silicon semiconductor industry. Issues primarily studied in this work are related to residual stress calculation and crystallographic defect characterization. A new method is developed to determine all six components of residual strain and stress tensor. This novel technique, stress mapping analysis by ray tracing (SMART), is based on synchrotron X-ray reticulography and the principle of ray tracing. This nondestructive and non-invasive technique has the capability to measure all six components of stress tensor. In this method an area filling polychromatic X-ray beam is directed at the single crystal sample. A grid made out of X-ray absorbing material is placed in front of the sample. Multiple Laue spots were recorded on the X-ray film. The purpose of grid is to locate corresponding point in crystal to the corresponding point in the Laue spots.

Traditionally strain is measured by measuring change in lattice parameter. Instead of measuring change in lattice parameter we have measured change in plane normal vector direction. Plane normal direction(s) at a location in the crystal is determined from the location(s) of corresponding point in the Laue pattern.

A mathematical model is developed which utilizes three independent plane normal vector of an arbitrary location in the crystal and compared to the plane normal of a non-stressed crystal in order to determine strain tensor. Using the stiffness matrix of the crystal stress at that location is determined. A computer code is written in Mathematica which repeats the calculation for a array of points in the crystal and stress maps are generated.

We applied this technique in the transmission geometry to map the strain and thereby the stress state averaged through the thickness of the die. We also further developed this technique to measure and map the stresses along the depth of the die. To achieve this, we have recorded X-ray reticulographs in grazing incidence geometry to limit the interaction of X-ray only to the desired depth of the die. Laue pattern of the crystal is recorded in reflection geometry. Residual stress is calculated in similar method as in transmission geometry using SMART technique. This calculated stress value represents a weighted average (exponentially decaying) stress value. The reason that the stress value is weighted average and not simple average is because the X-ray

intensity drops exponentially as it penetrates the crystal. Multiple data points (stress values) are generated by tilting the crystal at different angle whereby changing the penetration depth. An analytical form of the stress (weighted average) function is generated which is the Laplace transform of real space stress distribution. Real space stress function is determined by evaluating inverse Laplace transform of calculated exponentially weighted average stress function. A code in Mathematica is developed to generate analytical form of experimentally calculated stress function and for calculation of inverse Laplace transform to generate real space stress profile. A complete mathematical validation and analysis is performed. Various sources of error have been identified and quantitative analysis is carried out.

Structural defects are another major concern for semiconductor industry. These defects include dislocations, surface scratches and subsurface cracks, stacking faults, grain boundaries, and precipitates. We have mainly focused in edge surface defects primarily caused by wafer slicing process. X-ray diffraction topography in various geometries is used for detection and characterization of surface and subsurface defects. Other complimentary techniques such as optical microscopy, SEM and TEM are also used. Finally an environmental chamber is designed and manufactured in order to study and analyze defect behavior at high temperature and thermal cycling. High temperature in-situ X-ray topography by temperature cycling is carried and dislocation movements were recorded real time.

5.2 Future work

The part of the goal of this project was to study the feasibility of this new technique, SMART, using synchrotron radiation. We were successfully able to demonstrate on single crystal Silicon device in both transmission and reflection geometry. Transmission geometry provides spatially resolved stress values which is average of the stress in thickness whereas transmission geometry provides both spatially resolved as well as depth resolved stress tensor components.

Technology transfer and implementation into Lab source:

We like to design and develop a system using lab source with substantial automation in which the complete stress analysis can be done. With the use of a very long collimator and a target to produce white radiation (such as Molybdenum) one can achieve this goal. With the use

of a high precision digital X-ray detector, the complete coordinate points in the reticulographs can be determined automatically. Once the coordinate points are digitally recorded, the strain and stress calculation can be carried. In the calculations of strain and stress one need to account for small divergence in the X-ray beam which may enhance the error in the measurements. The system can be built in such a way such that it can be used for both transmission and reflection geometry. The concept of SMART technique for use in lab source is shown schematically in Figure 5-1 below. Both transmission and reflection geometries can be achieved using same equipment.

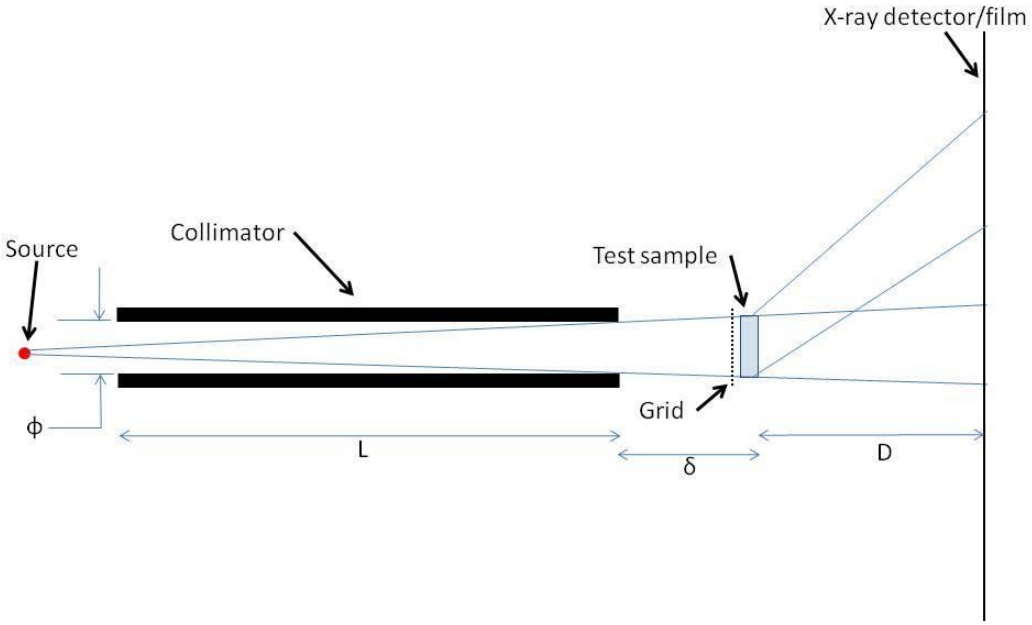

(A)

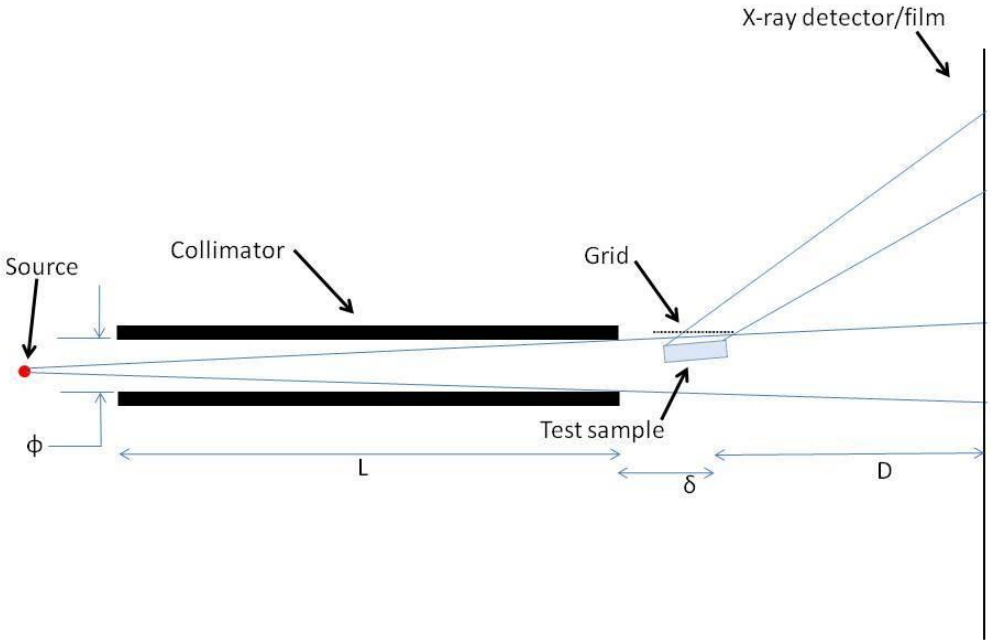

(B)

Figure 5-1: Schematic concept of lab source design for SMART technique: (A) Transmission geometry and (B) Reflection geometry. L is collimator length, ϕ is collimator diameter, D is specimen to film distance and δ is the distance between the end of collimator to sample.

Divergence of the beam is calculated as:

$$\text{Divergence} = 2\tan^{-1}\left(\frac{\phi}{2L}\right) \quad \text{Equation 5-1}$$

A very long collimator can be used in order to reduce the divergence of the beam. Resolution of the system can be calculated using Equation 5-2.

$$R = \frac{SD}{L} \quad \text{Equation 5-2}$$

where S is the source size.

Substituting L=2.5m, D=10cm and S=50μm we get resolution R as 2μm.

Four steps are been identified which are required in order to complete the design and assembly of the stress measurement system using lab source:

- Imaging system: rotating anode, collimator and detector (CCD or film based)
- Data acquisition: automation in detecting coordinate points.
- Data processing: software code to incorporate specific geometry of lab source.
- Stress (or strain) data presentation and graphical representation.

Other techniques used for residual stress determination:

Two other techniques for determining residual stress, micro Raman method and simulation in Abacus has been tried for the purpose of comparison with SMART technique. In case of micro Raman technique, stress is calculated from the shift in Silicon phonon mode with respect to unstrained controlled Silicon standard. 514nm laser light is used for micro Raman experiments and have sampling depth of about 400nm. The formula used for the calculation is:

$$\left(\sigma_{xx}+\sigma_{yy}\right)=-\frac{Shift\left(cm^{-1}\right)}{1.92cm^{-1}}GPa \qquad \text{Equation 5-3}$$

A biaxial stress (σ_{xx}+σ_{yy}) values at selected location is given below in Figure 5-2.

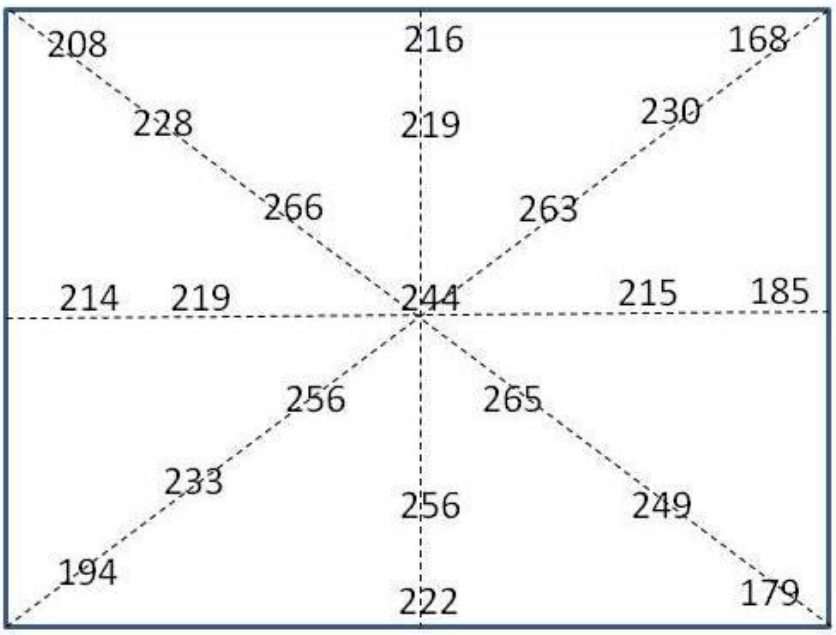

Figure 5-2: Biaxial stress measurement using micro Raman technique at selected location, stress values are in MPa.

A computer simulation is carried out using Abacus. Silicon crystal's bottom surface is attached to the plastic packaging material at high temperature. No slip condition is assumed between attached surfaces. After cooling down to room temperature a bending occurs due to difference in coefficient in thermal expansion as shown schematically in Figure 2-21. Abacus simulation is run to determine stress level at various locations in the crystal.

Both the micro Raman experiments and the Abacus simulations were carried out by Intel Corporations Oregon and Arizona facility respectively. Further studies are required to correlate all the three techniques namely micro Raman, Abacus simulation and SMART.

References

1. Hu, S.M., *Stress-related problems in silicon technology.* J. Appl. Phys., 1991. **70**(6): p. R53-R80.
2. Ma, D.I., et al., *Characterization of the Electrical Bias Induced Strain Variation in Metal-Oxide Semiconductor Field-Effect Transistors Using X-Ray Double Crystal Topography.* Journal of Vacuum Science & Technology a-Vacuum Surfaces and Films, 1992. **10**(4): p. 1012-1019.
3. Ranjan, M., et al., *Die cracking in flip chip assemblies.* Proc. - Electron. Compon. Technol. Conf., 1998. **48th**: p. 729-733.
4. Lu, J., *Handbook of Measurement of Residual Stress*. 1996: Fairmont Press.
5. Fitzpatrick, M.E., A. Lodini, and Editors, *Analysis of Residual Stress by Diffraction using Neutron and Synchrotron Radiation*. 2003. 354 pp.
6. DeWolf, I., *Micro-Raman spectroscopy to study local mechanical stress in silicon integrated circuits.* Semiconductor Science and Technology, 1996. **11**(2): p. 139-154.
7. Roberts, J.C., et al., *Stress measurements in large area array flip chip microprocessor chips.* IEEE Electron. Compon. Technol. Conf., 2008. **58th**(Vol. 3): p. 1462-1471.
8. Voloshin, A.S., P.H. Tsao, and R.A. Pearson, *In situ evaluation of residual stresses in an organic die-attach adhesive.* Journal of Electronic Packaging, 1998. **120**(3): p. 314-318.
9. Chen, T.Y. and C.H. Lin, *Whole-field digital measurement of principal stress directions in photoelasticity.* Optics and Lasers in Engineering, 1998. **30**(6): p. 527-537.
10. Yalamanchili, P., et al., *C-SAM Sounds the Warning for IC Packaging Defects.* IEEE Circuits Devices Mag. , 1994. **10**: p. 36-41.
11. Liu, S. and Y. Mei, *Behavior of delaminated plastic IC packages subject to encapsulation cooling, moisture absorption and wave soldering.* IEEE Transactions on Components, Packaging and Manufacturing Technologies A, 1995. **18**: p. 634-645.
12. Chen, K., et al., *High precision thermal stress study on flip chips by synchrotron polychromatic x-ray microdiffraction.* Journal of Applied Physics, 2010. **107**(6): p. -.
13. Fujii, N., K. Inui, and S. Kozaki, *X-ray stress measurement of mounted silicon chips.* Jpn. J. Appl. Phys., Part 1, 1997. **36**(12A): p. 7411-7414.
14. Kikuta, S., K. Kohra, and Y. Sugita, *Measurements on Local Variations in Spacing and Orientation of Lattice Plane of Silicon Single Crystals by X-Ray Double-Crystal Topography.* Japanese Journal of Applied Physics, 1966. **5**(11): p. 1047-&.
15. McNally, P.J., et al., *Mapping of mechanical, thermomechanical and wire-bond strain fields in packaged Si integrated circuits using synchrotron white beam x-ray topography.* Ieee Transactions on Components and Packaging Technologies, 2001. **24**(1): p. 76-83.
16. Stock, S.R., H. Chen, and H.K. Birnbaum, *The measurement of strain fields by x-ray topographic contour mapping.* Philos. Mag. A, 1986. **53**(1): p. 73-86.
17. Suzuki, H., K. Akita, and H. Misawa, *X-ray stress measurement method for single crystal with unknown stress-free lattice parameter.* Japanese Journal of Applied Physics Part 1-Regular Papers Short Notes & Review Papers, 2003. **42**(5A): p. 2876-2880.
18. Fahey, P.M., et al., *Stress-Induced Dislocations in Silicon Integrated-Circuits.* Ibm Journal of Research and Development, 1992. **36**(2): p. 158-182.
19. Danilewsky, A.N., et al., *Dislocation dynamics and slip band formation in silicon: In-situ study by X-ray diffraction imaging.* J. Cryst. Growth, 2011. **318**(1): p. 1157-1163.
20. Yoshiike, T., N. Fujii, and S. Kozaki, *An X-ray stress measurement method for very small areas on single crystals.* Japanese Journal of Applied Physics Part 1-Regular Papers Short Notes & Review Papers, 1997. **36**(9A): p. 5764-5769.

21. Kanatharana, J., et al. *Mapping of mechanical stresses in silicon substrates due to lead-tin solder bump reflow process via synchrotron x-ray topography and finite element modelling*. 2003: Iop Publishing Ltd.
22. Kanatharana, J., et al., *Evaluation of mechanical stresses in silicon substrates due to lead-tin solder bumps via synchrotron X-ray topography and finite element modeling.* Microelectronic Engineering, 2003. **65**(1-2): p. 209-221.
23. Kanatharana, J., et al., *Examination of mechanical stresses in silicon substrates due to lead-tin solder bumps via micro-Raman spectroscopy and finite element modelling.* Semiconductor Science and Technology, 2002. **17**(12): p. 1255-1260.
24. Imafuku, M., et al., *Advanced x-ray stress analysis method for a single crystal using different diffraction plane families.* Applied Physics Letters, 2008. **92**(23): p. -.
25. Ando, Y. and N. Kato, *X-Ray Diffraction Phenomena in Elastically Distorted Crystals.* Journal of Applied Crystallography, 1970. **3**: p. 74-&.
26. Matsui, J., et al., *Measurement of minute local strain in semiconductor materials and electronic devices by using a highly parallel X-ray microbeam.* Nuclear Instruments & Methods in Physics Research Section B-Beam Interactions with Materials and Atoms, 2003. **199**: p. 15-18.
27. Matsui, J., *Synchrotron Radiation X-ray Studies on Strain in Semiconducting Crystal.* Solid State Phenomena, 1989. **6 & 7**: p. 423-434.
28. Bonse, U. and I. Hartmann, *X-Ray-Measurement of Minute Lattice Strain in Perfect Silicon-Crystals.* Zeitschrift Fur Kristallographie, 1981. **156**(3-4): p. 265-279.
29. Barnett, S.J., B.K. Tanner, and G.T. Brown, *Investigation of the homogeneity and defect structure in semi-insulating LEC gallium arsenide single crystals by synchrotron radiation double crystal x-ray topography.* Mater. Res. Soc. Symp. Proc., 1985. **41**(Adv. Photon Part. Tech. Charact. Defects Solids): p. 83-8.
30. Laue, M.V., Ann Phys., 1936. **26**: p. 55-68.
31. Dudley, M., *X-Ray Topography.* Encyclopedia of Applied Physics, 1997. **2**.
32. Raghothamachar, B., et al., *Defect analysis in crystals using X-ray topography.* Microscopy Research and Technique, 2006. **69**(5): p. 343-358.
33. Black, D. and G. Long, *X-ray topography.* NIST Special publication, 2004. **960-10**.
34. Barrett, C.S., *A New Microscopy and Its Potentialities.* Transactions of the American Institute of Mining and Metallurgical Engineers, 1945. **161**: p. 15-64.
35. Berg, W., *An x-ray method for study of lattice disturbances of crystals.* Naturwissenschaften, 1931. **19**: p. 391-6.
36. Guinier, A. and J. Tennevin, *Two variants of the Laue method and their applications.* Acta Crystallogr., 1949. **2**: p. 133-8.
37. Lang, A.R., *Direct Observation of Individual Dislocations by X-Ray Diffraction.* Journal of Applied Physics, 1958. **29**(3): p. 597-598.
38. Newkirk, J.B., *Observation of Individual Dislocations in Crystals by X-Ray Diffraction Microscopy.* Journal of Applied Physics, 1958. **29**(11): p. 1619-1619.
39. Schulz, L.G., *Method of Using a Fine-Focus X-Ray Tube for Examining the Surface of Single Crystals.* Transactions of the American Institute of Mining and Metallurgical Engineers, 1954. **200**(9): p. 1082-1083.
40. Klapper, H., *Structural defects in crystals and techniques for their detection.* Theoretical and Technological Aspects of Crystal Growth, 1998. **276-2**: p. 291-306.
41. Danilewsky, A.N., et al., *White beam synchrotron topography using a high resolution digital X-ray imaging detector.* Nuclear Instruments & Methods in Physics Research Section B-Beam Interactions with Materials and Atoms, 2008. **266**(9): p. 2035-2040.

42. Tuomi, T., Naukkari.K, and P. Rabe, *Use of Synchrotron Radiation in X-Ray-Diffraction Topography.* Physica Status Solidi a-Applied Research, 1974. **25**(1): p. 93-106.
43. Miltat, J., ed. *Characterization of crystal growth defects by X-ray methods*. Proceedings of NATO ASI, ed. B.K. Tanner and D.K. Bowen. Vol. B63. 1980. 401-420.
44. Hart, M., *Synchrotron Radiation - Application to High-Speed, High-Resolution X-Ray-Diffraction Topography.* Journal of Applied Crystallography, 1975. **8**(Aug1): p. 436-444.
45. Lang, A.R., *International Tables of Crystallography*. Vol. C. 1992.
46. Bowen, D.K. and B.K. Tanner, *High Resolution X-ray Diffractometry and Topography*. 1998.
47. Authier, A., *Dynamical Theory of X-ray Diffraction*. 2003.
48. Huang, X.R., *LauePt, a graphical-user-interface program for simulating and analyzing white-beam X-ray diffraction Laue patterns.* Journal of Applied Crystallography, 2010. **43**: p. 926-928.
49. Dudley, M., J. Wu, and G.D. Yao, *Determination of Penetration Depths and Analysis of Strains in Single-Crystals by White Beam Synchrotron X-Ray Topography in Grazing Bragg-Laue Geometries.* Nuclear Instruments & Methods in Physics Research Section B-Beam Interactions with Materials and Atoms, 1989. **40-1**: p. 388-392.
50. Yuan, D. and M. Dudley, *Dislocation Line Direction Determination in Pyrene Single-Crystals.* Molecular Crystals and Liquid Crystals, 1992. **211**: p. 51-58.
51. Miltat, J. and M. Dudley, *Projective properties of Laue topographs.* J. Appl. Crystallogr., 1980. **13**(6): p. 555-62.
52. Chikawa, J.I., *X-Ray Topographic Observation of Dislocation Contrast in Thin Cds Crystals.* J. Appl. Phys., 1965. **36**(11): p. 3496-&.
53. Hearmon, R.F.S., *The Elastic Constants of Anisotropic Materials .2.* Advances in Physics, 1956. **5**(19): p. 323-&.
54. Huntington, H.B., ed. *Solid State Physics: Advances in Research and Applications*. ed. D.T. F. Seitz. Vol. 7. 1958, Academic Press. 213.
55. Ma, D.I., et al., *Double-Crystal X-Ray Topography Characterization of an Electrical-Bias-Induced Stress Variation in Metal-Oxide Semiconductor Field-Effect Transistors.* Thin Solid Films, 1991. **206**(1-2): p. 18-26.
56. Raghothamachar, B., et al., *A novel X-ray diffraction -based technique for complete stress state mapping of packaged silicon dies.* Mater. Res. Soc. Symp. Proc., 2009. **1158E**(Packaging, Chip-Package Interactions and Solder Materials Challenges): p. No pp given, Paper #: 1158-F01-07.
57. Arridge, R.G.C., A.R. Lang, and A.P.W. Makepeace, *Elastic deformation in a crystal plate where lattice-parameter mismatch is present between adjacent growth sectors. II - Measurement of lattice tilts by synchrotron X-ray reticulography.* Proceedings of the Royal Society of London Series a-Mathematical Physical and Engineering Sciences, 2002. **458**(2027): p. 2623-2643.
58. Lang, A.R. and A.P.W. Makepeace, *Reticulography: a simple and sensitive technique for mapping misorientations in single crystals.* J. Synchrotron Radiat., 1996. **3**(6): p. 313-315.
59. Lang, A.R. and A.P.W. Makepeace, *Synchrotron x-ray reticulography: a versatile new technique for mapping misorientations in single crystals.* Microscopy of Semiconducting Materials 1997, 1997(157): p. 457-460.
60. Lang, A.R. and A.P.W. Makepeace, *Synchrotron x-ray reticulography: principles and applications.* J. Phys. D Appl. Phys., 1999. **32**(10A): p. A97-A103.
61. Norton, J.T., Advances in X-ray analysis, 1968. **11**: p. 401.
62. Noyan, I.C. and J.B. Cohen, *Residual stress : measurement by diffraction and interpretation*. Materials research and engineering. 1987, New York: Springer-Verlag. x, 276 p.
63. Manns, T., A. Rothkirch, and B. Scholtes, *Residual stress determination in surface treated alumina samples applying beam limiting masks.* Powder Diffraction, 2009. **24**(2): p. S77-S81.

64. Genzel, C., *Evaluation of stress gradients sigma(ij)(z) from their discrete laplace transforms sigma(ij)(tau(k)) obtained by X-ray diffraction performed in the scattered vector mode.* Physica Status Solidi a-Applied Research, 1996. **156**(2): p. 353-363.
65. Denks, I.A., et al., *An experimental approach to the problem of transforming stress distributions from the LAPLACE- into real space.* Zeitschrift Fur Kristallographie, 2009: p. 69-74.
66. Tang, Y., et al., *Laser dicing of silicon wafer.* Surface Review and Letters, 2008. **15**(1-2): p. 153-159.
67. Zarudi, I. and L. Zhang, *Subsurface damage in single-crystal silicon due to grinding and polishing.* Journal of Materials Science Letters, 1996. **15**(7): p. 586-587.
68. Zarudi, I. and L.C. Zhang, *Effect of ultraprecision grinding on the microstructural change in silicon monocrystals.* Journal of Materials Processing Technology, 1998. **84**(1-3): p. 149-158.
69. Pei, Z.J., S.R. Billingsley, and S. Miura, *Grinding induced subsurface cracks in silicon wafers.* International Journal of Machine Tools & Manufacture, 1999. **39**(7): p. 1103-1116.
70. Baker, L.R., *Standard for Surface Damage.* Optical Engineering, 1992. **31**(8): p. 1685-1689.
71. Wang, V.S. and R.J. Matyi, *X-ray diffraction observation of surface damage in chemical-mechanical polished gallium arsenide.* J. Electron. Mater., 1992. **21**(1): p. 23-31.
72. Hockey, B.J., *Observations by transmission electron microscopy on the subsurface damage produced in aluminum oxide by mechanical polishing and grinding.* Proc. Brit. Ceram. Soc., 1972. **No. 20**: p. 95-115.
73. Silva, R.M., F.D. Orazio, and J.M. Bennett, *Nondestructive Measurements of Subsurface Structural Defects in Polished Single-Crystal Silicon.* Optics News, 1986. **12**: p. 10-17.
74. Black, D., *Using X-ray topography to inspect surfaces of single-crystal components.* International Journal of Applied Ceramic Technology, 2005. **2**(4): p. 336-343.
75. Bowen, D.K., M. Wormington, and P. Feichtinger, *A novel digital x-ray topography system.* Journal of Physics D-Applied Physics, 2003. **36**(10A): p. A17-A23.
76. Danilewsky, A.N., et al., *White beam topography of 300 mm Si wafers.* Journal of Materials Science-Materials in Electronics, 2008. **19**: p. S269-S272.
77. Kawado, S., et al., *Synchrotron-radiation X-ray topography of surface strain in large-diameter silicon wafers.* J. Synchrotron Radiat., 2002. **9**: p. 166-168.
78. Black, D.R., et al., *Imaging defects in strained-silicon thin films by glancing-incidence x-ray topography.* Applied Physics Letters, 2006. **88**(22): p. -.
79. McNally, P.J., et al., *On the use of total reflection x-ray topography for the observation of misfit dislocation strain at the surface of a Si/Ge-Si heterostructure.* Applied Physics Letters, 2000. **77**(11): p. 1644-1646.
80. McNally, P.J., et al., *Observation of misfit dislocation strain-induced surface features for a Si/Ge-Si heterostructure using total reflection X-ray topography.* Physica Status Solidi a-Applied Research, 2000. **180**(1): p. R1-R3.
81. Thompson, N., *Dislocation Nodes in Face-Centred Cubic Lattices.* Proceedings of the Physical Society of London Section B, 1953. **66**(402): p. 481-492.
82. Gramberg, G. and G. Popp, *Effects of Temperature Quenching on Silicon Slices with and without Dislocations.* Journal of Applied Physics, 1972. **43**(11): p. 4801-&.
83. Miltat, J.E.A. and D.K. Bowen, *Dislocation sources and interactions in silicon.* Phys. Status Solidi A, 1970. **3**(2): p. 431-45.
84. Miltat, J.E.A. and Christia.Jw, *Dislocation Pile-Ups in Silicon.* Philosophical Magazine, 1973. **27**(1): p. 35-47.
85. Schwuttke, G.H. and H.J. Queisser, *X-Ray Observations of Diffusion-Induced Dislocations in Silicon.* Journal of Applied Physics, 1962. **33**(4): p. 1540-&.

86. Matsui, J., *Interaction of Slip Dislocations in Silicon-Crystals Having Low Dislocation Densities.* Physica Status Solidi a-Applied Research, 1975. **27**(2): p. 605-613.
87. Dudley, M. and G.D. Yao, *Synchrotron Topography of Phase-Transitions in Perovskite-Like Crystals.* Journal of Physics D-Applied Physics, 1993. **26**(4A): p. A120-A125.
88. Wu, J. and M. Dudley, *Synchrotron white radiation x-ray topographic investigation of dislocation configurations developed in indium antimonide single crystals by plastic bending.* Mater. Res. Soc. Symp. Proc., 1993. **307**(Applications of Synchrotron Radiation Techniques to Materials Science): p. 231-6.
89. Ma, D.I., et al., *Double-crystal x-ray topography characterization of an electrical-bias-induced stress variation in metal-oxide-semiconductor field effect transistors.* Thin Solid Films, 1991. **206**(1-2): p. 18-26.
90. Kume, S. and N. Kato, *Furnace for High-Temperature X-Ray-Diffraction Topography.* Journal of Applied Crystallography, 1974. **7**(Aug1): p. 427-429.
91. Goldschmidt, H.J., *High-temperature x-ray diffraction techniques.* Intern. Union Cryst., Comm. Cryst. App., Bibliog., 1964. **1**: p. 22 pp.
92. Lurio, L., et al., *Windows for small-angle X-ray scattering cryostats.* Journal of Synchrotron Radiation, 2007. **14**: p. 527-531.
93. Suzuki, Y., A. Momose, and H. Sugiyama, *Characterization of windows and filters for coherent X-ray beamlines.* Journal of Synchrotron Radiation, 1998. **5**: p. 596-599.

Appendix A: Proof of plane normal equation

Consider a crystallographic plane perpendicular to z axis as shown in Figure A-1.

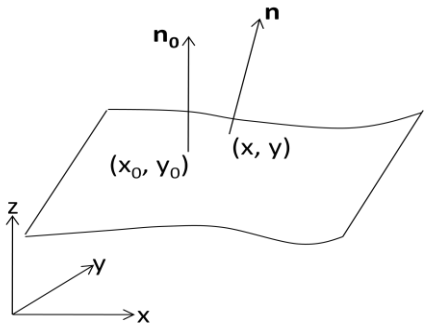

Figure A-1: Schematic of a general warped crystallographic plane, n represents plane normal at an arbitrary location.

Assuming the plane is slightly distorted at a location A and as a result plane normal vector is tilted at an angle with respect to plane normal vector n0 at undistorted region in the crystal. Let us consider the equation of surface as

$z = f(x, y)$ Equation A-1

or, $F(x, y, z) = f(x, y) - z = 0$ Equation A-2

Plane normal vector at any general location can be written as:

$\bar{n}(x, y, z) = \bar{\nabla}[F(x, y, z)]$ Equation A-3

Applying Taylor's expansion to the function f, we get

$$f(x,y) = f(x_0, y_0) + \left(\frac{\partial f(x_0, y_0)}{\partial x}(x - x_0) + \frac{\partial f(x_0, y_0)}{\partial y}(y - y_0)\right)$$ Equation A-4

$r = (x - x_0)\hat{i} + (y - y_0)\hat{j}$ Equation A-5

Now consider the term $\vec{r}.\nabla[f(x_0, y_0) - z]$

$$\vec{r}.\nabla[f(x_0, y_0) - z] = \left[(x - x_0)\hat{i} + (y - y_0)\hat{j}\right].\left[\frac{\partial f(x_0, y_0)}{\partial x}\hat{i} + \frac{\partial f(x_0, y_0)}{\partial y}j - k\right]$$

$$= (x - x_0)\frac{\partial f(x_0, y_0)}{\partial x} + (y - y_0)\frac{\partial f(x_0, y_0)}{\partial y}$$

Substituting the above result into Equation A-4, we have

$f(x,y) = f(x_0, y_0) + \vec{r}.\nabla[f(x_0, y_0) - z]$

or, $f(x,y) - z = f(x_0, y_0) - z + \vec{r}.\nabla[f(x_0, y_0) - z]$

or, $\nabla[f(x,y) - z] = \nabla[f(x_0, y_0) - z] + \nabla\left[\vec{r}.\nabla[f(x_0, y_0) - z]\right]$

or, $\bar{n} = \bar{n}_0 - \bar{\nabla}[\vec{r}.n_0]$

Appendix B: Grid design and description

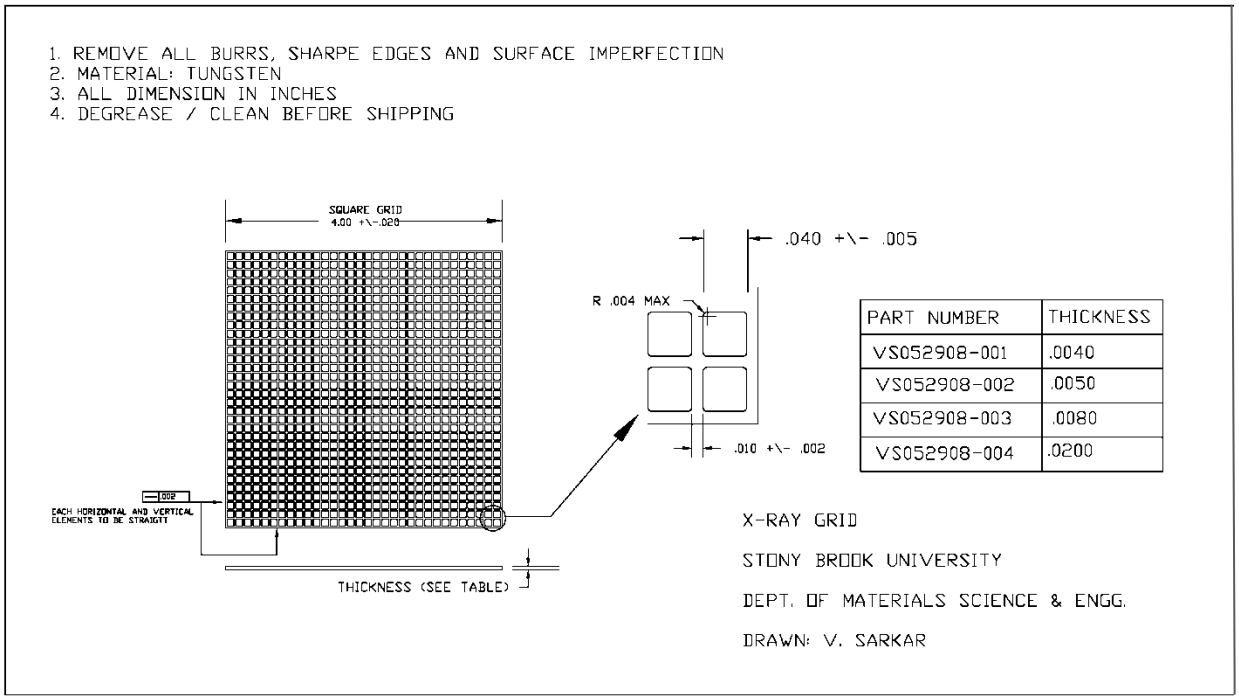

Figure B-1: Engineering drawing of X-ray absorbing grid used for reticulography experiments (SWBXR) in case of both transmission and reflection geometry.

The grid was manufactured by Tecomet Inc. (http://www.tecomet.com) using photochemical etching. Out of two materials: Molybdenum and Tungsten we selected Tungsten because of its superior X-ray absorbing capability in the range of .2A to 1.8A.

Appendix C: Mathematica code for SMART technique

```
resolution=2400;
dsf=80000;
(***** specimen-film distance, in micron, and resolution of scanning *****)

spotrow=48;
spotcolumn=42;
(***** number of row and columns measured *****)

Transmissionx=Table[0,{48},{42}];
Transmissiony=Table[0,{48},{42}];
(***** define two X×Y matrixes which record the transmission spot coordinates *****)

Diffraction1x=Table[0,{48},{42}];
Diffraction1y=Table[0,{48},{42}];
Diffraction2x=Table[0,{48},{42}];
Diffraction2y=Table[0,{48},{42}];
Diffraction3x=Table[0,{48},{42}];
Diffraction3y=Table[0,{48},{42}];
(***** define six X×Y matrixes which record the diffraction spot coordinates *****)

Bridge=Array[b,2016];
Bridge=ReadList["C:\vs_lab\ReRun\B05x.txt"];
k=1;
Do[Transmissionx[[i,j]]=(2.54*10000/resolution)*Bridge[[k]];k=k+1,{i,1,spotrow},{j,1,spotco
lumn}];

Bridge=ReadList["C:\vs_lab\ReRun\B05y.txt"];
k=1;
Do[Transmissiony[[i,j]]=(2.54*10000/resolution)*Bridge[[k]];k=k+1,{i,1,spotrow},{j,1,spotco
lumn}];

Bridge=ReadList["C:\vs_lab\ReRun\B02x.txt"];
k=1;
Do[Diffraction1x[[i,j]]=(2.54*10000/resolution)*Bridge[[k]];k=k+1,{i,1,spotrow},{j,1,spotco
lumn}];

Bridge=ReadList["C:\vs_lab\ReRun\B02y.txt"];
k=1;
Do[Diffraction1y[[i,j]]=(2.54*10000/resolution)*Bridge[[k]];k=k+1,{i,1,spotrow},{j,1,spotco
lumn}];

Bridge=ReadList["C:\vs_lab\ReRun\B04x.txt"];
k=1;
Do[Diffraction2x[[i,j]]=(2.54*10000/resolution)*Bridge[[k]];k=k+1,{i,1,spotrow},{j,1,spotco
lumn}];

Bridge=ReadList["C:\vs_lab\ReRun\B04y.txt"];
k=1;
Do[Diffraction2y[[i,j]]=(2.54*10000/resolution)*Bridge[[k]];k=k+1,{i,1,spotrow},{j,1,spotco
lumn}];

Bridge=ReadList["C:\vs_lab\ReRun\B06x.txt"];
k=1;
Do[Diffraction3x[[i,j]]=(2.54*10000/resolution)*Bridge[[k]];k=k+1,{i,1,spotrow},{j,1,spotco
lumn}];

Bridge=ReadList["C:\vs_lab\ReRun\B06y.txt"];
k=1;
Do[Diffraction3y[[i,j]]=(2.54*10000/resolution)*Bridge[[k]];k=k+1,{i,1,spotrow},{j,1,spotco
lumn}];
(***** save the data into the matrix *****)

FC=Array[fc,3];
FC[[1]]=Transmissionx[[25,13]];
```

```
FC[[2]]=Transmissiony[[25,13]];
FC[[3]]=0;
(***** coordinates of stress free point from the transmission spot *****)

F1=Array[f1,3];
F1[[1]]=Diffraction1x[[25,13]];
F1[[2]]=Diffraction1y[[25,13]];
F1[[3]]=0;
(***** coordinates of stress free point from the diffraction spot 1 *****)

F2=Array[f2,3];
F2[[1]]=Diffraction2x[[25,13]];
F2[[2]]=Diffraction2y[[25,13]];
F2[[3]]=0;
(***** coordinates of stress free point from the diffraction spot 2 *****)

F3=Array[f3,3];
F3[[1]]=Diffraction3x[[25,13]];
F3[[2]]=Diffraction3y[[25,13]];
F3[[3]]=0;
(***** coordinates of stress free point from the diffraction spot 3 *****)

OR=Array[or,3];
OR[[1]]=Transmissionx[[25,13]];
OR[[2]]=Transmissiony[[25,13]];
OR[[3]]=-dsf;
(***** coordinates of stress free point on the crystal *****)

Incidentbeam={0,0,1};
(***** vector of the indicent x-ray beam *****)

Diffractbeam01=F1-OR;
Diffractbeam01=Diffractbeam01/Norm[Diffractbeam01];
(***** vector of the diffract x-ray beam of spot 1 *****)

Diffractbeam02=F2-OR;
Diffractbeam02=Diffractbeam02/Norm[Diffractbeam02];
(***** vector of the diffract x-ray beam of spot 2 *****)

Diffractbeam03=F3-OR;
Diffractbeam03=Diffractbeam03/Norm[Diffractbeam03];
(***** vector of the diffract x-ray beam of spot 3 *****)

N01=Diffractbeam01-Incidentbeam;
N01=N01/Norm[N01];
N02=Diffractbeam02-Incidentbeam;
N02=N02/Norm[N02];
N03=Diffractbeam03-Incidentbeam;
N03=N03/Norm[N03];
(***** plane normal of the stress free point *****)

uxxmatr=Table[0,{48},{42}];
uxymatr=Table[0,{48},{42}];
uxzmatr=Table[0,{48},{42}];
uyxmatr=Table[0,{48},{42}];
uyymatr=Table[0,{48},{42}];
uyzmatr=Table[0,{48},{42}];
uzxmatr=Table[0,{48},{42}];
uzymatr=Table[0,{48},{42}];
uzzmatr=Table[0,{48},{42}];
exxmatr=Table[0,{48},{42}];
exymatr=Table[0,{48},{42}];
exzmatr=Table[0,{48},{42}];
eyxmatr=Table[0,{48},{42}];
eyymatr=Table[0,{48},{42}];
eyzmatr=Table[0,{48},{42}];
ezxmatr=Table[0,{48},{42}];
```

```
ezymatr=Table[0,{48},{42}];
ezzmatr=Table[0,{48},{42}];
(***** defining matrixes of strain components *****)

Do[  S1=Array[s1,3];
       S1[[1]]=Diffraction1x[[i,j]];
       S1[[2]]=Diffraction1y[[i,j]];
       S1[[3]]=0;
       (***** coordinates of stress point from the diffraction spot 1 *****)

       S2=Array[s2,3];
       S2[[1]]=Diffraction2x[[i,j]];
       S2[[2]]=Diffraction2y[[i,j]];
       S2[[3]]=0;
       (***** coordinates of stress point from the diffraction spot 2 *****)

       S3=Array[s3,3];
       S3[[1]]=Diffraction3x[[i,j]];
       S3[[2]]=Diffraction3y[[i,j]];
       S3[[3]]=0;
       (***** coordinates of stress point from the diffraction spot 3 *****)

       SOR=Array[sor,3];
       SOR[[1]]=Transmissionx[[i,j]];
       SOR[[2]]=Transmissiony[[i,j]];
       SOR[[3]]=-dsf;
       (***** coordinates of stress point on the crystal *****)

       Incidentbeam={0,0,1};
       (***** vector of the indicent x-ray beam *****)

       Diffractbeam1=S1-SOR;
       Diffractbeam1=Diffractbeam1/Norm[Diffractbeam1];
       (***** vector of the diffract x-ray beam of spot 1 *****)

       Diffractbeam2=S2-SOR;
       Diffractbeam2=Diffractbeam2/Norm[Diffractbeam2];
       (***** vector of the diffract x-ray beam of spot 2 *****)

       Diffractbeam3=S3-SOR;
       Diffractbeam3=Diffractbeam3/Norm[Diffractbeam3];
       (***** vector of the diffract x-ray beam of spot 3 *****)

       N1=Diffractbeam1-Incidentbeam;
       N1=N1/Norm[N1];
       N2=Diffractbeam2-Incidentbeam;
       N2=N2/Norm[N2];
       N3=Diffractbeam3-Incidentbeam;
       N3=N3/Norm[N3];
      (***** plane normal of the stress point *****)

       Sol=NSolve[{N01[[1]]-N01[[1]]*uxx-N01[[2]]*uyx-N01[[3]]*uzx==N1[[1]],N02[[1]]-
N02[[1]]*uxx-N02[[2]]*uyx-N02[[3]]*uzx==N2[[1]],N03[[1]]-N03[[1]]*uxx-N03[[2]]*uyx-
N03[[3]]*uzx==N3[[1]]},{uxx,uyx,uzx}];
      {uxxmatr[[i,j]]}=uxx/.Sol;
      {uyxmatr[[i,j]]}=uyx/.Sol;
      {uzxmatr[[i,j]]}=uzx/.Sol;


      Sol=NSolve[{N01[[2]]-N01[[1]]*uxy-N01[[2]]*uyy-N01[[3]]*uzy==N1[[2]],N02[[2]]-
N02[[1]]*uxy-N02[[2]]*uyy-N02[[3]]*uzy==N2[[2]],N03[[2]]-N03[[1]]*uxy-N03[[2]]*uyy-
N03[[3]]*uzy==N3[[2]]},{uxy,uyy,uzy}];
      {uxymatr[[i,j]]}=uxy/.Sol;
      {uyymatr[[i,j]]}=uyy/.Sol;
      {uzymatr[[i,j]]}=uzy/.Sol;
```

```
       Sol=NSolve[{N01[[3]]-N01[[1]]*uxz-N01[[2]]*uyz-N01[[3]]*uzz==N1[[3]],N02[[3]]-
N02[[1]]*uxz-N02[[2]]*uyz-N02[[3]]*uzz==N2[[3]],N03[[3]]-N03[[1]]*uxz-N03[[2]]*uyz-
N03[[3]]*uzz==N3[[3]]},{uxz,uyz,uzz}];
      {uxzmatr[[i,j]]}=uxz/.Sol;
      {uyzmatr[[i,j]]}=uyz/.Sol;
      {uzzmatr[[i,j]]}=uzz/.Sol;
       (***** solve the nine equations *****)


       exxmatr[[i,j]]=uxxmatr[[i,j]];exymatr[[i,j]]=1/2 (uxymatr[[i,j]]+uyxmatr[[i,j]]);
       exzmatr[[i,j]]=1/2 (uxzmatr[[i,j]]+uzxmatr[[i,j]]);eyymatr[[i,j]]=uyymatr[[i,j]];
       eyzmatr[[i,j]]=1/2 (uyzmatr[[i,j]]+uzymatr[[i,j]]);ezzmatr[[i,j]]=uzzmatr[[i,j]],
       (***** convert into the strain and save the data into the matrix *****)

  {i,1,spotrow},{j,1,spotcolumn}];
     (***** use the loop to calculate every spot *****)

Do[Extract[exxmatr,{i,j}]>>>exxmatr12.txt,{i,1,spotrow},{j,1,spotcolumn}];
Do[Extract[eyymatr,{i,j}]>>>eyymatr12.txt,{i,1,spotrow},{j,1,spotcolumn}];
Do[Extract[ezzmatr,{i,j}]>>>ezzmatr12.txt,{i,1,spotrow},{j,1,spotcolumn}];
Do[Extract[exymatr,{i,j}]>>>exymatr12.txt,{i,1,spotrow},{j,1,spotcolumn}];
Do[Extract[exzmatr,{i,j}]>>>exzmatr12.txt,{i,1,spotrow},{j,1,spotcolumn}];
Do[Extract[eyzmatr,{i,j}]>>>eyzmatr12.txt,{i,1,spotrow},{j,1,spotcolumn}];

temp=Table[0,{48},{42}];
<<PlotLegends`
exxmatr
ShowLegend[ListDensityPlot[exxmatr, Mesh→False], {ColorData["LakeColors"][1-
#1]&,10,".0023","-.0007",LegendPosition→ {1,-.4}}]
eyymatr
ShowLegend[ListDensityPlot[eyymatr, Mesh→False], {ColorData["LakeColors"][1-
#1]&,10,".0037","-.0052",LegendPosition→ {1,-.4}}]
ezzmatr
ShowLegend[ListDensityPlot[ezzmatr, Mesh→False], {ColorData["LakeColors"][1-
#1]&,10,".0153","-.0154",LegendPosition→ {1,-.4}}]
exymatr
ShowLegend[ListDensityPlot[exymatr, Mesh→False], {ColorData["LakeColors"][1-
#1]&,10,".0139","-.0093",LegendPosition→ {1,-.4}}]
exzmatr
ShowLegend[ListDensityPlot[exzmatr, Mesh→False], {ColorData["LakeColors"][1-
#1]&,10,".0097","-.0065",LegendPosition→ {1,-.4}}]
eyzmatr
ShowLegend[ListDensityPlot[eyzmatr, Mesh→False], {ColorData["LakeColors"][1-
#1]&,10,".0158","-.0063",LegendPosition→ {1,-.4}}]

sigmaxx=Table[0,{48},{42}];
sigmayy=Table[0,{48},{42}];
sigmazz= Table[0,{48},{42}];
sigmayz=Table[0,{48},{42}];
sigmaxz=Table[0,{48},{42}];
sigmaxy=Table[0,{48},{42}];
c11=194.4 ;c22=194.4;c33=165.7; c44=50.9 ;c55=79.6; c66=79.6; c12=35.4; c13=194.4;
c23=63.9;
sigmaxx=c11*exxmatr + c12*eyymatr + c13*ezzmatr;
sigmayy=c12*exxmatr + c22*eyymatr +c23*ezzmatr;
sigmazz=c13*exxmatr + c23*eyymatr + c33*ezzmatr;
sigmayz= c44*2*eyzmatr;
sigmaxz= c55*2*exzmatr;
sigmaxy= c66*2*exymatr;
sigmaxx
ShowLegend[ListDensityPlot[sigmaxx, Mesh→False], {ColorData["LakeColors"][1-
#1]&,10,"3.33","-2.94",LegendPosition→ {1,-.4}}]
sigmayy
ShowLegend[ListDensityPlot[sigmayy, Mesh→False], {ColorData["LakeColors"][1-
#1]&,10,"1.26","-1.34",LegendPosition→ {1,-.4}}]
sigmazz
```

```
ShowLegend[ListDensityPlot[sigmazz, Mesh→False], {ColorData["LakeColors"][1-
#1]&,10,"2.85","-2.52",LegendPosition→ {1,-.4}}]
sigmayz
ShowLegend[ListDensityPlot[sigmayz, Mesh→False], {ColorData["LakeColors"][1-
#1]&,10,"1.61","-.64",LegendPosition→ {1,-.4}}]
sigmaxz
ShowLegend[ListDensityPlot[sigmaxz, Mesh→False], {ColorData["LakeColors"][1-
#1]&,10,"1.55","-1.05",LegendPosition→ {1,-.4}}]
sigmaxy
ShowLegend[ListDensityPlot[sigmaxy, Mesh→False], {ColorData["LakeColors"][1-
#1]&,10,"2.19","-1.47",LegendPosition→ {1,-.4}}]

pstressxx=Table[0,{spotrow},{spotcolumn}];
pstressyy=Table[0,{spotrow},{spotcolumn}];
pstresszz=Table[0,{spotrow},{spotcolumn}];
Do[
 tempmatr={{sigmaxx[[i,j]],
sigmaxy[[i,j]],sigmaxz[[i,j]]},{sigmaxy[[i,j]],sigmayy[[i,j]],sigmayz[[i,j]]},{sigmaxz[[i,j
]], sigmayz[[i,j]],sigmazz[[i,j]]}};
 {pstressxx[[i,j]],pstressyy[[i,j]],pstresszz[[i,j]]}=Eigenvalues[tempmatr],
 {i,1,spotrow},{j,1,spotcolumn}
 ]
pstressxx
ShowLegend[ListDensityPlot[pstressxx, Mesh→False], {ColorData["LakeColors"][1-#1]&,10,"-
4","6",LegendPosition→ {1,-.4}}]
pstressyy
ShowLegend[ListDensityPlot[pstressyy, Mesh→False], {ColorData["LakeColors"][1-#1]&,10,"-
3","3",LegendPosition→ {1,-.4}}]
pstresszz
ShowLegend[ListDensityPlot[pstresszz, Mesh→False], {ColorData["LakeColors"][1-#1]&,10,"-
1","1",LegendPosition→ {1,-.4}}]

Null
```

Appendix C: Laplace transforms: fundamental concepts

Laplace transform is a type of integral transform. Laplace transform has various useful properties and has many important applications in science and engineering. It is an operator, which operates on a function $f(t)$ with real arguments $t \geq \mathbf{0}$ and transforms it to a function $F(s)$ with complex argument. Laplace integral of the function $f(t)$ defined for $\mathbf{0} \leq t \leq \infty$ is defines as:

$$F(s) = \mathcal{L}(f(t)) = \int_{\mathbf{0}}^{\infty} f(t) e^{-st} dt$$

A table of few important Laplace transform are given below:

Table C-1: Table of frequently used Laplace transmorm

$f(t)$	$F(s)$		$f(t)$	$F(s)$
1	$\frac{1}{s}$		e^{at}	$\frac{1}{s-a}$
t	$\frac{1}{s^2}$		$e^{at}\sin(bt)$	$\frac{b}{(s-a)^2+b^2}$
t^n $n=1,2,3\ldots$	$\frac{n!}{s^{n+1}}$		$e^{at}\cos(bt)$	$\frac{s-a}{(s-a)^2+b^2}$
$\sin(at)$	$\frac{a}{s^2+a^2}$		$t^n e^{at}$ $n=1,2,3\ldots$	$\frac{n!}{(s-a)^{n+1}}$
$t\sin(at)$	$\frac{2as}{(s^2+a^2)^2}$		$e^{ct}f(t)$	$F(s-c)$
$\cos(at)$	$\frac{s}{s^2+a^2}$		$f(ct)$	$\frac{1}{c}F\left(\frac{s}{c}\right)$
$t\cos(at)$	$\frac{s^2-a^2}{(s^2+a^2)^2}$		$\frac{1}{t}f(t)$	$\int_s^{\infty} F(u)\,du$

Appendix D: Electrical, mechanical and thermal specification for finned strip heater

Finned strip heater, used as a heating element for the furnace was manufactured by Watlow Electric Manufacturing Company (http://www.watlow.com).

Watlow code number: SGA1J5JY3 [120Volt, 250Watts]

Description: 375 Finned Strip heater

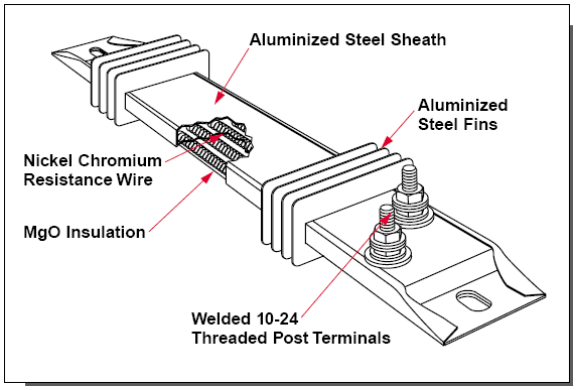

Figure D-1: Cutaway view of finned strip heater.

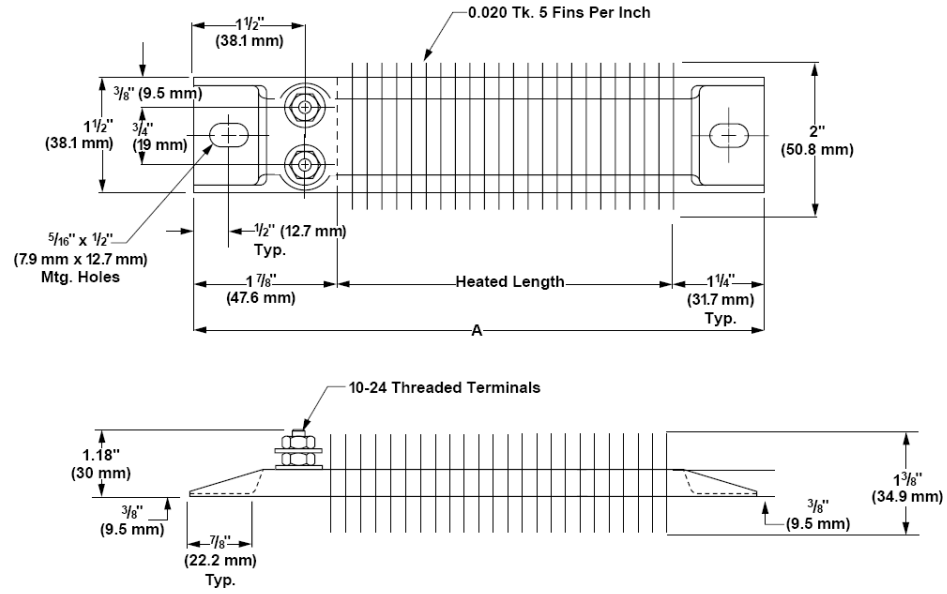

Figure D-2: Engineering drawing of finned strip heater. A=5.5inches is used.

Appendix E: Mathematica code for stiffness tensor C_{ijkl} transformation

When the axis of reference changes by rotation, the individual component of the tensor also changes. As shown in the diagram for the case of stress tensor, the values of each component of stress changes as the axis of reference changes.

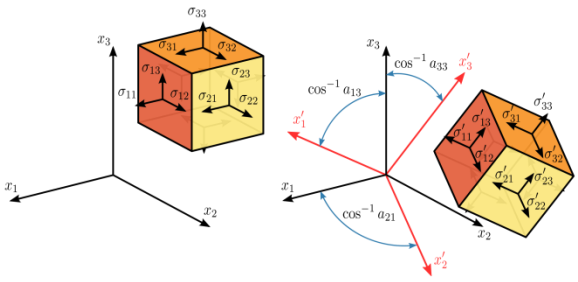

Figure E-1: Schematic illustration of stress components due to transformation of axis

The transformation equation in case of a stress tensor which is tensor of rank two is given by:

$$\sigma'_{ij} = a_{im} a_{jn} \sigma_{mn}$$

where a_{ij} is the cosine of the angle between the new axis x'_i and the old axis x_j. In the above equation summation in m, n, o and p is implied.
In case of tensor of rank four tensor transformation such as stiffness tensor C_{ijkl} is given by:

$$C'_{ijkl} = a_{im} a_{jn} a_{ko} a_{lp} C_{mnop} \qquad \text{Equation [10]}$$

Similar expression can be written in case of tensor of any rank

$$T'_{x_1 x_2 x_3 x_4 \ldots x_n} = a_{x_1 y_1} a_{x_2 y_2} a_{x_3 y_3} a_{x_4 y_4} \ldots a_{x_n y_n} T_{y_1 y_2 y_3 y_4 \ldots y_n}$$

where T is a general tensor of rank n.

A simple Mathematica program is written to convert stiffness constant C_{ijkl} from one coordinate system to another.

```
A={{1/Sqrt[2],1/Sqrt[2],0},{-1/Sqrt[2],1/Sqrt[2],0},{0,0,1}}

stiffness=Table[0,{i,1,3},{j,1,3},{k,1,3},{l,1,3}]

stiffness[[1]][[1]][[1]][[1]]= stiffness[[2]][[2]][[2]][[2]]=
stiffness[[3]][[3]][[3]][[3]]=165.7
```

```
stiffness[[1]][[1]][[2]][[2]]=stiffness[[2]][[2]][[3]][[3]]=stiffness[[3]][[3
]][[1]][[1]]=stiffness[[2]][[2]][[1]][[1]]=stiffness[[3]][[3]][[2]][[2]]=stif
fness[[1]][[1]][[3]][[3]]=63.9

stiffness[[3]][[2]][[3]][[2]]=stiffness[[3]][[2]][[2]][[3]]=stiffness[[2]][[3
]][[3]][[2]]=stiffness[[2]][[3]][[2]][[3]]=stiffness[[3]][[1]][[3]][[1]]=stif
fness[[3]][[1]][[1]][[3]]=stiffness[[1]][[3]][[3]][[1]]=stiffness[[1]][[3]][[
1]][[3]]=stiffness[[2]][[1]][[2]][[1]]=stiffness[[2]][[1]][[1]][[2]]=stiffnes
s[[1]][[2]][[2]][[1]]=stiffness[[1]][[2]][[1]][[2]]=79.6

Table[Sum[A[[m]][[i]] A[[n]][[j]] A[[o]][[k]] A[[p]][[l]]
stiffness[[i]][[j]][[k]][[l]],{i,1,3},{j,1,3},{k,1,3},{l,1,3}],{m,1,3},{n,1,3
},{o,1,3},{p,1,3}]

MatrixForm[%]

tensor=MatrixForm[Table[1000i+100j+10k+l,{i,1,3},{j,1,3},{k,1,3},{l,1,3}]]
```

Appendix F: Plot of mass absorption coefficient of Silicon as a function of wavelength

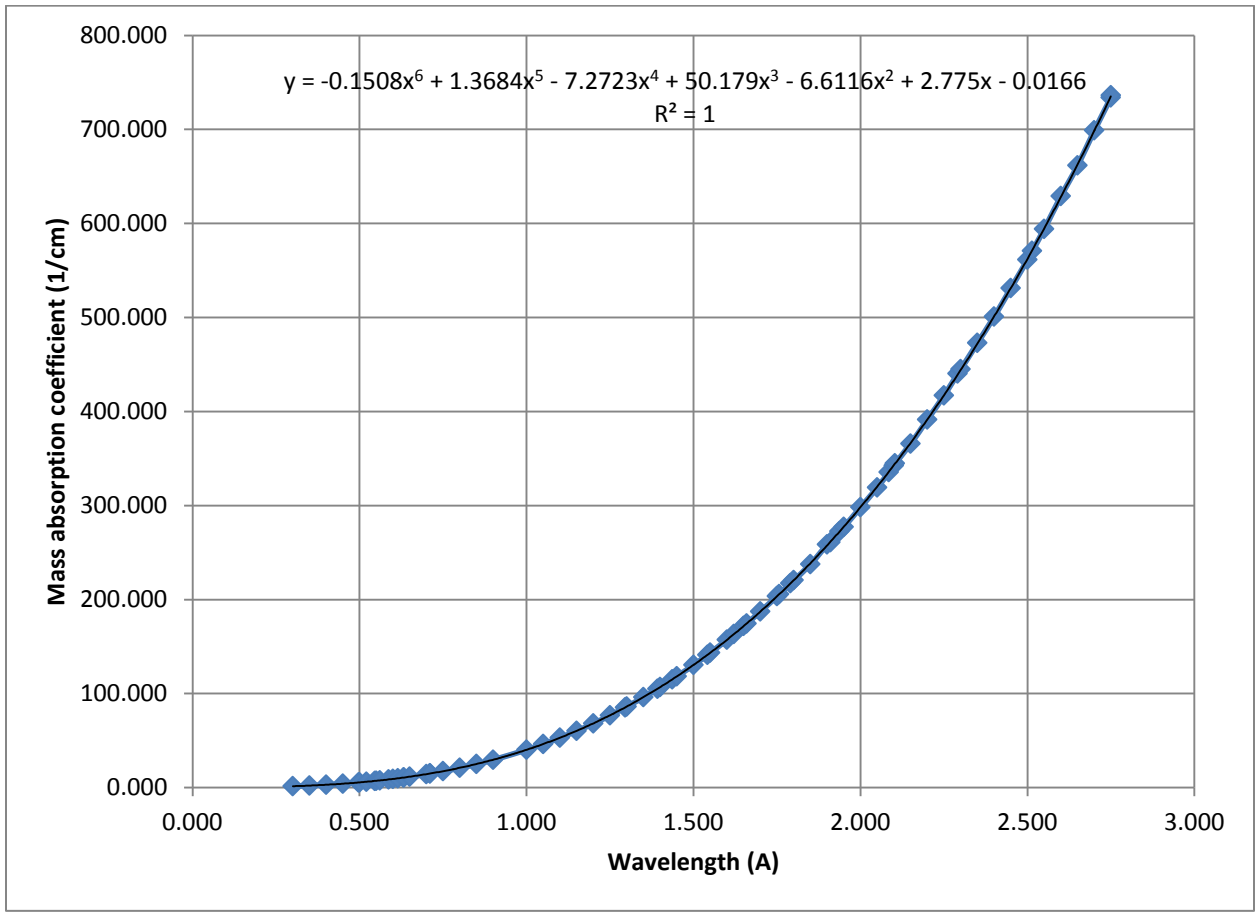

Figure F-1: Plot of mass absorption coefficient of Silicon as a function of wavelength between wavelength .3A to 2.75A. Data of mass absorption coefficient is collected from various sources and a plot is generated. A polynomial function is generated which is used for analytical calculation of mass absorption coefficient at any wavelength.